Downward spreading of turbulence beneath breaking waves and its influence on sediment suspension

Master Thesis

Aline Pieterse
3118770

09-11-2011
2nd version

Department of Physical Geography
Faculty of Geosciences
Utrecht University

Supervisor:
dr. B.G. Ruessink

Contents

1. Introduction

Turbulence is an energetic, rotational and eddying state of motion that results in the dispersion of material and the transfer of momentum, heat and solutes at high rates. Turbulence can, by generating large gradients of velocity at small scales of 1mm to 1cm, cause conditions for fast energy transfer and dissipation. Close to the shoreline, waves will start shoaling and eventually breaking due to the influence of the bed on the wave motion. In this nearshore zone, generation of turbulence under breaking waves occurs at both the surface and bottom boundary layers (Figure 1.1). At the surface turbulence is injected due to breaking waves. The depth of penetration of the turbulence varies with breaker type. Due to bottom shear stress, vorticity, or boundary layer momentum is diffused upward. The bottom boundary layer under waves is generally weak and confined to a region very near the bed (Thornton 1979).

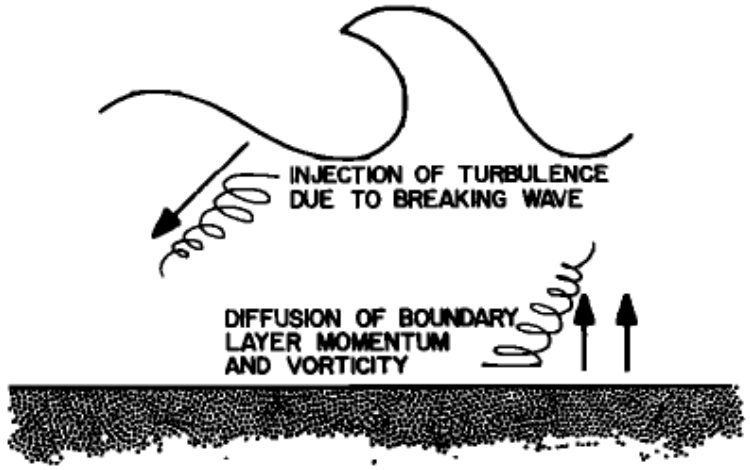

Figure 1.1 Generation of turbulence under breaking waves (Thornton 1979).

During the wave breaking process, the wave energy is converted into two parts: the mean current energy and the turbulent kinetic energy. The turbulent kinetic energy is damped through turbulence viscous dissipation. In this process, the energy of the fluctuating eddies under breaking waves is "drained" due to viscosity and converted into heat (Huang et al. 2009). Turbulent kinetic energy is the mean kinetic energy per unit mass associated with eddies in turbulent flow. Physically, the turbulent kinetic energy is characterized by measured (turbulent) velocity fluctuations.

$k = \frac{1}{2}\langle u'_i u'_i \rangle$, (1)

where i = 1, 2, 3, so that

$$\langle k' \rangle = 0.5(\langle u'^2 \rangle + \langle v'^2 \rangle + \langle w'^2 \rangle), \qquad (2)$$

with ' = turbulence and ⟨ ⟩ = time-average and u, v and w are the cross-shore, longshore and vertical component of the velocity respectively.

Dissipation (ε): the average rate of turbulent energy dissipation.

$$\varepsilon(\omega) = \left[\frac{S_{lm}(\omega)2(2\pi)^{3/2}}{\alpha M_{lm}(\omega)}\right]^{3/2}, \qquad (3)$$

where S_{lm} are the observed spectra, α is the empirical Kolmogorov constant (=1.5) and ω is the radian frequency. The calculation of M_{lm} will be discussed in detail in chapter 4.

Under breaking waves, turbulence can also have an influence on the bed. Turbulence generated at the surface can penetrate through the water column and at the bed, provide an additional mechanism to suspend sediment. Presently, bed sediment transport is parameterised in terms of the wave height or orbital velocity to the power 3. This parameterisation does not seem to be applicable to sediment transport under breaking waves, as this parameterisation is based on the assumption that sediment is suspended by near-bed processes, while surface-generated turbulence is not taken into account. Under breaking waves, sediment suspension is very irregular in time and can vary a lot between waves.

In this thesis, the breaking-wave induced turbulence is the point of focus. First of all, the literature findings about turbulent kinetic energy, turbulent dissipation and sediment suspension related to turbulence will be discussed. From this literature, objectives, hypotheses and research questions were formulated, which will also be discussed. To answer these research questions, a 6-week field experiment was conducted and the data collected there, was analysed. The results of the field experiment are presented in chapter 4-6. First the characteristics of turbulent kinetic energy will be discussed, for example the vertical profile of turbulent kinetic energy and its cross-shore variation. Then the sediment suspension will be discussed, with the dependency of sediment concentration on several parameters and also the relation between sediment suspension and turbulent kinetic energy. The third results chapter will be on the turbulent dissipation, where the vertical profile of dissipation and the variation in the cross-shore will be discussed. Finally there will be a discussion and conclusion.

2. Literature

I. Turbulence

I.1 Structures

The instantaneous turbulent velocity field near the bed is characterized by the passage of large scale turbulent structures, so called horizontal eddies and obliquely descending eddies (Nadaoka et al. 1989; Ting 2006). Horizontal eddies have a rather two-dimensional flow structure with its axis parallel to the crest line, while obliquely descending eddies are strongly three-dimensional in which the eddies stretch obliquely downward (Figure 2.1).

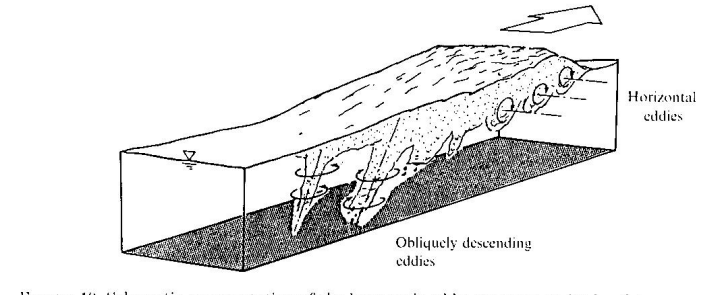

Figure 2.1 Schematic representation of the large-scale eddy structure under breaking waves (Nadaoka et al. 1989).

In the velocity field within the surf zone, the wave motion co-exists with the eddying motion. These eddies are the sources of most of the turbulent kinetic energy and shear stress and also affect the deformation characteristics of the mean flow field. The vorticity that is generated at the front face of the breaking waves is transported

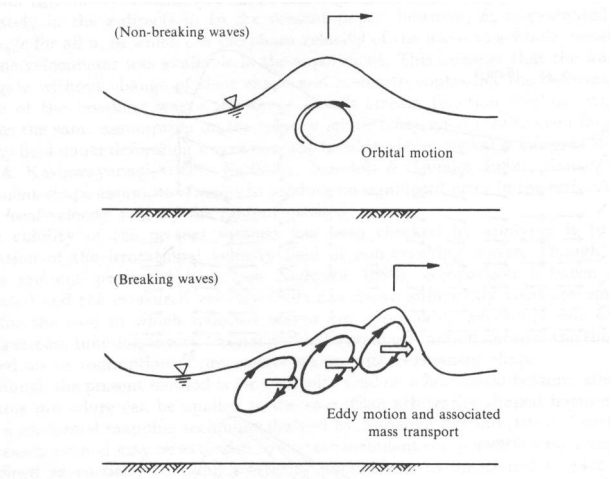

Figure 2.2 Conceptual illustrations of the vorticity effects on mass transport (Nadaoka et al. 1989).

downward by the large-scale eddies into the underlying flow field. The generation of the vorticity-containing mean velocity component causes considerable increase in mass and momentum transport (figure 2.2). These vorticity effects also have an influence on the dynamics of the water surface elevation of breaking waves (Nadaoka et al. 1989).
As said before, the vortices associated with wave breaking can be largely classified into two types: oblique and horizontal vortices. Zhang & Sunamura (1990) showed, based on monochromatic lab waves, that these two kinds of vortices can be clearly distinguished on the Bt (breaker type) = Re (Reynolds number) plane (figure 2.3). The following function was used to find the breaker type:

$$Bt = \frac{H_b}{(gT^2 \tan\beta)} \quad , \qquad (4)$$

in which H_b is breaker height, T is the wave period, tanβ is the bottom slope and g is the gravitational acceleration. The Reynolds number was defined as follows:

$$\mathrm{Re} = \frac{H_b L_b}{\nu T} \quad , \qquad (5)$$

where L_b is the breaker length and ν is the kinematic viscosity of fluid.

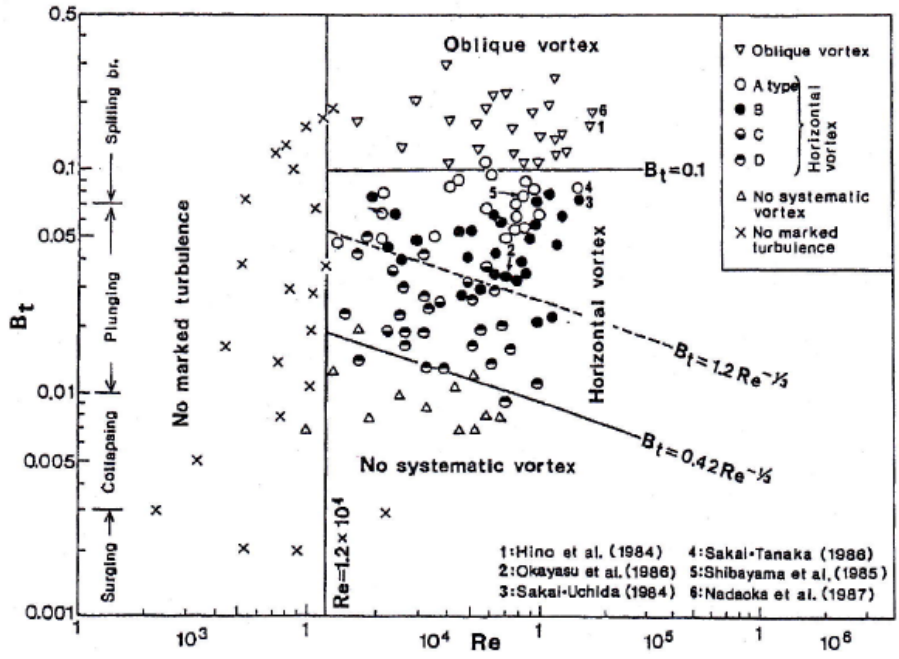

Figure 2.3 Conditions for the occurrence of various types of vortices (Zhang & Sunamura 1990).

The following relation was found by Zhang & Sunamura (1990):
Oblique vortices occur when Bt > 0.1 and the waves are thus spilling. Horizontal vortices occurred when 0.01 < Bt < 0.1 and the waves are thus plunging. When Bt < 0.01, there is

an initial vortex and then an incoherent mass as collapsing breaker. The parameter Bt was selected because the type of breaking waves is closely related to vortex types. Furthermore, Zhang & Sunamura (1990) subdivided the horizontal vortices into 4 types and two groups:

(1) type A (formation of a horizontal vortex that will change into oblique vortices) and type B (formation of horizontal vortices that will develop in sequence).

(2) type C (formation of a horizontal vortex that will disappear in a short time) and type D (formation of a horizontal vortex that will change rapidly to non-systematic vortices).

These were classified using the Reynolds number, for the occurrence of visible vortices the Reynolds number should be at least 1.2×10^4.

The five types of vortices (the oblique type and four horizontal types) were well distinguished on the Bt = Re plane and the horizontal vortices could be separated furthermore by their lasting time (Zhang & Sunamura 1990; figure 2.4).

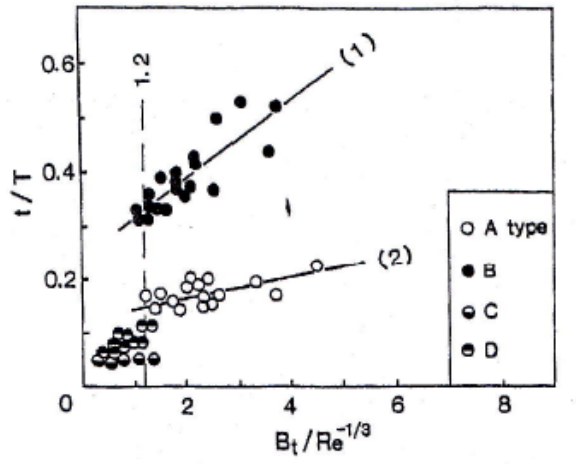

Figure 2.4 Lasting time of four types of horizontal vortices

According to Zhang et al. (1994), the vortices formed just after wave breaking can be classified into three types according to the direction of the vortex axis: an oblique vortex and two types of horizontal vortices (A and B-type horizontal vortices). The oblique vortex is like a tornado that has an obliquely stretched axis of rotation (figure 2.5a). The B-type horizontal vortex (figure 2.5c) has a horizontal axis of rotation, while the A-type horizontal vortex (figure 2.5b) is a mix between horizontal and oblique vortices: the horizontal vortex forms first in the upper part of the water column and then changes to the oblique vortex.

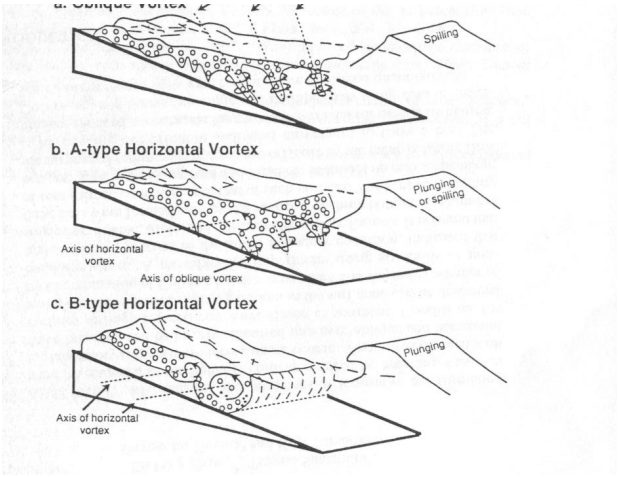

Figure 2.5 Three vortex types (Zhang et al. 1994).

So although Zhang et al. (1994) only distinguish between three types of vortices and Zhang & Sunamura have classified five types of vortices, these are largely the same, but Zhang et al. (1994) did not take the horizontal vortex types C and D into account.

From the phase-averaged turbulent velocities that are plotted in fig.2.6c and d it can be seen that coherent structures are present in a spilling breaker. The close resemblance of turbulent velocity fluctuations at different elevations indicates that a high degree of organization is present in the turbulent motion. Also a phase shift is visible that indicates that the turbulent motion spreads slowly downward (Ting & Kirby 1996). The structure of turbulence has many similarities in the outer and inner surf zone and is tied in a direct way to the breaking wave characteristics. The occurrence of spilling breakers is a necessary condition for oblique vortex formation (Zhang & Sunamura 1990). The wave breaking in a spilling breaker is confined to a region near the wave crest and the rate of energy transfer from wave to turbulence is relatively slow. The surface roller is therefore also confined to the region near the crest of the wave and therefore the size of the largest eddies is small compared to the local water depth. The turbulent velocity is also small compared to the local wave celerity and the surface-generated turbulence is spread slowly downward by turbulent diffusion (Ting & Kirby 1996).

In plunging breakers on the other hand, the structure of turbulence changes considerably from the outer surf zone to the inner surf zone. The length and velocity scales of the large eddies are determined by the rate of energy transfer from the wave motion to the turbulent motion and the size of the surface roller. Wave period, length

and velocity scales of the large eddies, and the local water depth are important parameters that define the temporal and spatial variations of turbulence intensity. In plunging breakers, the energy supply to the large eddies is much larger than in spilling breakers. The rate of energy supply is in the order of U^3/l, where l and U are the length scale and velocity scale of the large eddies. This means that the plunging breakers have larger length and velocity scales than the spilling breakers (Ting & Kirby 1996).

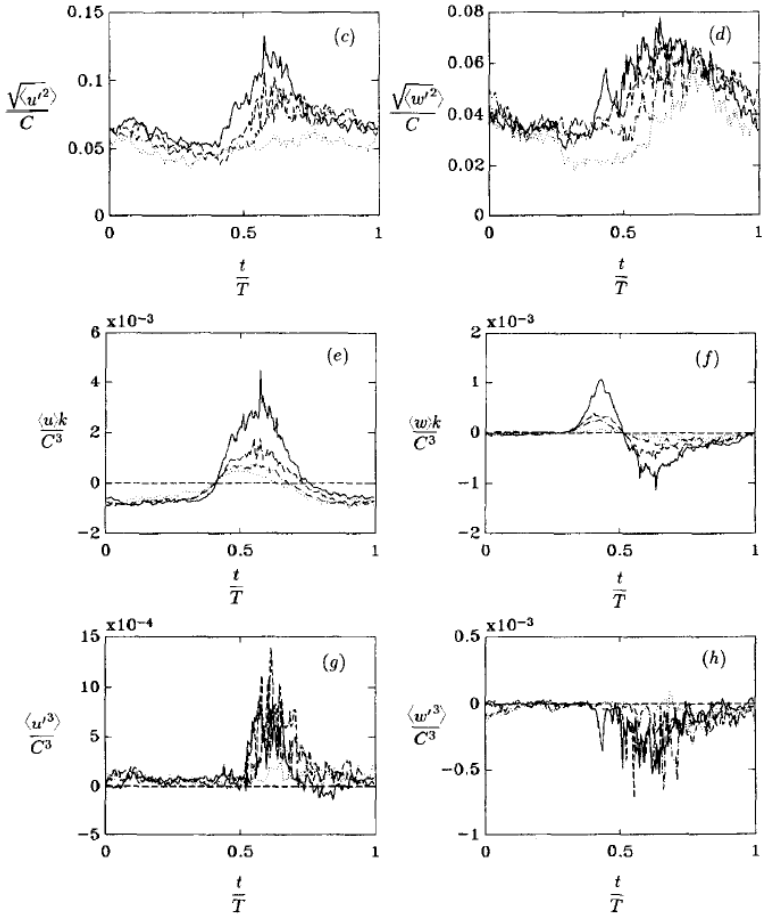

Figure 2.6 Turbulent kinetic energy observations (Ting & Kirby 1996). $(z-\bar{\zeta})/h$ = -0.2957 (_____) -0.4820 (- - -), -0.6683 (- . - .-), - 0.8857 (. . .).

The primary vortices generated in breaking waves are inherently unstable. One part of the wave crest might become unstable and curled over, while the rest of the wave front is still steepening. The longitudinal instability might be the result of uncontrolled upstream disturbance and/or side wall effects present in the flume. In figure 2.7, the transformation of a primary spanwise vortex produced by the beginning of breaking of a plunging regular wave on a plane slope. A transverse vortex can be seen in the left picture; the vortex tube is still intact. In the middle picture, instabilities have developed

near the left side wall and over the centre portion of the vortex tube. Observations of many repeated waves showed that these local deformations quickly grew in a cloud of air bubbles extending obliquely downward (right picture) (Ting 2008). On both sides of the aerated column, entrained air bubbles were observed to rotate in opposite directions indicating the presence of counter-rotating vorticity. After the wave had broken, similar bubble cloud structures emerged intermittently in space and time in a denser pattern as the wave propagated onshore. The experimental observations showed that spanwise instability could develop in the transverse vortex at incipient breaking. When this occurs, stretching and bending of the transverse vortex by the strong shear flow would lead to spontaneous production of streamwise and vertical vorticity. However, if the transverse vortex can reach the bottom quickly enough before the deformation has time to develop, as in the case of a strongly plunging breaker, the vortex motion might remain essentially two dimensional (Ting 2008).

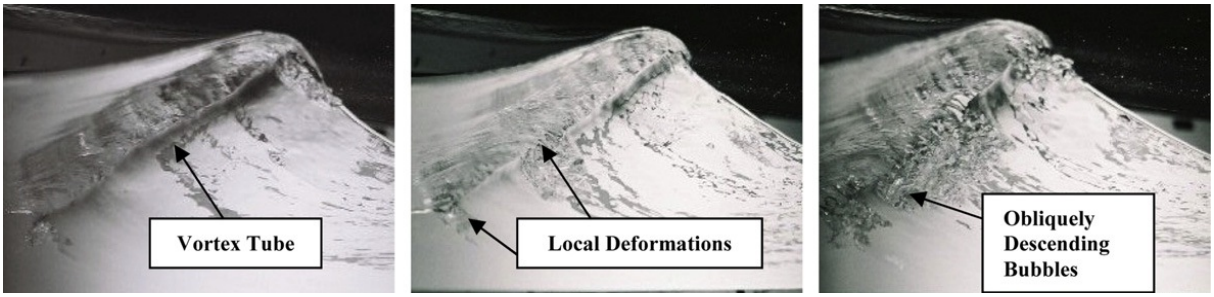

Figure 2.7 Incipient breaking of a plunging wave on a 1 in 50 plane slope. These pictures show the transformation of the primary spanwise vortex (Ting 2008).

I.2 Turbulent kinetic energy

I.2.1 Definition and calculation methods

During a wave breaking process, the wave energy is converted into two parts: the mean current energy and the turbulent kinetic energy. The turbulent kinetic energy can be obtained from the turbulent velocity fluctuations. In the nearshore, the velocity (u) can be decomposed into mean, wave-induced and turbulent component as follows:

$$u = \bar{u} + \tilde{u} + u', \qquad (6)$$

where an overbar denotes the time-averaged (mean) velocity, a tilde denotes wave-induced velocities and a prime denotes turbulent velocities. It is difficult to separate the wave-induced and turbulent components and there are several methods for this, so that the turbulent kinetic energy can be found. The time-averaged turbulent kinetic energy per unit mass ($\langle k' \rangle$) is defined as

$$\langle k' \rangle = 0.5(\langle u'^2 \rangle + \langle v'^2 \rangle + \langle w'^2 \rangle), \qquad (7)$$

where u, v and w are the cross-shore, alongshore and vertical velocities respectively (Scott et al. 2005). Three separation methods can be applied; the ensemble averaging methods, the high-pass filtering methods and the differencing method, these will be discussed below.

The ensemble averaging method can be used when regular waves are studied. The wave-induced velocity can be estimated by averaging the same point in the wave phase over many successive waves and the turbulent component can then be estimated using equation (6). The ensemble averaging method is the only well defined way of separating wave and turbulent motions for regular waves. Using this method, also large, low-frequency vortices, that are often neglected by other methods, can be recorded as turbulence. A limitation of this method is that it cannot be applied to truly random waves in the field (Scott et al. 2005). In the laboratory however, the ensemble averaging method can be applied to random waves by collecting many recordings of the same velocity time series at one location and averaging these recordings to obtain the wave-induced velocity.

The high-pass filtering method can be used when waves are not repeatable. This method separates the wave-induced and turbulent components of velocity by specifying a cut-off frequency separating the wave and turbulent time scales and then applying the standard filtering techniques to isolate the turbulent component. It can be difficult to

choose an appropriate cut-off frequency and it could be impossible to find one single cut-off frequency that separates these scales (Scott et al. 2005).

The differencing method can be applied to random waves, using the difference between the measured velocities from two closely spaced sensors to estimate the turbulent velocities. The turbulent velocities are computed based on the differencing and filtering method proposed by Feddersen and Williams (2007). In this method, the linear filtering is applied to all three directions (u, v and w) followed by the Trowbridge (1998) differencing strategy. The method requires input matrices (u, v and w) from two positions that are demeaned. The velocity at position 2 is transformed to position 1 and then differenced in u, v or w. The application of the high-pass filtering and differencing method will be discussed in more detail in chapter 4.4.

I.2.2 Time averaged, vertical structure, breaker type

In the surf zone, where waves are breaking, the turbulent kinetic energy is largest near the surface and decaying downward (George et al. 1994; Ting & Kirby 1996; Mocke 2001; Scott et al. 2005). This can be seen in figure 2.8, where the turbulent kinetic energy is shown as a function of height above the bed. This clearly shows that the turbulent kinetic energy is largest near the surface and decreasing downward. The large decrease in turbulent kinetic energy towards the bed corresponds with the fact that only a fraction of the turbulent eddies generated by wave breaking affect the bed.

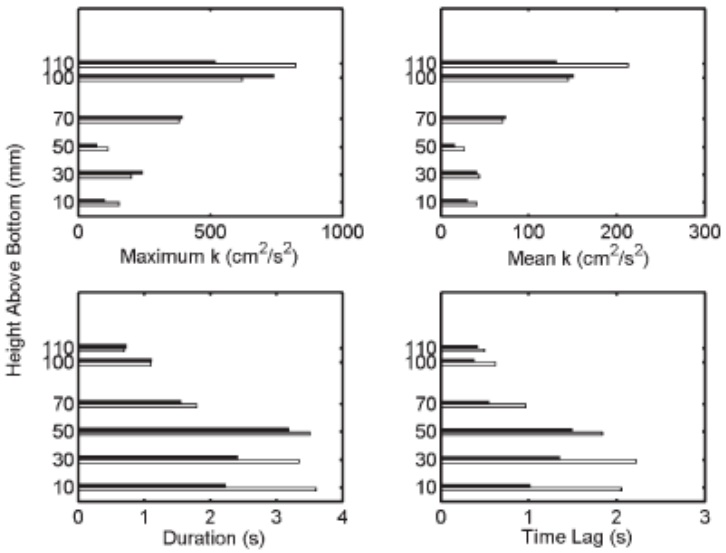

Figure 2.8 Mean (white bars) and standard deviation (black bars) of turbulent events properties (maximum value, mean value, duration and time lag) for k at different heights above the bottom (Ting 2006).

However, Scott et al. (2005) found that turbulence generated at the crest can be transported offshore and confined to a region near the bottom. This could lead to a maximum turbulent kinetic energy not at the wave trough level but near the bed. These events on the other hand, are probably episodic. In figure 2.8, also the duration and time lag (between the maximum value of k and the maximum value of <u>) are shown as a function of height above the bed. It can be clearly seen that the duration and time lag increase towards the bed as the turbulent kinetic energy decreases. This corresponds with the short duration and time lag found for intense turbulent events (which are mostly at near the wave crest) and the longer duration and time lag for weaker turbulent events (Ting 2006).

The surface roller in a spilling breaker is confined to a region near the crest of the wave (Ting & Kirby 1996). The relative height and period of the surface roller as a function of local water depth defines the characteristic turbulent generation and length scales (Mocke 2001). This shows the main distinction between turbulence under spilling and plunging breakers, where the surface roller and thus turbulent kinetic energy is much larger. In figure 2.9 the vertical profile of turbulence magnitudes for spilling and plunging breakers can be seen. The profiles are clearly different; the turbulence magnitude for the spilling breaker is largest near the surface and then rapidly decreasing downward. For the plunging breaker, the maximum is also located near the surface, but then the turbulence magnitude remains approximately the same in a large part of the water column and it is only slowly decreasing downward. This means that more sediment can be suspended, but because the vortices associated with plunging breakers are quite laminar (horizontal vortices), the upward mixing is limited.

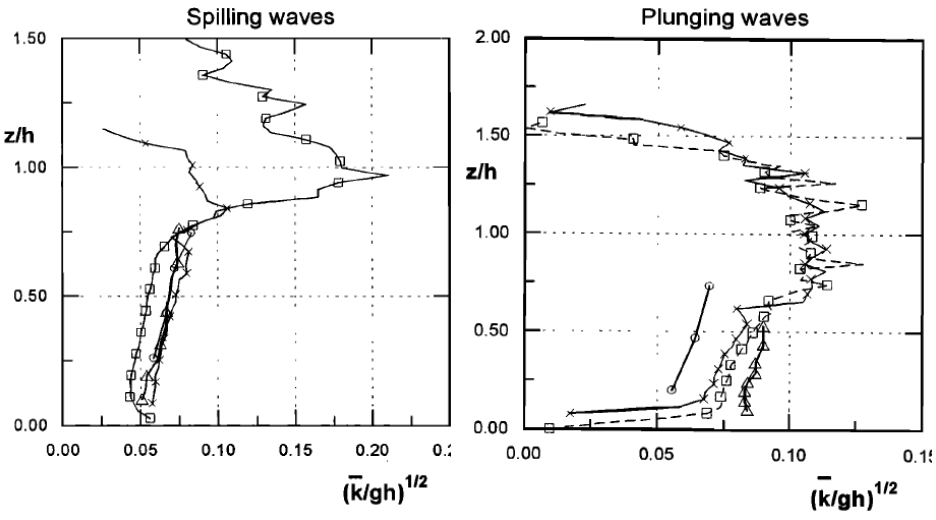

Figure 2.9 Comparison of turbulence magnitudes (Froude scaled wave-averaged turbulent kinetic energy $(k/gh)^{1/2}$) for spilling and plunging waves (Mocke 2001).

I.2.3 Cross-shore variation

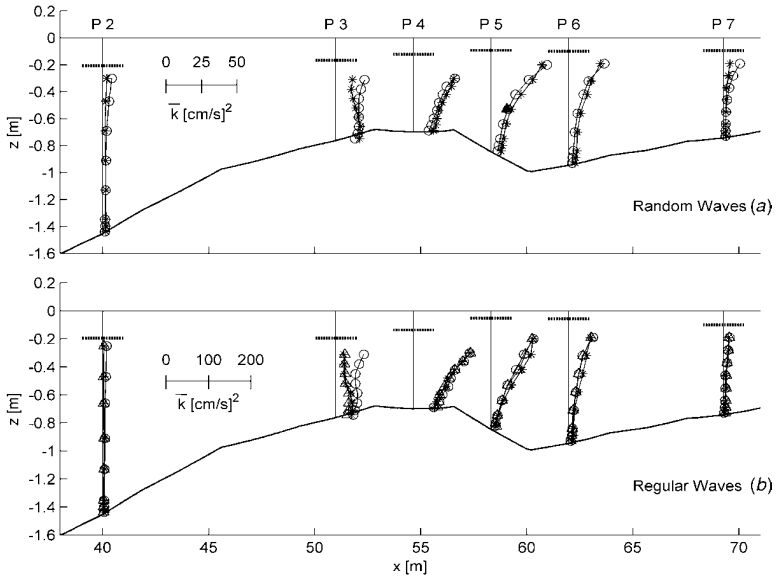

Figure 2.10 Cross-shore and vertical variation of k for the random and regular wave cases using ensemble averaging (Δ), high-pass filtering (O) and differencing (*) techniques (Scott et al. 2005).

Figure 2.10 shows a cross-shore profile of the vertical variation of the turbulent kinetic energy. Seaward of the breaking zone the turbulence is weak. The breaking-induced turbulence might not extend to the bed (Trowbridge & Elgar 2001), and the near-bed observed turbulence is dominated by near-bed processes (Feddersen & Trowbridge 2005). The turbulent velocities are highest in the crest portion of the wave near the surface, but the peak gradually shifts to the trough portion of the wave. This trend is more distinct in the inner surf zone and indicates that the turbulent kinetic energy is generated in the wave crest and spreads to the bed and that vertical mixing is slow (Ting & Kirby 1996).

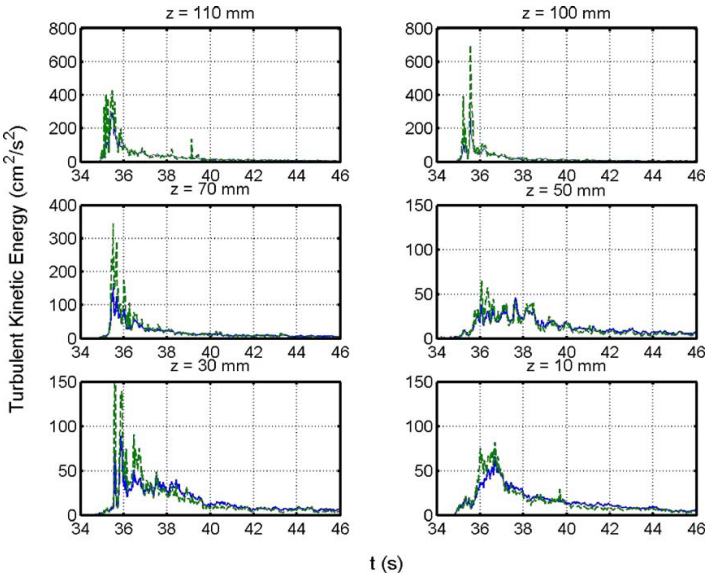

Figure 2.11 Ensemble-averaged turbulent kinetic energy bkN (solid line) and standard deviation (dashed line) under a broken solitary wave (Ting 2006).

Near the bed, turbulent events are more sporadic and turbulent kinetic energy is typically caused by a few large and intense events (Ting 2006; figure 2.11). The largest turbulent kinetic energy rates are clearly found near the breaking point at the bar crest. However, at location P3, which is a little more offshore, the maximum of turbulent kinetic energy is not located at the wave trough level, but near the bed, which suggests that turbulent kinetic energy has been transported from the breaking point offshore near the bed.

Near the breaking point, the turbulent kinetic energy can be significant throughout the water column (even 1 cm above the bed), but more onshore, the turbulent kinetic energy is confined to the upper part of the water column, which suggests that the significant turbulent kinetic energy throughout the entire water column is a localized feature near the wave breaking point (Scott et al. 2005). In figure

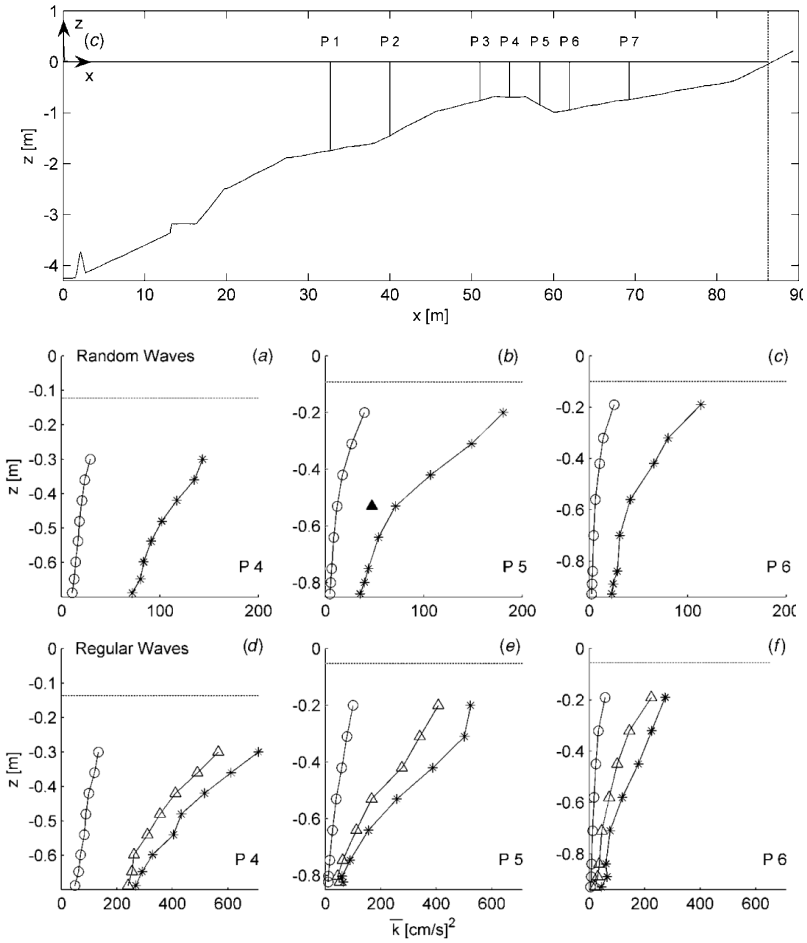

Figure 2.12 Vertical variation of k for random (a-c) and regular (d-f) waves at P4-P6 using ensemble averaging (Δ), high-pass filtering (O) and differencing (*) techniques. Trough level indicated by (---) (Scott et al. 2005).

2.12 the vertical variation of the turbulent kinetic energy can be seen for random and regular waves at 3 different cross-shore locations using the three methods described earlier. It can be clearly seen that the turbulent kinetic energy is largest near the wave trough and decreasing downward. This profile is stronger for the more onshore locations than for the location P4, which is located at the bar crest. At this point, the turbulent kinetic energy seems more consistent throughout the water column as said before. This increase of turbulent kinetic energy near the bed was probably not due to bottom boundary layer processes, but due to turbulence generated by breaking waves at the surface that was transported to the bed (Scott et al. 2005).

In the swash zone, the bottom turbulence plays a relative important role, depending on the kind of breaking and it is even dominant during the backwash. There is more interaction between free surface, bottom and turbulence, due to the limited water depth and furthermore, possibly very dense water/sand mixtures in the swash zone have to be taken into account (Longo et al. 2002)

I.3 Dissipation

I.3.1 Definition and calculation

Turbulence viscous dissipation in wave breaking has been considered a crucial factor in wave energy dissipation. The turbulent kinetic energy is damped through turbulence viscous dissipation. In this process, the energy of the fluctuating eddies under breaking waves is 'drained' due to viscosity and converted into heat (Huang et al. 2009). The dissipation can be calculated in various ways, which will be discussed below.

One of the first methods to compute turbulent dissipation was developed by George et al. (1994). The dissipation rate was calculated by finding the best fit $k^{-5/3}$ line through the wave number spectrum ($\Phi(\kappa)$), that was found from (8) and (9).

$$\Phi(\kappa) = \frac{\Phi(f)}{2\pi/U} \qquad (8)$$

$$\kappa = \frac{2\pi f}{U} \qquad (9)$$

$$\Phi(\kappa) = \alpha\varepsilon^{2/3}\kappa^{-5/3} \qquad (10)$$

This slope of the line is -5/3, because this is the scaling in the inertial subrange. This is the intermediate range of turbulent scales or wavelengths where the net energy coming from the energy containing eddies is in equilibrium with the net energy flowing to smaller eddies where it is dissipated. Thus the slope of the energy spectrum in this range remains constant and Kolmogorov (1962) has shown that this slope is -5/3.
The bulk dissipation rate per 512-s record was then estimated by George et al. (1994). The dissipation rates in the natural surf zone are highly intermittent and this produces an approximately lognormal distribution of dissipation rate. So then $z = \ln(\varepsilon)$ and the expected value is:

$$\langle\varepsilon\rangle = \exp\left(\mu + \frac{\sigma_{ln\varepsilon}^2}{2}\right) \qquad (11)$$

Where μ and σ^2 are the mean and variance of z.

Bryan et al. (2003) also found the dissipation rate by fitting a line to the observed spectrum $S_i(\omega)$

$$S_1(\omega) = \frac{9}{55}\alpha U^{2/3}\omega^{-5/3} \; and$$

$$S_3(\omega) = \frac{4}{3}\frac{9}{55}\alpha U^{2/3}\omega^{-5/3} \qquad (12)$$

and then averaging the resulting estimates of ε over the whole time series, so that the dissipation rate was found from

$$\langle \hat{\varepsilon} \rangle = \left(\frac{55}{9\alpha}\right)^{3/2} \left\langle \left[\frac{\hat{S}_1(\omega)}{\omega^{-5/3}\widehat{U}^{5/3}}\right] \right\rangle \qquad (13)$$

Where the angle brackets indicate the expected value over all the realisations of Si and U. In this case U is the mean of u_w over the subseries. This method of Bryan et al. (2003) is quite similar to the method of George et al. (1994).

Trowbridge and Elgar (2001) obtained estimates of dissipation from onshore ADVO data by applying an inertial range turbulence model to velocity spectra. The model was specialized for frequencies large compared with the dominant wave frequency, unidirectional waves, and conditions near the seafloor, where wave-induced vertical velocities have a very small effect on advection of turbulence. To simplify the analysis, the turbulence is assumed to be homogeneous and isotropic and to have a Kolmogorov spectrum.

$$E(k) = \alpha \varepsilon^{2/3} k^{-5/3} \qquad (14)$$

Where E(k) is the isotropic energy spectrum, k is the magnitude of the turbulent kinetic energy, α is the empirical Kolmogorov constant and ε is the dissipation rate. Burst-averaged velocity spectra P_{uu}, P_{vv} and P_{ww} were obtained by combining spectra from Hanning window 100-sample segments. The model representation of the sum of spectra of the two horizontal components of the velocity is:

$$P_{uu}(\omega) + P_{vv}(\omega) = \frac{21}{55}\alpha \varepsilon^{2/3} V^{2/3} \omega^{-5/3} I\left(\frac{\sigma}{V}, \theta\right) \qquad (15)$$

+ constant noise level

And the model representation of the spectrum of vertical velocity is:

$$P_{ww}(\omega) = \frac{12}{55}\alpha \varepsilon^{2/3} V^{2/3} \omega^{-5/3} I\left(\frac{\sigma}{V}, \theta\right) \qquad (16)$$

Where P_{uu} etc. are spectra, ω is radian frequency, equal to 2πf, where f is cyclic frequency, α is the empirical Kolmogorov constant, approximately equal to 1.5; V is the magnitude of the current; σ^2 is the variance of the wave-induced horizontal velocity; θ is the angle between waves and currents (Trowbridge & Elgar 2001).

The same model as Trowbridge & Elgar (2001) is used by Feddersen et al. (2007), and Gerbi et al. (2007). These two methods will be further discussed in Chapter 4.4.

A third method to compute the turbulent dissipation rate is defined by Huang et al. (2009), following Tennekes & Lumley (1972) as:

$$\varepsilon = 2\nu\langle s_{ij}s_{ij}\rangle = \nu\,\langle\frac{\partial u_i{}'}{\partial x_j}\left(\frac{\partial u_i{}'}{\partial x_j}+\frac{\partial u_j{}'}{\partial x_i}\right)\rangle \qquad (23)$$

This can then be expanded into 12 terms:

$$\varepsilon = \nu\left[2\,\langle\left(\frac{\partial u'}{\partial x}\right)^2\rangle + \langle\left(\frac{\partial u'}{\partial z}\right)^2\rangle + \langle\left(\frac{\partial w'}{\partial x}\right)^2\rangle + 2\,\langle\left(\frac{\partial w'}{\partial z}\right)^2\rangle + 2\,\langle\left(\frac{\partial u'}{\partial z}\frac{\partial w'}{\partial x}\right)\rangle + \langle\left(\frac{\partial u'}{\partial y}\right)^2\rangle \right.$$
$$+ \langle\left(\frac{\partial v'}{\partial x}\right)^2\rangle + 2\,\langle\left(\frac{\partial v'}{\partial y}\right)^2\rangle + 2\,\langle\left(\frac{\partial u'}{\partial y}\frac{\partial v'}{\partial x}\right)\rangle + \langle\left(\frac{\partial v'}{\partial z}\right)^2\rangle + \langle\left(\frac{\partial w'}{\partial y}\right)^2\rangle$$
$$\left. + 2\,\langle\left(\frac{\partial v'}{\partial z}\frac{\partial w'}{\partial y}\right)\rangle\right] \qquad (24)$$

From two-dimensional PIV (Particle Image Velocimetry) velocity measurements, five terms in the x-z plane, $(\partial u'/dx)^2$, $(\partial u'/dz)^2$, $(\partial w'/dx)^2$, $(\partial w'/dz)^2$, and $(\partial u'/dz)\,(\partial w'/\partial x)$ can be evaluated directly and the remaining terms may be estimated with various assumptions, as discussed in Huang et al. (2009). This method is only applicable when a lot of detailed data is available and thus can generally only be used for laboratory studies.

I.3.2 Vertical structure, scaling

The turbulent dissipation was measured by Feddersen et al. (2007) seaward of the surf zone at three different heights above the bed. Near the surface, the dissipation was maximum, indicating that the surface is an important turbulent source. At middepth, the dissipation was minimum and a factor of 2-2.5 smaller than the upper one. A secondary maximum was near the bed. The highest maximum could be due to whitecapping breaking-wave generated turbulence, while the lower maximum could be due to bottom boundary layer generated turbulence. This two-maxima dissipation could be seen as combination of the deep-water breaking wave dissipation and the continental shelf bottom boundary layer dissipation. In figure 2.13 the observed vertical structure of dissipation is shown and figure 2.14 shows the non-dimensionalized dissipation of different experiments, so that these could be compared. These clearly show the pattern described above. The highest maximum at the upper location, the minimum at middepth and the secondary maximum near the bed.

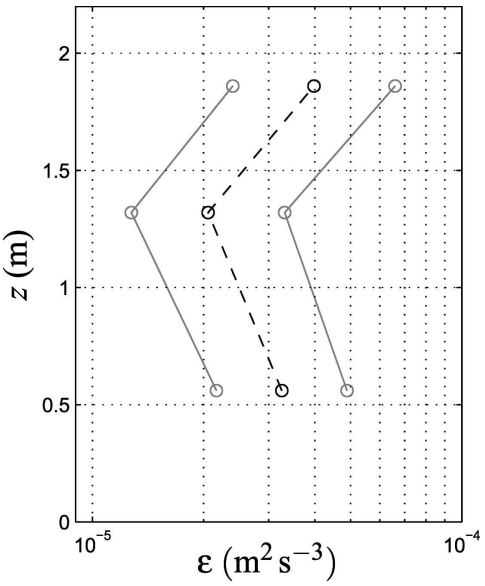

Figure 2.13 Dominant vertical structure mean (dashed) and standard deviation (solid) (Feddersen et al. 2007).

The upper maximum suggests a surface source of turbulence (surface boundary scaling: u_*^3/kz' (this scaling is for dominance of wind, not of breaking waves)). For a surface boundary scaling and thus a surface source of turbulence, a large dissipation rate would be expected at the surface, which is decaying downward. Therefore Feddersen et al. (2007) compared these measurements to previous measurements. The measurements for the lower maximum were compared to previous studies of bottom boundary layer scalings for dissipation (bottom boundary scaling: u_*^3/kz). For the bottom boundary

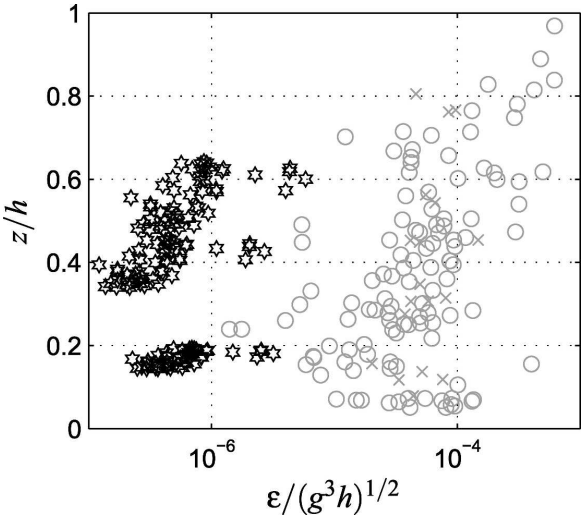

Figure 2.14 Surf zone-scaled dissipation as a function of normalized depth, different observations (Feddersen et al. 2007).

scaling, a large dissipation rate would be expected at the bed, which is decreasing upward quickly. The observed dissipation rates appear to be larger than the bottom boundary layer scaling, although the two are correlated (figure 2.15).

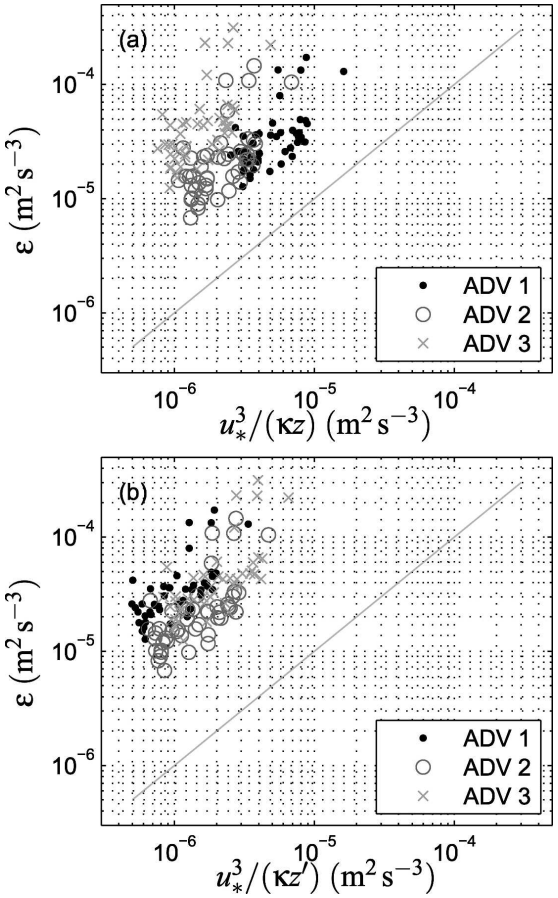

Figure 2.15 Observed ε vs (a) bottom boundary layer scaling u_*^3/kz and (b) surface boundary layer scaling u_*^3/kz' at ADVs 1 (dots), 2 (circles) and 3 (crosses) (Feddersen et al. 2007).

Thus, although correlations are high, it appears unlikely that these boundary layer scalings that neglect breaking-wave-generated turbulence are applicable. The observed dissipation does not follow the surfzone or the bottom boundary layer scaling as was explained above. The downward diffusion of the turbulent kinetic energy is balancing the dissipation. However, in stead of decreasing with depth, at the lowest ADV the dissipation increases, due to the decrease in the turbulent length scale near the bed. Thus, in the nearshore region seaward of the surfzone, whitecapping breaking-wave-generated turbulence can be significant and may dominate over boundary layer processes (Feddersen et al. 2007).

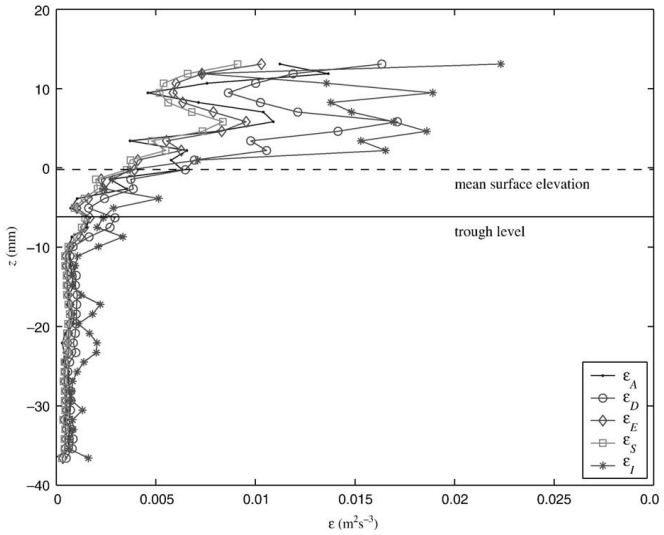

Figure 2.16 Estimates of turbulence dissipation rate using different estimation methods based on different assumptions, see the appendix of Huang et al. (2009) for specifications.

The turbulent dissipation in the surf zone below the trough level may be associated with the coherent descending turbulent structures from the crest region and the large scale motion of turbulent eddies that dominate the dynamics of turbulent dissipation in the surf zone (Huang et al. 2009). The vertical profile of the turbulent dissipation rate shows an exponential decay from the crest to the bed (figure 2.16). Note that the scale of the experiment of Huang et al. (2009) is in the order of millimetres, so possibly scaling problems can arise. George et al. (1994) found that the dissipation rates are smallest where less than 5% of the waves were broken. When the fraction of broken waves increases, the dissipation rate also increases.

From the temporal variations of turbulent velocities it could be that the dissipation rate is slow in spilling breakers, and thus turbulent energy does not die out between breakers but is uniform in time (Ting & Kirby 1996). This is also supported by the small amount of turbulent dissipation relative to total energy dissipation.

I.3.3 Cross-shore structure

In the nearshore region seaward of the surfzone, whitecapping breaking-wave-generated turbulence can be significant and may dominate over boundary layer processes (Feddersen et al. 2007). In the outer surf zone an equilibrium exists between turbulent production and dissipation (Sou et al. 2010). Initially, in the roller region at the frontal wave crest, significant turbulent dissipation occurs and then spreads to the entire crest region after the establishment of a turbulent bore (Huang et al. 2009). The

dissipation rate is largest at the incipience of wave breaking, decreases rapidly in the bore-established region and then decreases gradually in the inner surf zone (Huang et al. 2009). However, the turbulence dissipation rate in the entire surf zone is relatively small in comparison to the total dissipation rate (the decrease in wave height). In the outer surf zone, the turbulent dissipation is 1% of the total dissipation and in the inner surf zone, the turbulent dissipation is 10-12% of the total dissipation (figure 2.17). Dissipation rates found by Bryan et al. (1993) were also not large enough to explain the reduction in wave height that is expected in the surf zone. Approximately 90% of the dissipation must occur very near the water surface or close to the bed, above and below where the measurements were taken. Observed dissipation rates increased steadily shoreward as the probability of breaking increased. Although not observed, here dissipation rates should decrease with water depth once all the waves are broken.

Inside the surf zone, the beach slope was highly correlated with offshore wave height and so it is impossible to determine objectively whether the dissipation rate was dependent on beach slope or significant wave height. This codependency of beach slope and significant wave height was mainly due to changing beaches to assess the dependency of dissipation rate on changing beach slope (Bryan et al. 2003). Once the bore front has passed, the turbulence production is much smaller than the turbulent dissipation in the inner surf zone (Sou et al. 2010).

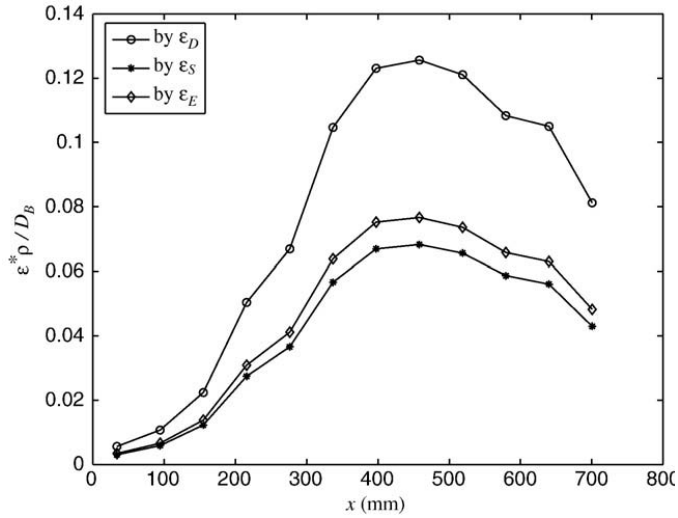

Figure 2.17 Ratio of the turbulence dissipation rate to the total energy dissipation rate. The results were calculated by averaging the quantities through the fifth to the seventh breaking waves. The "shoreline" is located at approximately x=700 mm, at x=0, the measurements start. The different lines were calculated using different assumptions for the dissipation estimation, for specifics see the appendix of Huang et al. (2009).

The vertical structure of cross-shore orbital velocities observed by Raubenheimer et al. (2004) in the swash zone of a low-sloped, fine-grained beach is approximately logarithmic within 5 cm of the bed. Turbulent dissipation rates are consistent with previous estimates in the inner surf zone, and increase with decreasing water depth in the swash zone. During the backwash phase, dissipation is dominant in the inner surf zone and the swash zone is primarily a dissipater of energy (Sou et al. 2010). Wave breaking is probably important to near-bed turbulence in the swash and inner surf zones (Raubenheimer et al. 2004).

II. Sediment suspension

II.1 High concentration due to turbulence

Suspension of sediment is highly dependent on breaking wave processes that were discussed above. The amount of turbulent kinetic energy (that penetrates to the bed) is important for the suspension of sediment. Furthermore, the vortices induced by breaking waves have a large influence on the vertical distribution of the suspended sediment concentration.

II.1.1 Importance of turbulence

Ogston & Sternberg (2002) found suspended sediment concentration profiles from wave basin experiments (figure 2.18). These clearly show that the suspended sediment concentrations are much higher under broken waves, especially higher up in the water column. This suggests that breaking of waves is very important for the mixing of sediment upward into the water column.

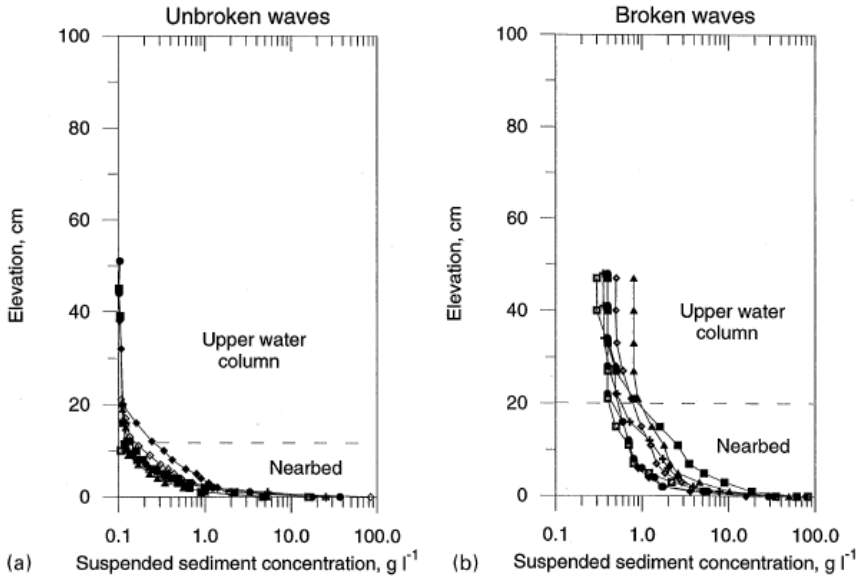

Figure 2.18 DUCK94 profiles of time-averaged suspended sediment concentration for (a) unbroken wave data runs, and (b) broken wave data runs. The dashed line in both panels represents the approximate location of the top of the nearbed region (Ogston & Sternberg 2002).

To find the turbulent velocity signal from the total vertical velocity signal is not easy. The vertical wave velocity variance (w_{rms}^2) is found from linear theory as:

$$\widetilde{w}^2 = \left(\frac{2\pi\sigma_\eta}{T_p}\frac{z_m}{\bar{h}}\right)^2, \qquad (25)$$

where σ_η is the standard deviation of the surface elevation time series, T_p is the peak spectral wave period, z_m is the measurement height above the bed and h is the mean water depth. The maximum values found from this method are far smaller than the observed vertical velocities associated with large vortices. Therefore, it is assumed that within the surf zone the wave contribution to vertical velocity w is negligible ($w' >> \tilde{w}$) and thus $w^2 \approx w'^2$ (Aagaard & Hughes 2010). A fixed vertical velocity threshold for breaker vortex occurrence was employed. This was selected as w_c = 0.2 m/s, which is 50% larger than the maximum vertical velocity observed under non-breaking waves. A window around w_c needs to be applied, due to the response time. Coherent velocity structures associated with breaker vortices were identified when the magnitude of |w| exceeds the pre-defined threshold velocity $|w_c|$. The concentration of sediment in the water column contributed by breaker vortices was assessed by computing the instantaneous vertical (upward) sediment flux, w(t)c(t). The total upward flux at a specified OBS-sensor, q_{tot} over a time-scale T, corresponding to the length of a time series is:

$$q_{tot} = \sum_{t=1}^{T} w(t)c(t); w > 0 \qquad (26)$$

and the flux caused by breaker vortices is:

$$q_{vx} = \sum_{t=1}^{T} w(t)c(t); w > |w_c| \qquad (27)$$

where w(t)c(t) is the instantaneous upward sediment flux, w is the vertical velocity and w_c is the threshold value for breaker vortex occurrence. In figure 2.19 the importance of breaking wave turbulence for sediment suspension is shown. In figure 2.19A the relative fraction of sediment suspended by breaker vortices (q_{vx}/q_{tot}) is plotted against the run-averaged turbulence intensity (w_{rms}^2). The ratio q_{vx}/q_{tot} represents the relative contribution of local breaker vortices to the total sediment concentration (Aagaard & Hughes 2010). It is clearly shown that the sediment suspended by breaker vortices increases with the turbulence intensity, with high ratios up to 88%. In figure 2.19B the relative fraction of sediment suspended by breaker vortices is plotted against the relative wave height (H_s/h). Some correlation is visible, but this is not very strong. The sediment suspension seems to be quite independent of relative wave height. At high relative wave heights, an increase in sediment suspension by breaker vortices is seen.

However, at a relative wave height of approximately 0.5-0.6, the range of sediment suspension by breaker vortices is very large (from 10-80%).

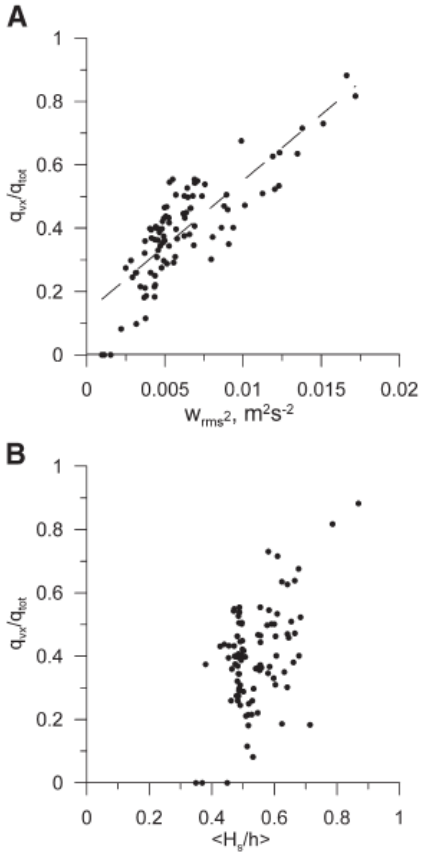

Figure 2.19 The relative fraction of sediment suspended by breaker vortices (q_{vx}/q_{tot}), plotted against A) run-averaged turbulence intensity and B) relative wave height (Aagaard & Hughes 2010).

Scott et al. (2009) on the other hand, found that sand suspension events caused by a steep wave and locally generated breaking wave-turbulence only account for 33% of the total number of high concentration events under erosive conditions. During accretive conditions, this percentage was down to only 15% of the total number of high concentration events. This would mean that a large amount of sediment transport under breaking waves is due to bottom-boundary layer processes and advection.

In figure 2.20 the results of a model run are shown at three different time steps (t1-t3) that are shown in the upper panel (Scott et al. 2009). The right column shows the model results for the predicted sediment concentration and the observed sediment concentrations. The black solid line gives the model results that included the breaking wave-turbulence, while the red dashed line gives the model results that do not include the breaking wave turbulence. The model used was a one-dimensional vertical two-

phase model for sand transport that was modified to take measured breaking wave turbulence quantities as top boundary conditions to simulate the effect of breaking wave turbulence on bottom sediment transport. The blue circle symbols are the measured concentrations. As can be seen, during high turbulence events, the model represents the measurements very well if the breaking wave-turbulence is included, while the results are very different if this is not included. This suggests that breaking wave-induced turbulence is very important for sediment suspension throughout the water column near breaking point (Scott et al. 2009).

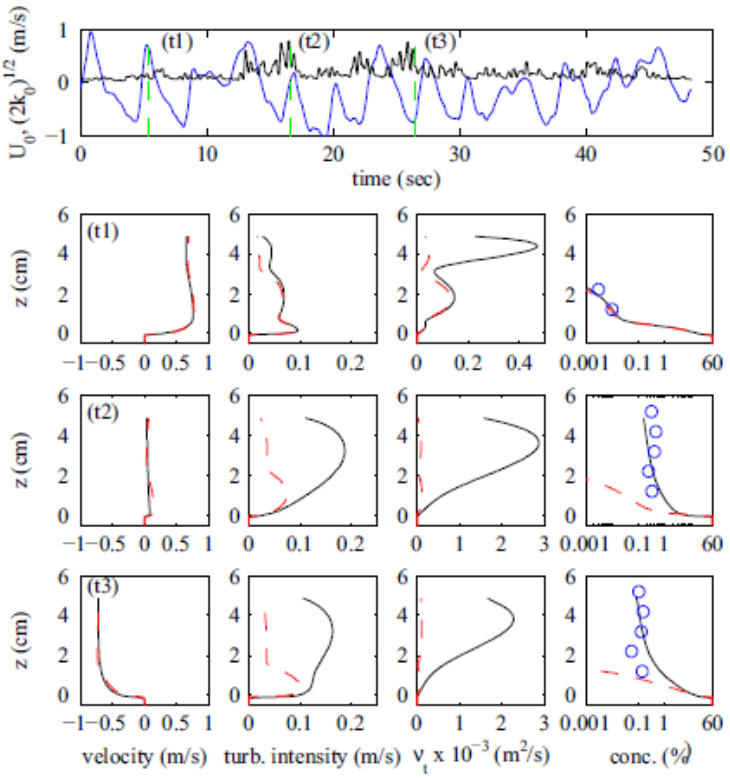

Figure 2.20 Two-phase model results during erosive conditions. Lower panels: model results for instantaneous fluid velocity, turbulent intensity, eddy viscosity and sediment concentration (Scott et al. 2009).

II.1.2 Breaker type

Plunging breakers are significantly more efficient in suspending sediment than inner surf bores and spilling breakers (Aagaard & Hughes 2010). They are responsible for a greater proportion of suspended load, longshore and cross-shore flux of sediment than bores, spilling waves and unbroken waves (Beach & Sternberg 1996; figure 2.21). The large coherent vortex structures under plunging waves that impinge occasionally on the seabed, increase the local instantaneous bed shear stress by several orders of magnitude

compared to conditions under shoaling waves, and about one order of magnitude compared to surf bores. Therefore, plunging breakers have a major effect on the mobilization of sediment and the surface-generated turbulence at wave crests is critical to the upward sediment flux (Aagaard & Hughes 2010). As explained above, plunging waves do set more sediment in suspension near the bed, but because of the horizontally oriented vortices associated with this type of waves the upward mixing is less efficient (Voulgaris & Collins 2000). The opposite is valid for spilling waves. These set less sediment in suspension near the bed, but because of the oblique vortices associated with spilling waves, they are much more efficient in the vertical mixing. The reference concentration and mixing parameter are both highly correlated with the wave breaking type, which shows the importance of breaking wave types for sediment suspension (Voulgaris & Collins 2000).

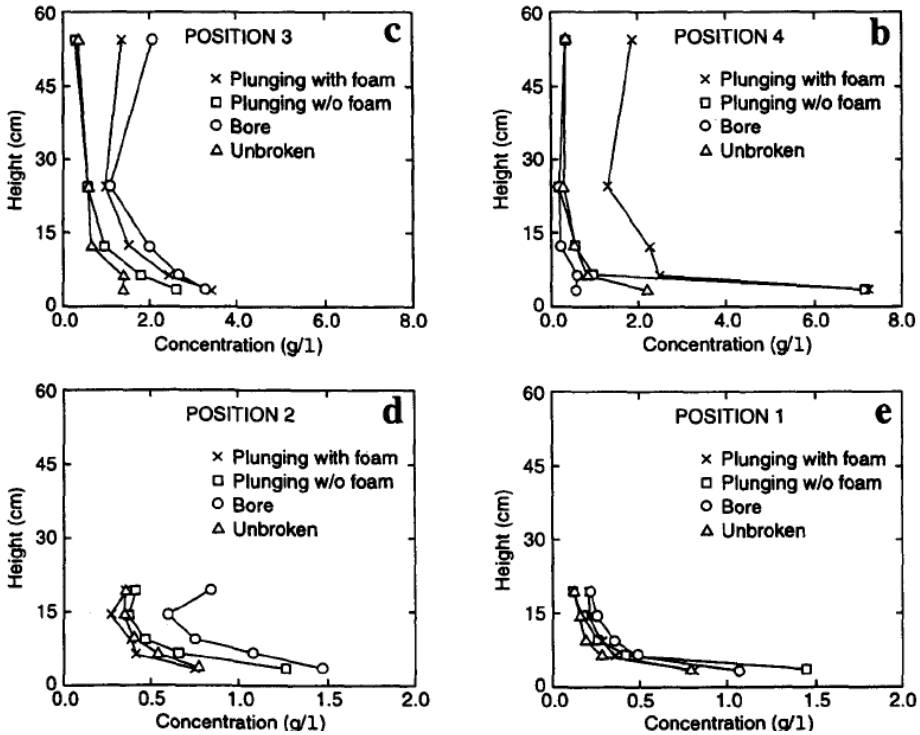

Figure 2.21 Observed suspended-sediment distribution across the surf zone as a function of wave type at different positions (Beach & Sternberg 1996).

II.1.3 Cross-shore variation

The sediment concentration in the surf zone at the wave crest and over the entire vertical water column is strongly determined by the turbulent intensity (up to 88%) (Aagaard & Hughes 2010) and is furthermore dependent on the distance from the breakpoint (Beach & Sternberg 1996), because the turbulent kinetic energy differs

strongly in the cross-shore direction. Close to the breakpoint, the turbulent kinetic energy is penetrating to the bed, while further away from the breakpoint, much less turbulent kinetic energy can reach the bed. Suzuki et al. (2007) found that at the offshore side of the wave breaking point, sediment was picked up uniformly in the longshore direction. However, after the wave breaking point, sediment pickup occurred intermittently in the longshore and cross-shore directions. Major eddies, or vortices, begin to form upon breaking. Initially, wave orbital motions (potential flow patterns) dominate the velocity structure and wave shape. However, as the wave breaking process progresses, orbital velocities are reduced and eddy motions and associated turbulence dominate the wave velocity field (Yu et al. 1993). The consequence of this is that under breaking waves, the sediment suspension is highly intermittent in time, as was also found by Suzuki et al. (2007), while during non-breaking conditions, the sediment suspension is more uniform. This suggests that the concentration signal is irregular in time due to breaker-induced turbulence, while it is more uniform in time when bed-generated turbulence is dominant.

During the passage of the bore front, high values of suspended sediment concentration and turbulent kinetic energy occur almost simultaneously, suggesting bore turbulence to be a possible sediment transport mechanism. Little suspended sediment is observed in the water column after the turbulent kinetic energy peak, suggesting that sediment might quickly settle out behind the bore. Bore turbulence probably has a real effect on sediment transport in the swash and inner surf zones, and can therefore not be ignored (Butt et al. 2004).

Suspension events in the swash zone are characterised by a distinctive temporal structure. High concentrations seem to be associated with high bed shear stresses and turbulent kinetic energy generated by the rapidly accelerating flows at both the start and end of the uprush and backwash. It seems likely that high concentrations during the uprush phase are controlled mostly by intense turbulence and high stresses associated with the front of shoreward propagating swash bores (Osborne & Rooker 1999).

II.2 Direction of transport

Scott et al. (2009) determined the direction of enhanced transport due to turbulence by the relative timing between the breaking wave turbulence events and the wave phase. As the time lag between the appearance of a high velocity turbulence event and a high

concentration event was expected to be very short, a direct correlation between measured wave velocity and turbulence can possibly be a good indicator for the direction of sediment transport due to a sand suspension event caused by breaking wave-turbulence. In figure 2.22a the measured time-series of wave velocity and turbulence are shown. This shows that high velocity turbulence events are in this case mostly correlated with the negative phase of the wave velocity. This can be seen for example at time steps t=22s and t=26s. So in the case of this time series, the correlation between high velocity turbulence events and wave phase seems to be negative and thus the turbulence enhances the wave-induced offshore transport. However, another time series is shown in figure 2.22b, again with the turbulence and the wave velocity. In this case, the turbulence events are positively correlated to the wave phase, which can be seen for example at t=35s. This positive correlation suggests that the turbulence enhances the wave-induced onshore transport in this case. So this shows that the enhanced onshore or offshore transport due to breaking wave-turbulence depends on the timing of the occurrence of high velocity turbulence events relative to the wave phase (Scott et al. 2009). Scott et al. (2009) found that about $^2/_3$ of the high breaking wave turbulence events appeared to be negatively correlated with the wave velocity. This implies that the breaking wave turbulence enhances the wave-related sediment transport offshore. However, also quite a large amount of the breaking wave turbulence events were positively correlated, which suggests that also onshore transport is enhanced at times. Besides the wave-related transport, the increased sediment suspension can also have an influence on the current-related sediment transport. As the (cross-shore) current is mostly offshore directed near the bed, the increased suspension of sediment due to turbulence is expected to increase the current-related offshore transport.

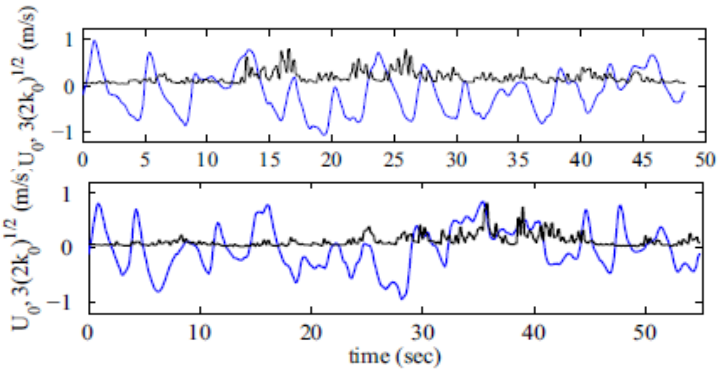

Figure 2.22 two measured time-series of wave velocity and turbulence (Scott et al. 2009)

3. Objectives, hypotheses and research questions

Two types of vortices are associated with wave breaking: oblique and horizontal vortices. The turbulent kinetic energy is generally largest near the surface and decreasing downward, furthermore it is largest near the breakpoint and decreasing towards the coast. The turbulent kinetic energy profile is highly dependent on the breaker type.
The turbulent dissipation is also maximum near the breakpoint and near the surface.

Plunging waves have a major effect on the suspension of sediment, but because of the horizontally oriented vortices, the upward mixing is less efficient. Spilling waves on the other hand, have less energy to suspend the sediment, but because of the oblique vortices, they are much more efficient in the vertical mixing. The suspension of sediment by turbulence probably enhances the offshore wave-related sediment transport.

Main objective

To study the downward spreading of turbulence and its influence on the sediment suspension.

- Study the relation between (surface generated) turbulence and sediment suspension.
- Study the dependence of turbulent kinetic energy on wave height and relative position in the surf zone.
- Study the influence of wave height on turbulent dissipation.
- Study the dependency of the turbulent dissipation profile on high energetic conditions.
- Study the influence of the wave conditions on the sediment suspension due to turbulence

What process causes the downward spreading of turbulence (during different conditions)? Although recognised as the dominant mechanism for sediment suspension in the surf zone, the enhanced mixing due to breaker turbulence is presently poorly quantified. It is unknown why sediment suspension is strong under some waves and weak under others. When the wave height changes, this can influence the turbulent kinetic energy because the (intensity of) breaking also changes.

The dissipation profile was found to have maxima near the surface and the bed outside the surf zone, while it showed an exponential decay in the surf zone. For the relative importance of turbulent dissipation for total energy dissipation various results were found. Some found that is was very important, while other found that it had only a minor influence.

Hypothesis

Turbulence generated at the sea surface penetrates through the water column and determines sediment suspension (rather than turbulence generated at the bed).

Research questions

- Is turbulence generated at the surface spreading downward to the bed?
- Does turbulent kinetic energy increase over the vertical profile during more intense breaking conditions (larger relative wave heights)?
- Does the turbulent dissipation increase during higher energetic conditions?
- Does the profile of turbulent dissipation change during higher energetic conditions?
- Can sediment suspension under breaking waves be related to turbulence?
- And if so: is it also dominated by surface-generated turbulence?

4. Methods

4.1 Instruments

A 6-week field experiment was conducted at Ameland, on the North Sea coast in September and October 2010. The Ameland coast is a 25-km-long east-west oriented coast between the Borndiep tidal inlet to the west and the inlet between Ameland and Schiermonnikoog to the east. Ameland beach is a very low-sloping beach (1:80) with an intertidal bar. The research location is located at the northwest side of the island, a beach facing the North Sea (Figure 4.1). The research area is at the seaward side of a very wide beach on which embryo dunes are forming. Seaward of the research area, towards the northwest, an ebb-tidal delta is located, which influences wave propagation toward the beach. During high-energy conditions waves break on the ebb-tidal delta and this thus limits wave height on the beach.

Figure 4.1 Research site on Ameland (in the red box)

An instrumented rig (Figure 4.2) was positioned at the neap low tide level to measure vertical profiles of the water motion (from turbulence quantities to mean currents), wave characteristics and water depth, seabed configuration (absence/presence ripples), and sediment concentration. The instruments used are three single-point, downward-oriented, Acoustic Doppler Velocimeters (ADV) placed at different heights above the bed to measure 3D mean and oscillatory flows and to estimate turbulence energy and its dissipation. The three ADVs were fitted with pressure, temperature, and pitch and roll sensors, as well as a compass, and had their own logger that sampled each instrument at 10 Hz in a burst of 29 min, each half hour. The initial vertical distance between the lower (ADV1) and middle (ADV2) sensor was 0.20 m and between ADV2 and the upper (ADV3) sensor was 0.30 m. Furthermore, 5 Optical Backscatter Sensors (OBS) were deployed in an vertical array to measure sediment concentrations. These OBSs were

measuring at 4 Hz continuously during high water and all five of them were positioned within 15 cm, with the lowest one at approximately 3 cm above the bed. Finally also a ripple sensor was deployed to determine the absence or presence of ripples. During high water, this ripple sensor made a scan of the bed every 5 minutes. The construction of the instrumented rig and the positioning and orientation of all instruments was such, that the disturbance of the flow field and of the seabed by the instruments themselves, the rig and by its power and logging canisters was minimized. The waves at the Ameland beach were expected to be mostly incident from the north to northwest and thus the alongshore currents to flow to the east. Therefore the instruments were placed at the northwestern side of the rig, while all the power and logging canisters were placed to the south.

Figure 4.2 Instrumented rig deployed at the neap low-tide water level during the Ameland 2010 field experiment.

4.2 Initial data processing

The quality control of the ADV velocity series was done using the guidelines in Elgar et al. (2005) and Mori et al. (2007). A threshold backscattered signal amplitude of 100 was used and series with signal amplitudes less than 100 during more than 5% of the time were assumed not to be submerged during the entire burst and were rejected for further processing. Elgar et al. (2005) used a threshold of 1%, while Feddersen (2010) used 10%. The time series that remained, were despiked using a two-step velocity despiking procedure. The first step was to reject the beam velocities with a correlation lower than

the critical correlation, which was calculated using the method of Elgar et al. (2005). The correlation threshold for swash- and surfzone data is $0.3 + 0.4\sqrt{(F_s/25)}$, where F_s is the sampling frequency. For a sampling frequency of 10 Hz, this holds that the correlation threshold is 55%. So all beam velocities with a correlation smaller than 55% were rejected and interpolated over, as discussed in Elgar et al. (2005). The beam velocities were then converted into the orthogonal coordinate system, which was then rotated into cross-shore u, alongshore v and vertical w velocity, with positive u directed onshore, positive v to the east and positive w upward. The second step of the despiking was then to depike the u, v and w series with the phase-space method of Mori et al. (2007). The spikes that were detected using this method were interpolated over again. This two-step despiking method was used because spikes in the beam velocities did not always coincide with low correlations. The method of Elgar et al. (2005) does not use the number of points with low correlations as a criterion for rejecting data runs, because of the variable quality of time series with similar numbers of low correlation points. The applied interpolation method to fill data gaps will bias low turbulence fluctuations. Results in Feddersen (2010) indicate that the magnitude of this bias is likely to be minor for fractions of bad correlation points lower than about 10-15%.

The 5-fold STM array stores measurements in mV and therefore has to be calibrated into kg/m^3. A calibration-polynomial function of any order could be used to relate mV to concentration. In practice, order = 2 suffices. The coefficients of the polynomial curve were determined in a circulation falicity using the sediment at the rig. The average grain size at the field experiment location was about 200μm.

4.3 Experimental conditions

The rig was deployed from 23 September (yearday 266) until 1 November (yearday 305) 2010. The offshore wave and water level conditions that were observed during the campaign are shown in Figure 4.3. During the field experiment, several storms were encountered. First of all, on yearday 268/269 waves peaked at a significant wave height Hs of about 3.5m (Fig.4.3a) with a period of almost 8 s (Fig.4.3b). Afterwards, a calmer period started, which lasted for approximately 20 days. During this period the wave height was generally below 1 m and the wave period was around 4 s. This calmer period was followed by a higher energetic period with an offshore significant wave height that was mostly around 3 m and peaked at 6 m on yearday 297 with a wave period of 8 s.

Both these storms/higher energetic periods were during spring tide, which has a range of about 2.5m, while during neap tide (range ~1m) the conditions were low energetic (Fig.4.3d). The red line in figure 4.3d represents the predicted water level, while the black line represents the measured water level. These are mostly the same, but during high energetic conditions the water levels are sometimes higher than predicted (due to wave set-up). During most of the experiment, and especially during the high energetic conditions, the waves were incident from the northwest (large angle of incidence). The angle of incidence from the offshore waves is shown in Figure 4.3c. An angle of 0 corresponds to waves from the north; an angle of 90 means waves from the east and an angle of 270 corresponds to waves coming from the west.

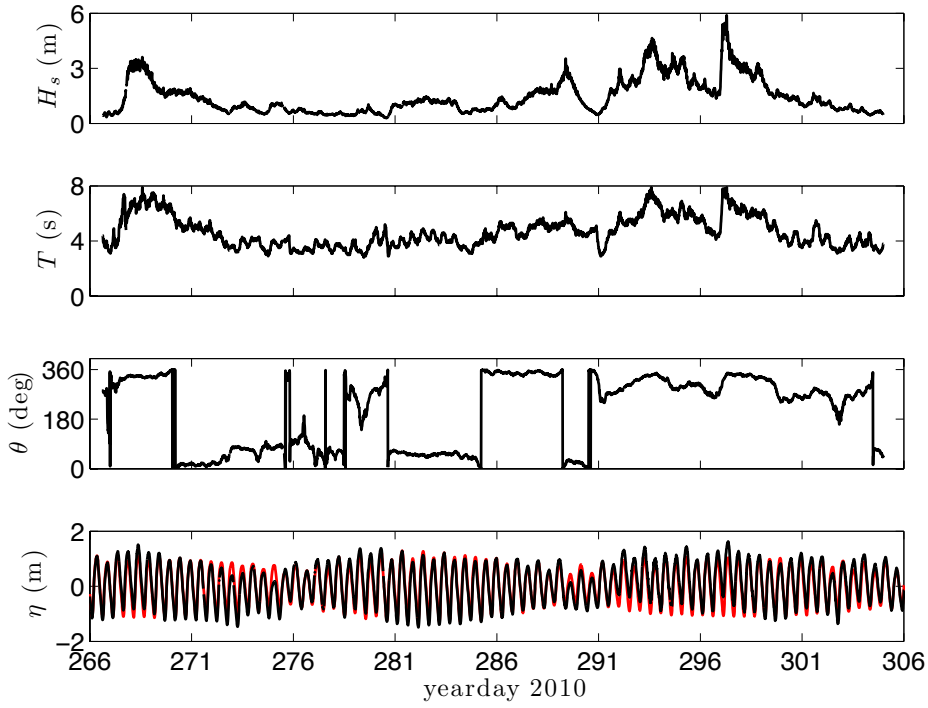

Figure 4.3 Offshore (a) significant wave height H_s, (b) wave period T, (c) angle of incidence with respect to North, and (d) water level with respect to MSL (predicted = red, measured = black). Wave parameters in (a)-(c) were measured by a wave buoy located in about 21.5m depth, about 2 km offshore.

The wave and water level conditions at the rig during the entire field experiment are shown in Figure 4.4. The sea-swell (0.04-1Hz) significant wave height Hs varied mostly with the local water depth (Fig.4.4a and 4.4b) and did not depend on the offshore significant wave height. The ratio of significant wave height tot water depth at the rig varied between 0.2 and 0.75 and was mainly around 0.5 (Fig.4.4c). The infragravity (0.004-0.04Hz) significant wave height at the rig did generally not depend on local water

depth, but varied with the offshore H_s and reached a maximum value of 0.51 m on yearday 293.

The angle of incidence of the waves was generally close to the shore normal and varied between -15 and +35 degrees, where a positive angle corresponds to a (north)westerly angle of incidence, while a negative angle corresponds to a (north)easterly angle (Fig.4.4d). The wave angle of incidence based on all three ADVs was generally within several degrees of each other, which corresponds to the compass accuracy.

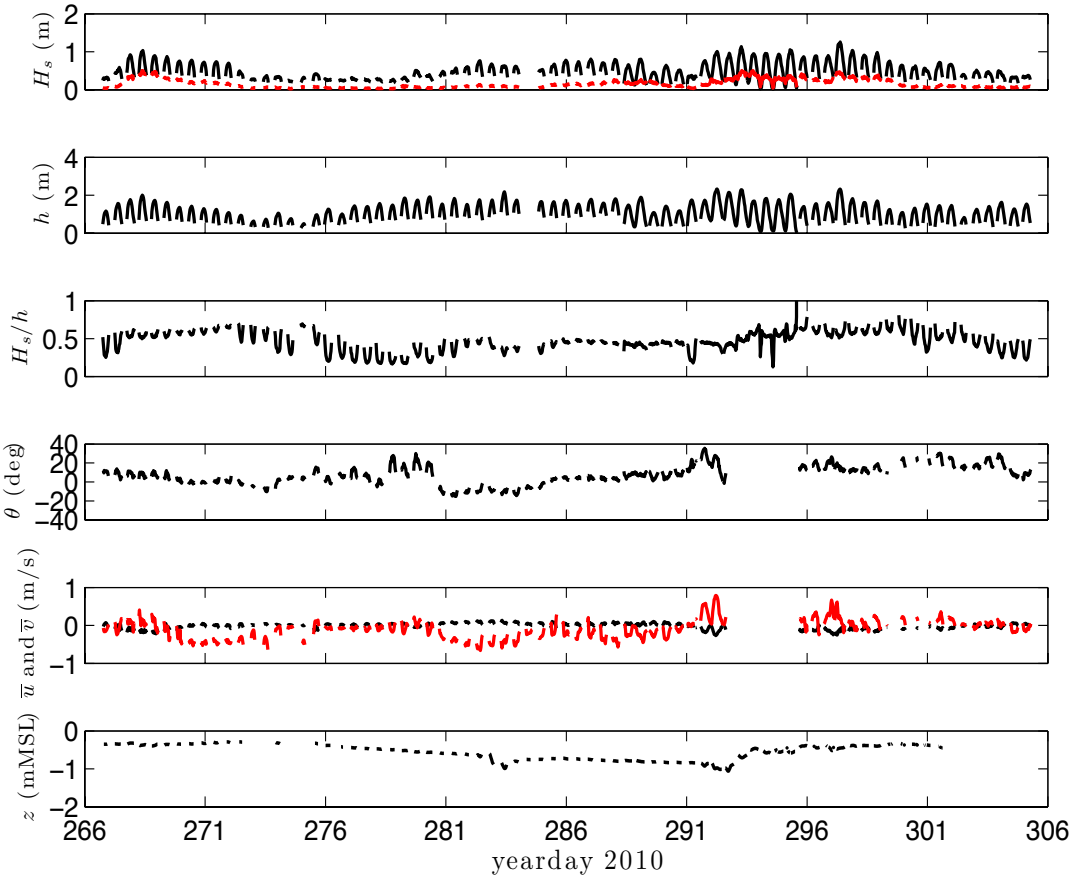

Figure 4.4 Local (a) significant wave height H_s of the swell (black line, 0.04-1 Hz) and infragravity (red line, 0.004-0.04Hz) band, (b) water depth h, (c) relative wave height H_s to h, (d) angle of incidence with respect to the shore normal, (e) mean cross-shore u and alongshore v velocity, (f) bed elevation z with respect to chart datum.

The time-averaged currents (cross- and alongshore, per burst) are shown in Fig.4.4e. The cross-shore currents u are generally very small and only show a negative value during the high energetic conditions around yearday 268/269 and 297/298. The maximum positive value (onshore-directed) of u is 0.14 m/s and the maximum negative value (offshore-directed) is 0.26 m/s. The alongshore currents v are larger than the

cross-shore currents and vary more during the field experiment. During the low-energetic conditions the alongshore current is generally negative (to the west), while during high-energetic conditions the alongshore current is generally positive (to the east). This corresponds to the angle of incidence of the sea-swell waves during these periods. The maximum positive value of v is 0.79 m/s, while the maximum negative value of v is 0.66 m/s. So the maximum towards the east is larger than towards the west, which corresponds to the higher energetic conditions and larger waves that will induce larger alongshore currents. The highest values for both cross- and alongshore currents are found during high tide. The mean vertical velocities were generally small, and had larger negative (downward) and positive (upward) values. The maximum values of the vertical component for all three ADVs were around 0.01 m/s upward and -0.12 m/s downward.

At the start of the field experiment, the instrumented rig was positioned just shoreward of an intertidal trough. From yearday 266 to 276 the bed level at the rig remained approximately constant (Fig.4.4f). After this constant period, the bed level gradually decreased during 7 days from -0.38 to -0.62 m below MSL. The trough that moved onshore caused the gradual decrease of the bed level. This was followed by a sudden decrease in bed level on yearday 283 and 284, when the bed level decreased during two high tides from -0.62 m to -0.99 m. A localized feature caused this sudden fall in bed level, because a large pit developed at the rig. On yearday 284 this pit closed up again, after which the bed level remained approximately constant at -0.75 m until yearday 291, when the trough in which the rig was standing deepened. This trough then moved offshore, which caused the bed level at the rig to increase again from -0.95 to -0.5 m within three high tides. Due to this quite sudden increase in bed level, combined with the high energetic conditions and high water levels, the instruments got buried and could not be reached for several days and no data was collected (Fig.4.4d and 4.4e). During the entire field experiment, also a ripple scanner was deployed on the instrumented rig. This ripple scanner showed almost no ripples at all during the six weeks of the field experiment, suggesting that the ripples that were sometimes found during low water were formed during the swash when the ripple scanner was not submerged.

4.4 Data analysis

4.4.1 Turbulent kinetic energy

In the nearshore, the velocity (u) can be decomposed into mean, wave-induced and turbulent components as follows:

$$u = \bar{u} + \tilde{u} + u', \qquad (28)$$

where an overbar denotes the time-averaged (mean) velocity, a tilde denotes wave-induced velocities and a prime denotes turbulent velocities. The time-averaged turbulent kinetic energy per unit mass ($\langle k' \rangle$) is defined as

$$\langle k' \rangle = 0.5(\langle u'^2 \rangle + \langle v'^2 \rangle + \langle w'^2 \rangle), \qquad (29)$$

where u, v and w are the cross-shore, alongshore and vertical velocities respectively (Scott et al. 2005). It is difficult to separate the wave-induced and turbulent components in random waves and there are several methods for this, so that the turbulent kinetic energy can be found. For random waves, two separation methods can be applied; the high-pass filtering method and the differencing method, these will be discussed below.

The high-pass filtering method can be used when waves are not repeatable. This method separates the wave-induced and turbulent components of velocity by specifying a cut-off frequency separating the wave and turbulent frequencies and then applying the standard filtering techniques to isolate the turbulent component. It can be difficult to choose an appropriate cut-off frequency and possibly it is impossible to find one single cut-off frequency that separates these scales. As opposed to the ensemble averaging method, often used for regular laboratory waves, the filtering method may neglect the large-scale vortices produced by breaking that are of a lower frequency than the organised wave motion, depending on the chosen cut-off frequency. Probably for this reason, the turbulence estimates obtained from the high-pass filtering method are often smaller than those from the ensemble averaging method for regular waves (Scott et al. 2005).

The differencing method can be applied to random waves, using the difference between the measured velocities from two closely spaced sensors to estimate the turbulent velocities. The turbulent velocities are computed based on the differencing and filtering method proposed by Feddersen and Williams (2007). In this method, the linear filtering is applied to all three directions (u, v and w) followed by the Trowbridge (1998) differencing strategy. The method requires input matrices (u, v and w) from two

positions that are demeaned. The velocity at position 2 is transformed to position 1 and then differenced in u, v or w, as follows:

$$\widehat{W}_1 = F(W_2) = \tilde{w}_1 + \varepsilon_w \Delta\tilde{w} + \tilde{n}_w + \delta_w w'_2, \quad (30)$$

where $\tilde{w}_1$ is the wave component of the velocity at sensor 1, $\Delta\tilde{w}$ is the difference between the wave component of the velocity at sensor 1 and 2, and w'_2 is the turbulent component of the velocity at sensor 2. Furthermore, ε_w represents the reduction in wave bias (wave velocity magnitude variations or phase shifts can lead to large differenced wave velocities (i.e. $\Delta\tilde{w}$). To account for this, ε_w ($|\varepsilon_w| < 1$) is used to reduce the wave bias), and $\tilde{n}_w$ is an unknown fraction of $\theta_2\tilde{u}_2$that is passed by the filter and is considered noise. In practice, the instrument coordinate systems are slightly rotated relative to the true coordinate system. The instrument coordinate system is assumed rotated in the 2D x,z plane by a small angle θ_i. Filtering of the turbulent velocities is assumed to result in small δ_w, resulting in differenced velocity $\Delta\widehat{W}_{12}$ (neglecting the small unknown $\tilde{n}_w$).

$$\Delta\widehat{W}_{12} = W_1 - \widehat{W}_1 = -\varepsilon_w \Delta\tilde{w} - \theta_1\tilde{u}_1 + w'_1 - \delta_w w'_2 - \theta_1 u'_1, \quad (31)$$

where $-\varepsilon_w \Delta\tilde{w} - \theta_1\tilde{u}_1$ represents the wave component and $w'_1 - \delta_w w'_2 - \theta_1 u'_1$ is the turbulent component. Assuming that all turbulent velocity components are more or less of the same order of magnitude, this means that the terms $\delta_w w'_2$ and $\theta_1 u'_1$ are much smaller than w'_1 (the turbulent velocity component at sensor 1). This gives the filtered and differenced velocities at position 1, here shown for the vertical component w, but similarly applicable to the cross-shore and alongshore components u and v (Feddersen & Williams 2007). For this method, the sensors have to be separated such that the turbulent component is uncorrelated between the two sensors, which means that the separation distance between the sensors must be larger than the largest eddy produced by wave breaking, but not too large, as the wave signals have to agree.

Both methods were used to see which method gives the best results.

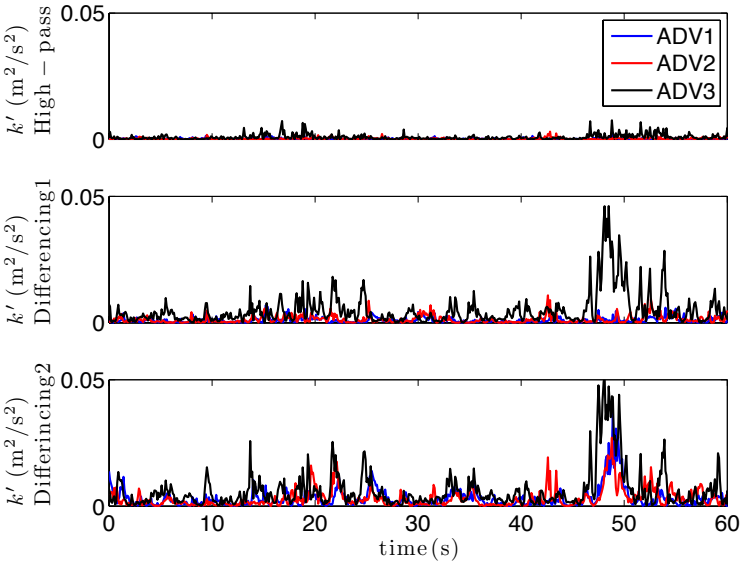

Figure 4.5 Time series of 60s of turbulent kinetic energy for (a) high-pass filtering method and (b) and (c) differencing method.

Figure 4.5 shows an example of a time series of the turbulent kinetic energy for the high-pass filtering method (upper graph), and the two differencing methods (lower two graphs). The differencing method can be calculated in two different ways, as it uses the difference between two ADVs, so for each ADV the difference with two others can be calculated, which gives two different results. In figure 4.5, the black line represents the upper ADV (ADV3), the red line is the middle ADV (ADV2) and the blue line is the lower ADV (ADV1). For ADV3, the two differencing methods give approximately the same results, while for ADV1 and 2 the difference is quite large. In the middle graph (1(2) (the turbulence calculated for ADV1 by using the difference with ADV2), 2(1) and 3(2)), the turbulent kinetic energy at ADV1 and 2 is much smaller than in the lower graph (1(3), 2(3) and 3(1)). The high-pass filtering method gives much smaller results for all three positions and also shows a different trend. The peaks in turbulent kinetic energy that are visible in the lower two graphs are not very well represented in the upper graph. The differences between the methods are also shown in figure 4.6. This shows the time-averaged vertical profile of the turbulent kinetic energy. The high-pass filtering method is clearly smaller than the differencing method and also shows less difference in turbulent kinetic energy between ADV1, 2 and 3, for both the high-energetic and low-energetic conditions (Fig.4.6a and 4.6b respectively).

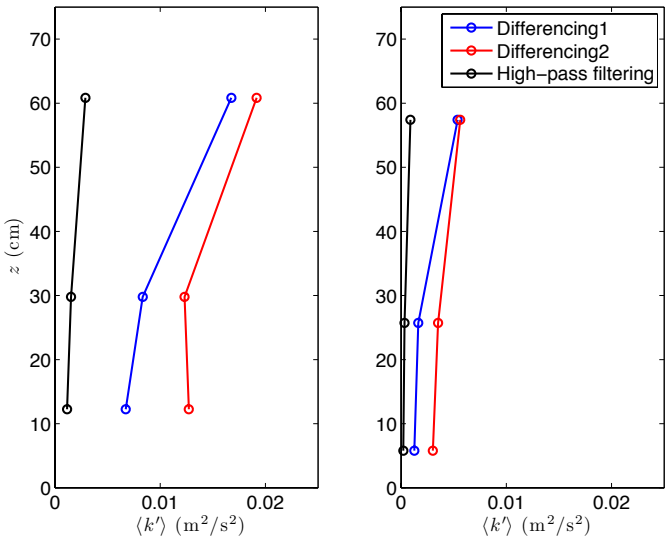

Figure 4.6 Time-averaged vertical profile of turbulent kinetic energy for high-pass filtering method (black line) and differencing methods (red and blue line), for 2 different bursts, (a) high energetic conditions and (b) low energetic conditions.

The fact that the high-pass filtering methods gives smaller k values, is consistent with the expectation that this method will neglect large-scale vortices produced by breaking that are of a lower frequency than the cutoff frequency. The differencing method on the other hand may identify large 'clouds' of turbulence as wave motion. The differencing method compares the signals of two ADVs. The wave motion is assumed to be the same at both ADVs and thus the difference between the two signals is the turbulence. This means that when two ADVs are placed quite close to each other, a large turbulence cloud may be seen as wave motion and thus neglected. Therefore it seems best to use the ADVs that are farthest separated from each other and thus have the least risk of identifying turbulence as wave motion. This means that the lower graph of figure 4.5 represents the method that will be used for all the subsequent analyses.

4.4.2 Dissipation

Dissipation ε can be estimated by using the observed velocity (high) frequency spectrum together with a model for the effect of waves on the turbulent wavenumber spectrum (Feddersen et al. 2007). Velocity spectra [$S_{uu}(\omega)$, $S_{vv}(\omega)$ and $S_{ww}(\omega)$] (where ω is the radian frequency) are calculated at each ADV per burst. The same model is used as Trowbridge & Elgar (2001) used. The turbulence is assumed nearly homogeneous and

isotropic with a Kolmogorov spectrum. The following relation between the velocity spectra and the dissipation rate can then be found.

$$S_{lm}(\omega) = \frac{\alpha\varepsilon^{2/3}}{2(2\pi)^{3/2}} M_{lm}(\omega) \ , \qquad (32)$$

with α = 1.5 is the empirical Kolmogorov constant, ε is the turbulent dissipation, $S_{lm}(\omega)$ is the observed velocity spectrum and where $M_{lm}(\omega)$ is (with mean vertical velocity = 0)

$$M_{lm}(\omega) = \int_{-\infty}^{\infty} \int_{-\infty}^{\infty} \int_{-\infty}^{\infty} \frac{k^{-11/3}(\delta_{lm} - \frac{k_l k_m}{k^2})}{\sqrt{\sigma_i^2 k_i^2}} \times exp\left[-\frac{(k_1\bar{u}_1 + k_2\bar{u}_2 - \omega)^2}{2\sigma_i^2 k_i^2}\right] dk_1 dk_2 dk_3, \quad (33)$$

where k_i is the wave number vector component, σ_i^2 is the variance of the wave velocities and $\bar{u}_i$ is the mean velocity, and i = 1,2,3 for the different components of the velocity. To estimate ε from the observed spectra $S_{lm}(\omega)$, the value of M_{lm} is needed. The observed mean velocity $\bar{u}_i$ and the observed variance of the wave velocities σ_i^2, are used to numerically solve the integral (33). The turbulent dissipation can then be calculated at various radian frequencies (ω) with (Feddersen et al. 2007)

$$\varepsilon(\omega) = \left[\frac{S_{lm}(\omega)2(2\pi)^{3/2}}{\alpha M_{lm}(\omega)}\right]^{3/2}, \qquad (34)$$

Gerbi et al. (2009) found that in the presence of multidirectional waves (as is the case in the field), simpler numerical integration than that of Feddersen et al. (2007) is possible, by writing the equations in terms of bounded integrals and a Gaussian.

$$J_{lm} = M_{lm}\frac{\omega^{5/3}}{2(2\pi)^{3/2}}$$

$$= \frac{1}{2(2\pi)^{3/2}}\frac{1}{\sigma_1\sigma_2\sigma_3}\int_0^{\pi} d\theta \int_0^{2\pi} d\phi G^{-11/3} sin\theta P_{lm} \int_0^{\infty} dR R^{2/3} exp\left[-\frac{(R_0 - R)^2}{2}\right], \quad (35)$$

where θ is between 0 and π, ϕ is between 0 and 2π, G and P are a function of θ and ϕ, and R = 1/r (r = interval between 0 and ∞).

The relation between the observed velocity spectra and the dissipation rate is then:

$$S_{lm}(\omega) = \frac{\alpha\varepsilon^{2/3}}{\omega^{5/3}} J_{lm}(\omega), \qquad (36)$$

which can be rewritten to:

$$\varepsilon(\omega) = \left[\frac{S_{lm}(\omega)2(2\pi)^{3/2}}{\alpha M_{lm}(\omega)}\right]^{3/2}, \qquad (37)$$

So, because the ω is outside the triple-integrals in the Gerbi et al. method, this approach is computationally more efficient, although it gives the same results as the Feddersen et

al. method. Because of this computational advantage, the method of Gerbi et al. (2009) was used to calculate the dissipation.

4.4.3 Quality control turbulence kinetic energy and dissipation

To check the quality of the computed time series of turbulent kinetic energy and dissipation, two quality checks, based upon properties of the turbulent inertial subrange, are used to reject bad data runs. The first test checks that the vertical velocity spectrum's power law exponent is near -5/3 (an uncertainty in the slope taken into account). An example of such a spectrum is shown in figure 4.7. For the turbulence frequencies a line with a slope of -5/3 is plotted (the dotted line) and this shows that the slope of this spectrum for the turbulence frequencies is indeed approximately -5/3. The slope check was done per ADV for each direction (u, v and w). It was then assumed that when at least one of the 3 directions had a slope that was conform the requirements, the quality of the burst was sufficient and it was not rejected.

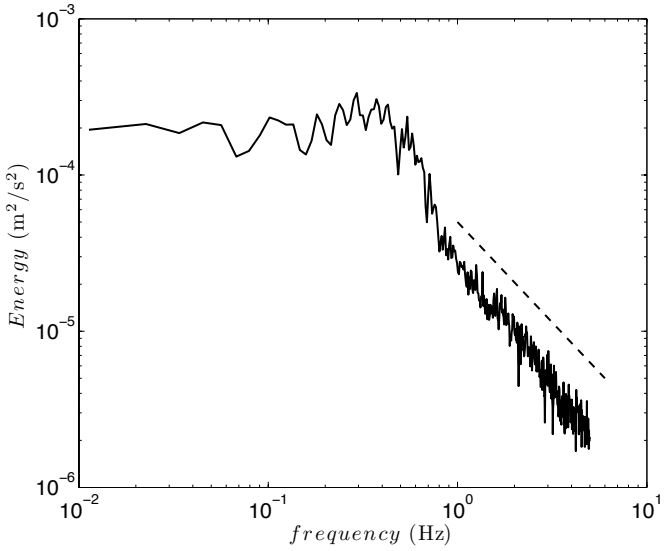

Figure 4.7 Energy spectrum for the vertical (w) velocities, the dotted line represents a -5/3 slope.

The second test checks that the ratio R of horizontal and vertical velocity spectra is near one, where R is:

$$R = \frac{(12/21)\,\langle f^{5/3}(P_{uu}(f) + P_{vv}(f) - noise)\rangle}{\langle f^{5/3} P_{ww}(f)\rangle}, \qquad (38)$$

The ratio R has to be between 0.5 and 2 to pass the quality check test (Feddersen 2010). These quality checks were then used to reject certain bursts, as the quality checks were done per burst. For each ADV the quality check was done separately. For each ADV each

burst was tested whether it was conform the set ratio R and otherwise the entire burst was rejected from further analysis. The ratios R per ADV are plotted against time for the entire field campaign in figure 4.8. The horizontal (dotted) line indicate the boundary values of R above and below which a burst is rejected. Clearly, most bursts are rejected at the lowest ADV, and the least rejected bursts are found at the ADV3 (the upper one). For this ADV, almost all bursts passed this quality check. This suggests that the lower ADVs were possibly sometimes located too close to the bed, which caused inconsistent data due to the presence of the bed, or high sediment concentrations. Another possibility is that close to the bed the -5/3 is not valid anymore, and thus the test cannot be applied close to the bed. Data runs that did not pass both quality check tests were considered inconsistent with a turbulent inertial subrange and their turbulent kinetic energy and dissipation estimates were rejected.

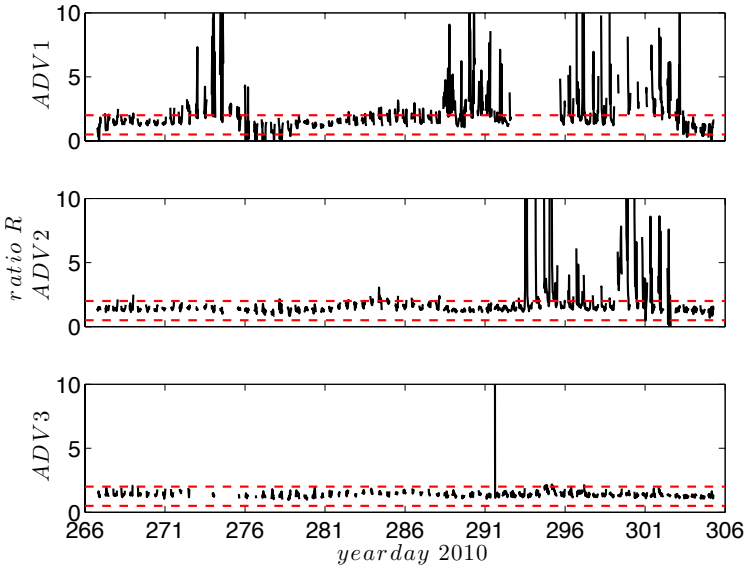

Figure 4.8 The ratio R against time for the entire field experiment for (a) ADV1, (b) ADV2, and (c) ADV3. The red dotted lines indicate the upper and lower boundary of R for the quality check.

These quality checks were applied to both the turbulent kinetic energy and turbulent dissipation time series. For the turbulent kinetic energy, about 62% of all bursts passed the quality checks, with the highest percentage of good bursts for the upper ADV and the lowest percentage for the lower ADV, as can be seen in table 4.1. For the turbulent dissipation the total percentage of passed bursts is about 60%, and a similar difference between the lower and upper ADV can be seen (table 4.2). So about 60% of all bursts passed both quality checks. Table 4.3 shows how many bursts passed the R test, which is considerably higher (80%), with again the highest values at the upper ADV.

TKE	Total bursts	Good bursts	Percentage
ADV1	652	300	46.01%
ADV2	788	454	57.61%
ADV3	652	547	83.90%
Total	2092	1301	62.19%

Table 4.1 The amount of bursts that passed both the quality checks for turbulent kinetic energy.

Dissipation	Total bursts	Good bursts	Percentage
ADV1	974	413	42.4%
ADV2	999	569	56.96%
ADV3	789	668	84.66%
Total	2762	1650	59.74%

Table 4.2 The amount of bursts that passed both the quality checks for turbulent dissipation.

Dissipation due to R	Total bursts	Good bursts	Percentage
ADV1	974	611	62.73%
ADV2	999	848	84.88%
ADV3	789	776	98.35%
Total	2762	2235	80.92%

Table 4.3 The amount of bursts that passed the ratio R quality check for turbulent dissipation.

5. Turbulence

5.1 Turbulent kinetic energy

This chapter will discuss the results of the data analysis for the turbulent kinetic energy, and will thus specifically investigate the research questions regarding turbulent kinetic energy. It will be investigated whether turbulence that was generated at the surface and is spreading downward to the bed. Furthermore a question that will be answered is whether turbulent kinetic energy increases over the vertical profile during more intense breaking conditions, more specifically under larger relative wave heights. First of all, the general results of turbulent kinetic energy will be discussed. Then, the vertical profile will be discussed in more detail, comparing it to relative wave height and total breaker dissipation. The turbulent kinetic energy will then be related to position in the surf zone, using a model. Finally, results of some methodological issues regarding turbulent kinetic energy will be discussed.

5.1.1 General results

The turbulent kinetic energy k was calculated for the entire 6-week period. For each burst, an instantaneous 10 Hz time series of turbulent kinetic energy k was computed and per burst also a (time-averaged) turbulent kinetic energy rate $\overline{k}$ was calculated. Figure 5.1 shows the time series of the turbulent kinetic energy rate $\overline{k}$ over the entire field experiment. This graph includes only the bursts that were not rejected by the quality checks. The turbulent kinetic energy $\overline{k}$ is clearly largest during the higher energetic periods (see Fig. 4.3) with values up to 0.035 m^2/s^2 and smaller during the calm conditions. Furthermore, the majority of the rejected bursts seem to be during the low energetic conditions, since during this period the number of gaps in the graph is large. This can be due to several things. First of all, during lower energetic conditions, fewer bubbles are in the water, which leads to lower correlations and accuracy of the ADVs, so during higher energetic conditions, the correlations are higher and the bursts will not be rejected. Secondly, during low-energetic conditions the wave set-up is less, which leads to a relatively lower water level that is even lower because of the neap tidal conditions. Due to this lower water level the ADVs are submerged during a shorter period of time and more bursts are rejected. Finally, if $\overline{k}$ is smaller, the value is closer to the noise level of the instrument.

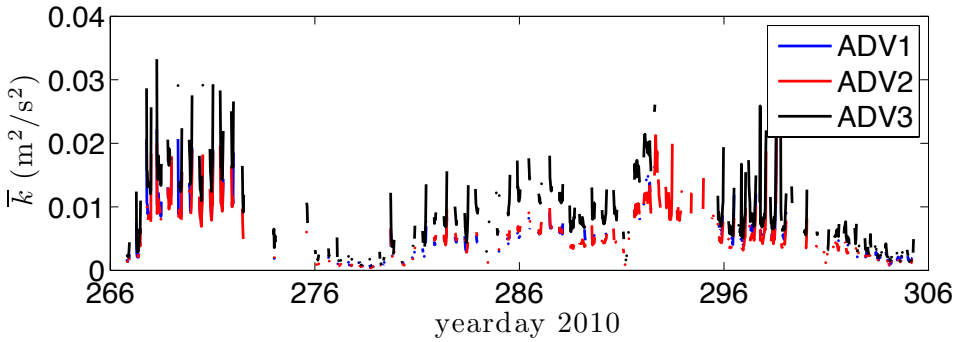

Figure 5.1 Turbulent kinetic energy k for the 6-week field experiment for ADV1 (blue line), ADV2 (red line) and ADV3 (black line).

In figure 5.2 an example of the instantaneous turbulent kinetic energy k as a function of time (for 60 sec) is shown. The black, red and blue line represent the three ADVs, where the black line is of the upper ADV (ADV3), the blue line is of the lower one (ADV1) and the red line is of the middle one (ADV2). The turbulent kinetic energy at ADV3 is generally larger than that of the lower two ADVs, but they follow the same pattern with peaks at the same time. The close resemblance of turbulent velocity fluctuations at different elevations indicate that turbulence generated at the surface is spreading downward towards the bed.

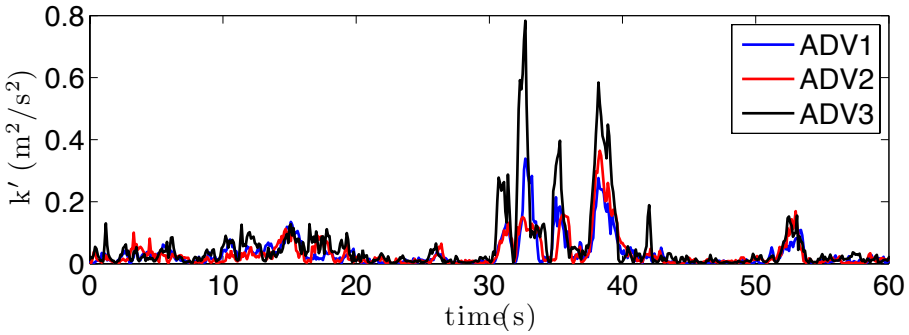

Figure 5.2 Time series of 60 sec of the turbulent kinetic energy k for ADV1 (blue line), ADV2 (red line) and ADV3 (black line).

5.1.2 Vertical profile

For each burst three vertical positions of velocity measurements were available. To investigate the vertical profile characteristics for different conditions, several of these profiles were plotted. In figure 5.3 the time-averaged vertical profile of turbulent kinetic energy (per burst) for one high tide is shown. As was already seen in the time series, the turbulent kinetic energy is largest in the upper part of the water column, and decreases downward. The turbulent kinetic energy at the lower two ADVs is almost equal, but at

ADV1 the turbulent kinetic energy is slightly larger in the example shown here. ADV2 could give smaller values due to the smaller distance between the ADVs for calculating turbulence with the differencing method, which leads to more turbulence bias. This suggests that not only the surface-generated turbulence contributes to the turbulent kinetic energy at the lower ADV, but also the bottom boundary layer turbulence has an (small) influence. During the high tide, the magnitude of the turbulent kinetic energy changes, but the shape of the vertical profile remains the same. This change in magnitude could suggest that the higher turbulent kinetic energy occurs during higher energetic conditions. However, the range of relative wave height Hs/h (a measure for breaking) during this high tide is quite small (0.58-0.63). A trend that is more striking is the fact that the highest TKE values occur during rising and falling tide, while the lowest values occur at high tide. So the turbulent kinetic energy seems to depend on either water depth, or relative position in the surf zone, as the highest values of turbulent kinetic energy occur during the lower water depths and the position closest to the shoreline.

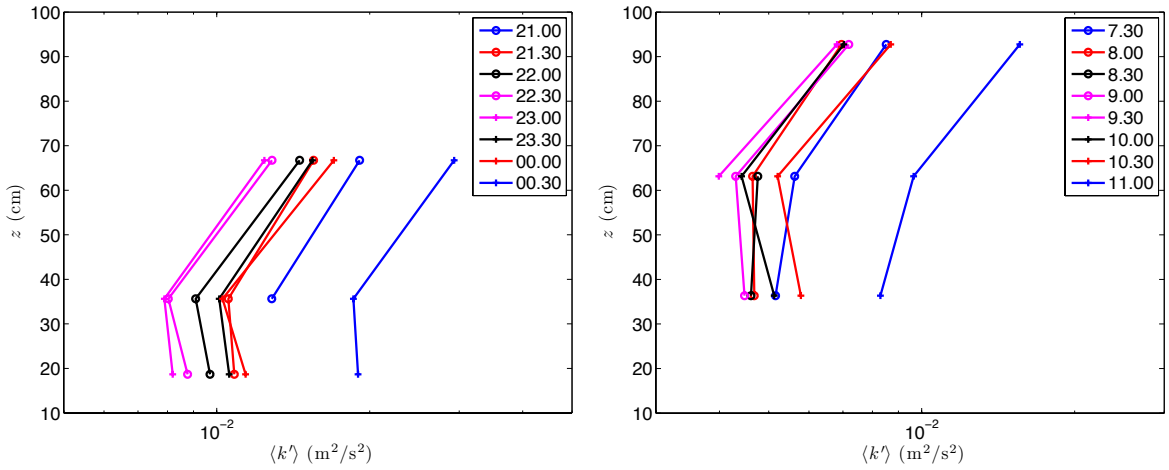

Figure 5.3 Time-averaged vertical profiles per burst of the turbulent kinetic energy k for (a) a high energetic high tide and (b) a low energetic high tide.

Figure 5.3b shows a similar figure of the time-averaged vertical profile of the turbulent kinetic energy. However, this is a lower energetic high tide (with relative wave heights varying from 0.44 – 0.48). The turbulent kinetic energy is smaller than during the high energetic tide. Again, the highest values of k are found during rising and falling tide, while the lowest values occur during high tide. This again suggests that k depends on either water depth or position in the surf zone during both high- and low-energetic conditions. Although the shape of the vertical profile is quite similar to that of Figure

5.3a the difference between the highest ADV3 and the lower 2 ADVs is larger, which suggests that vertical mixing is less strong during lower energetic conditions and that the turbulent kinetic energy is more confined to the upper part of the water column. This shows that turbulent kinetic energy is dependent on offshore energy conditions on the one hand, and on the other hand it depends on the tide, which is an effect that is superimposed on the dependency on energy conditions.

The variation in the vertical structure of turbulent kinetic energy was then quantified by decomposing the turbulent kinetic energy estimates into an EOF for each ADV (Figure 5.4). The estimates were taken into account for the EOF if at least two of the ADVs were working and that data passed the quality checks. The EOF decreases from the top ADV to the middle one and then increases again towards the bottom one, which is similar to what was seen in figure 5.3. The EOF decomposition explains 96% of the turbulent kinetic energy variance. So the temporal variations in turbulent kinetic energy are very coherent in the water column. The smaller value at ADV2 could be due to computational differences (turbulence bias), or because of bed-generated turbulence influence at ADV1.

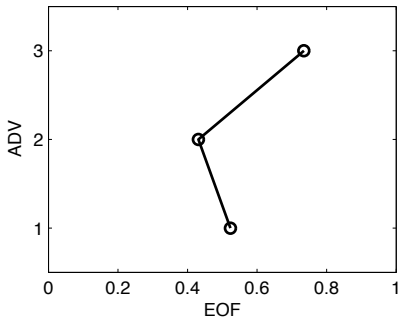

Figure 5.4 Vertical structure of the EOF for turbulent kinetic energy <k'>. This EOF explains 96% of the total variance in <k'>.

Figure 5.5 shows the EOF coefficients divided in negative and positive coefficients in figure 5.5a and 5.5b respectively. Furthermore they are divided for ADV1, 2 and 3. This shows that the EOF coefficients at ADV1 are largely negative, while those at ADV3 are mostly positive. The EOF coefficients at ADV2 are mostly around 0, but both negative and positive. The EOF coefficients were plotted against relative wave height Hs/h, to investigate the relation with wave breaking. This division in sign of the EOF coefficients at ADV1 and 3 indicates a double source of turbulent kinetic energy, both at the bed and at the surface. So at the lower ADV, mostly bed-generated turbulence is important, shown by the negative sign of the coefficients, while at the upper ADV, surface generated turbulence is most important, indicated by the positive sign. At the middle ADV, the importance of bed and surface generated turbulence alternates, which can be seen from

the coefficients that are sometimes positive and sometimes negative at ADV2. Both the positive and negative EOF coefficients increase with relative wave height, indicating a dependency on wave breaking. This is particularly interesting for the negative coefficients, because this indicates that bed-generated turbulence also increases with relative wave height.

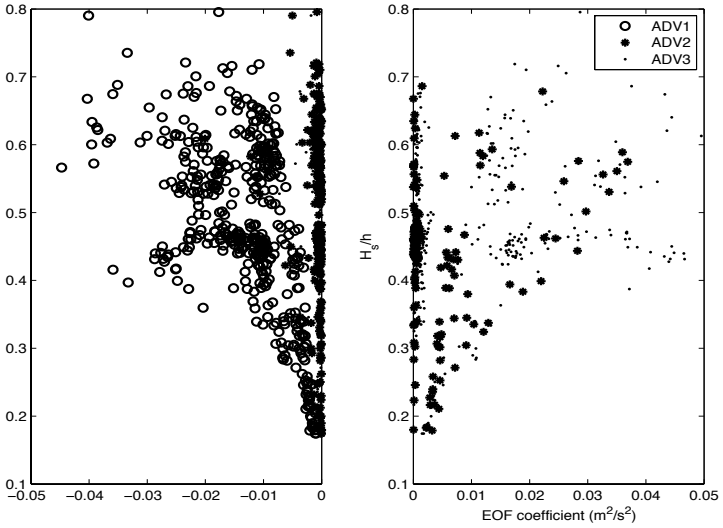

Figure 5.5 (a) negative, and (b) positive coefficients of the first EOF for turbulent kinetic energy.

The time-averaged turbulent kinetic energy per burst was then divided into groups of water depths and relative wave heights per ADV (for each burst when all ADVs are measuring). In figure 5.6 these groups of turbulent kinetic energy are plotted against height above the bed. The left figure shows the turbulent kinetic energy in the largest water depth (h>2m), while the figure on the right shows the turbulent kinetic energy in the smallest water depth (h<0.5m). The different colours in each subplot indicate different groups of relative wave height, from Hs/h < 0.38 (no breaking, blue line) up till Hs/h > 0.58 (all waves broken, magenta line). The horizontal lines through each point represent the standard deviation of the group of turbulent kinetic energy rates, while the vertical lines through each point represent the standard deviation of the group of elevation above the bed. At the largest water depths (h>2m), the largest turbulent kinetic energy rates are found near the bed and higher up in the water column for Hs/h = 0.38-0.48, while the turbulent kinetic energy rates for Hs/h = 0.48-0.58 are smaller. This suggests that for the first one there is a double source of turbulent kinetic energy, from both the bed and the surface, while for the larger relative wave heights the turbulent kinetic energy is smaller throughout the entire water column. The three middle figures, with water depths varying between 0.5 and 2 m, all show more or less the same trend. The turbulent kinetic energy rates are largest higher up in the water

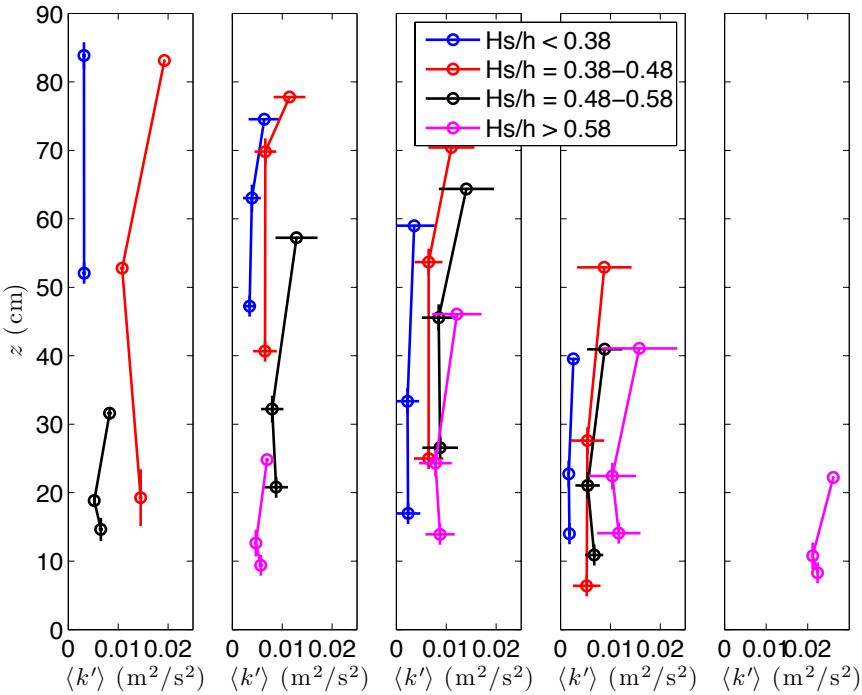

Figure 5.6 Turbulent kinetic energy rates per water depth, with (a) h > 2m, (b) h = 1.5-2m, (c) h = 1-1.5m, (d) h = 0.5-1m, and (e) h < 0.5m; and relative wave height, with Hs/h < 0.38 (blue), Hs/h = 0.38-0.48 (red), Hs/h = 0.48-0.58 (black), and Hs/h > 0.58 (magenta). The horizontal lines indicate the standard deviation of the turbulent kinetic energy rates, the vertical lines indicate the standard deviation of the height of each ADV above the bed.

column and decreasing downward. This suggests that the surface turbulence dominates in this region. Furthermore, the turbulent kinetic energy rates for Hs/h < 0.38 are clearly smallest for all three water depths. These are mostly constant throughout the water column, with a slight trend increasing upward. Possibly the turbulent kinetic energy rates would also increase closer to the bed for this relative water height (suggesting a bottom-generated turbulence source), however, the measurements were mostly done quite high above the bed. In general, the largest increase in turbulent kinetic energy seems to be from Hs/h < 0.38 to Hs/h = 0.38-0.48. This is generally assumed to be the transition from non-breaking to breaking waves, so this increase in turbulence dissipation again suggests that breaking waves are an important surface source of turbulence. From this group of relative wave heights to the next (Hs/h = 0.48-0.58), the turbulent kinetic energy also increases, but the difference is not so big. At the highest relative wave heights (Hs/h > 0.58) the turbulent kinetic energy even decreases, except for h = 0.5-1 m, where it increases slightly. These more or less constant values of turbulent kinetic energy rates from Hs/h = 0.48 onward suggest that when eventually all

the waves are breaking, the intensity of wave breaking is not very important for the turbulent kinetic energy. The decrease of the turbulent kinetic energy rate at Hs/h > 0.58 could indicate a transition to a different type of wave breaking. The plot of the smallest water depths shows an entirely different image. First of all, very little data is available for these small water depths, because these were often rejected by the quality control of the ADV data. Secondly, the data that is available is exclusively for Hs/h > 0.58. The profile of the turbulent kinetic energy rates for this relative wave height shows a more or less constant turbulent kinetic energy throughout the lower 20cm of the water column. The turbulent kinetic energy is larger throughout the water column than the maximum turbulent kinetic energy rates for the larger water depths. This suggests that closer to the shoreline, in the inner surf zone to the swash zone, turbulence generated at the bed is increasingly more important, but also surface-generated turbulence is still important.

The turbulent kinetic energy rate was subdivided in a similar way, but then for different groups of breaker dissipation per water depth (Figure 5.8). The total breaker dissipation was computed over the cross-shore profile, to be able to determine the contribution of turbulent dissipation to total breaker dissipation. The breaker dissipation was calculated by first computing the energy flux at every point in the cross-shore profile, using the time series of the water depth and integrating over the short-wave frequency band. The breaker dissipation could then be computed using the difference in energy flux from one cross-shore position to the next. Figure 5.7 shows the (burst-averaged) total breaker dissipation for the entire campaign, which clearly shows a similar trend as the turbulent kinetic energy, with larger dissipation during the two storm events and lower dissipation during the low energetic period in between.

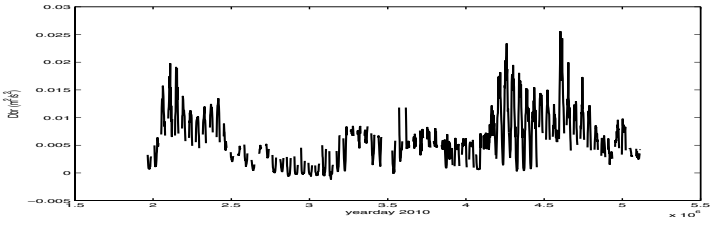

Figure 5.7 Burst-averaged total breaker dissipation for the entire campaign.

An increase in breaker dissipation indicates an increase in wave breaking. When the breaker dissipation is smaller than 0, this means that the energy flux does not decrease, but increase. Again, the horizontal lines through the points indicate the standard

deviation of the turbulent kinetic energy of that group, and the vertical lines indicate the standard deviation of the elevation above the bed. Generally, for all water depths and breaker dissipation groups, the turbulent kinetic energy is largest higher up in the water column and decreasing downward. However, for the largest water depth (h>2m) the turbulent kinetic energy seems to have a minimum in the middle of the water column and then increases both towards the surface and the bed. This suggests that there is also a source of turbulence near the bed. As expected, the turbulent kinetic energy is very small when the breaker dissipation is smaller than 0. In this case, the turbulent kinetic energy is close to 0 throughout the water column. The turbulent kinetic energy then increases with breaker dissipation, from Dbr = 0-0.005 to Dbr = 0.005-0.0125 (for all water depths), but then does not increase to the larger breaker dissipations of Dbr > 0.0125, as was also seen for the comparison with relative wave height. This suggests that there is maximum breaker dissipation up till where the turbulent kinetic energy increases and then it levels out. For the largest water depth, there is even a decrease in turbulent kinetic energy from Dbr = 0.005-0.0125 to Dbr > 0.0125. For the smallest water depths, no correct data was found for all ADVs at the same time.

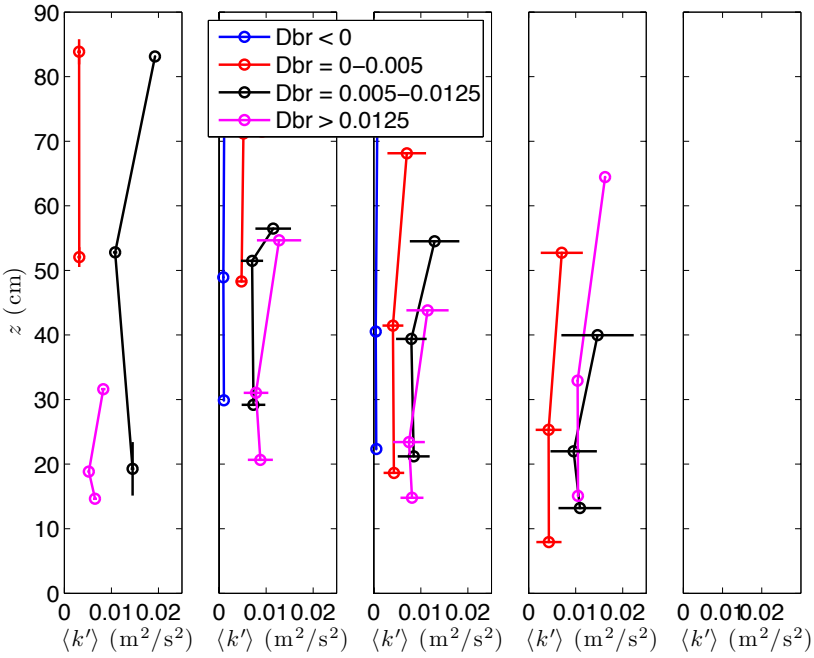

Figure 5.8 Turbulent kinetic energy rates per water depth, with (a) h > 2m, (b) h = 1.5-2m, (c) h = 1-1.5m, (d) h = 0.5-1m, and (e) h < 0.5m; and total breaker dissipation, with Dbr < 0 (blue), Dbr = 0-0.005 (red), Dbr = 0.005-0.0125 (black), and Dbr > 0.0125 (magenta). The horizontal lines indicate the standard deviation of the turbulent kinetic energy rates, the vertical lines indicate the standard deviation of the elevation of each ADV above the bed.

5.1.3 Position in surf zone and characteristics

5.1.3.1 Battjes-Janssen model

As the measurements were only done at one position, no cross-shore variation of turbulent kinetic energy is available. To look at the dependence of turbulent kinetic energy on the relative position in the surf zone, a model was used to determine the position of the instrumented rig relative to the shoreline (per burst). The model that was used was of Battjes & Janssen (1979). This model uses offshore wave height and a cross-shore bed profile to predict the propagation of the waves, i.e. where the waves will start breaking. If the start of wave breaking, the position of the shoreline and the position of the instrumented rig are known, the relative position of the rig in the surf zone can be determined. The model of Battjes-Janssen was run four times. First of all for three different methods to calculate the γ breaking factor (see Appendix) and secondly one time with the bed friction factor included, which was excluded in the first three model runs. These four different model runs were done to find the best prediction of the model for the position of the surf zone. To be able to evaluate the model runs, the predicted wave height from the model is compared to the measured wave height. These predicted wave heights and measured wave height are shown in Figure 5.9. Since the model calculates the root-mean-square wave height (H_{rms}), while the wave height from the measurements is the significant wave height (H_s), it was assumed that $H_s = 1.41H_{rms}$.

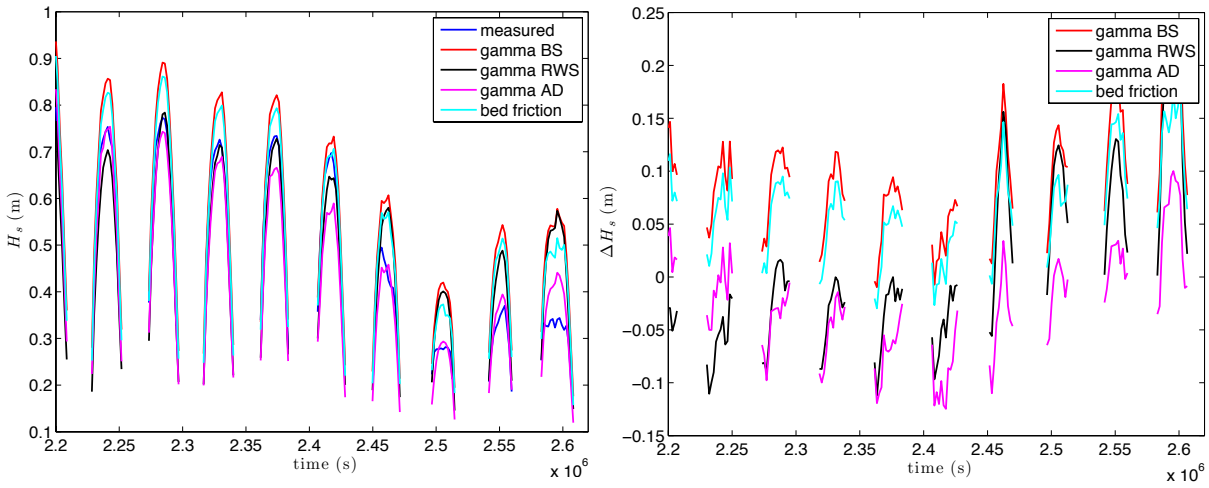

Figure 5.9 (a) predicted and measured wave height at the rig (blue line is measured) and (b) difference between predicted and measured wave height. Both for three different γ methods, Battjes-Stive (BS, red line), Ruessink et al. (RWS, black line) and Apotsos et al. (AD, magenta line), and one model run including bed friction (cyan line).

The wave height at the rig seems to be predicted best by the γ method of Ruessink et al. (2003) (RWS). The method of Battjes-Stive (1985) overpredicts the wave height always (even when bed friction is included), while the method of Apotsos et al. (2008) generally underpredicts the wave height. So based on wave height at the rig, the RWS method seems to be the best.

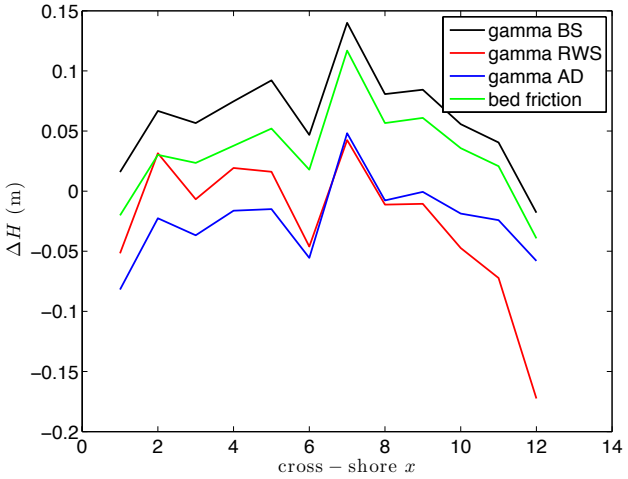

Figure 5.10 Difference between the measured wave height and the predicted wave heights for each cross-shore position, averaged over the entire field campaign. For the BS method (black), the RWS method (red), the AD method (blue) and the BS method with bed friction (green).

However, for the model, not only the wave height at the rig is important, but also the behaviour of the waves towards the shoreline and thus the position of the surf zone. Therefore, also the wave height propagation was investigated. Figure 5.10 shows the cross-shore profile of the difference between modelled wave height and measured wave

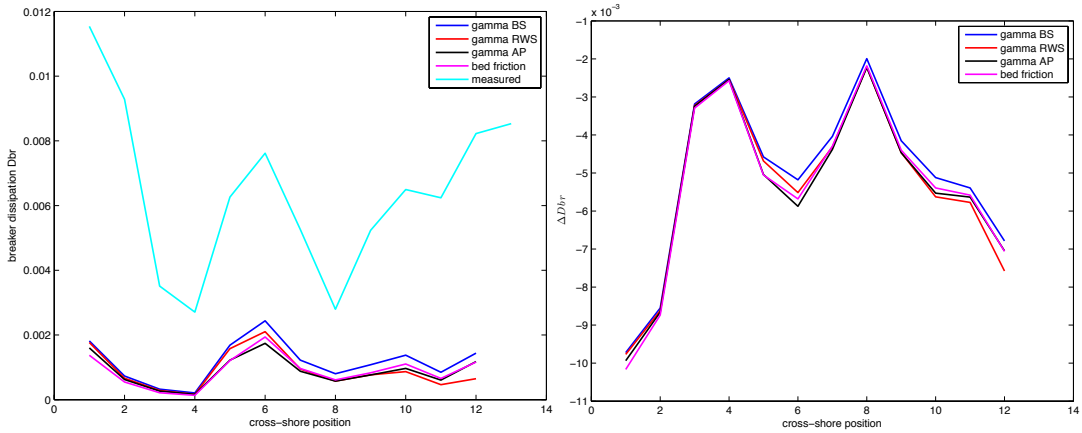

Figure 5.11 (a) Measured breaker dissipation (cyan) and the predicted breaker dissipation for each cross-shore position, averaged over the entire field campaign. (b) Difference between predicted and measured breaker dissipation. The BS method (blue), the RWS method (red), the AD method (black) and the BS method with bed friction (magenta).

height, as predicted by the four different model runs. On the x-axis, the cross-shore position is given, where position 1 is the most seaward positioned instrument and position 12 is the most landward positioned instrument. The instrumented rig is located at position 5. The graph shows the time-averaged prediction (over the entire campaign) of the wave height per cross-shore position. As can be seen in this figure as well, the wave height at the rig (position 5) is best predicted by the RWS method, however, the Apotsos et al. (AD) method seems to work better throughout the entire cross-shore profile. While the RWS method shows a large underestimation of the wave height for the positions closest to the shoreline, the underestimation of the AD method is smaller. Both the Battjes-Stive (BS) method and the BS method with bed friction overpredict the wave height almost all the time, so these are clearly not better. Figure 5.11a shows the cross-shore predicted breaker dissipation and the cross-shore measured breaker dissipation, the difference between the measured and predicted breaker dissipation is shown in figure 5.11b. The measured and predicted breaker dissipation clearly show a similar trend, but the model always underestimates the breaker dissipation by a factor 2-6. There is not a large difference between the different model settings, these all give more or less the same results. Figure 5.12 shows the measured and modelled breaker dissipation plot against each other. The black line is the 1:1 relation. For smaller breaker dissipation values the model seems to work better than for higher values.

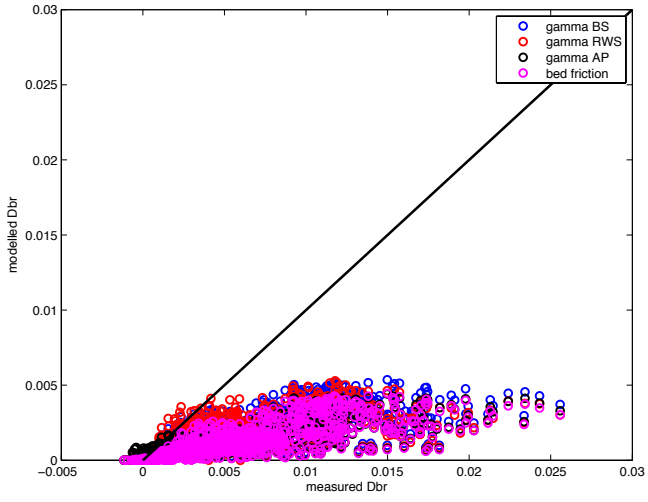

Figure 5.12 Modelled breaker dissipation rate against measured breaker dissipation, for the BS method (blue), the RWS method (red), the AP method (black), and the BS method with bed friction (magenta). The black line is a 1:1 line.

Then the results of the different model runs for the position in the surf zone were investigated. The cross-shore flux was calculated for each instrument position (10 OSSIs and 4 instrument frames). The seaward side of the surfzone was then determined to start where the flux drops below 85% of the flux at the offshore boundary (Thomson et al. 2006). The landward side of the surfzone is where the flux drops to 0. The model

gave an output of 0 at the position of the shoreline and 1 at the transition from breaker zone to shoaling waves. For each burst the position of the rig was calculated. The model results were interpreted as follows: if the value was larger than 1, the waves were assumed to be shoaling, not breaking at the rig; if the value was between 0.5 and 1, the rig was assumed to be positioned in the outer surf zone, with some, but not all, waves breaking; if the value was between 0 and 0.5, the rig was assumed to be in the inner surf zone, with all waves breaking.

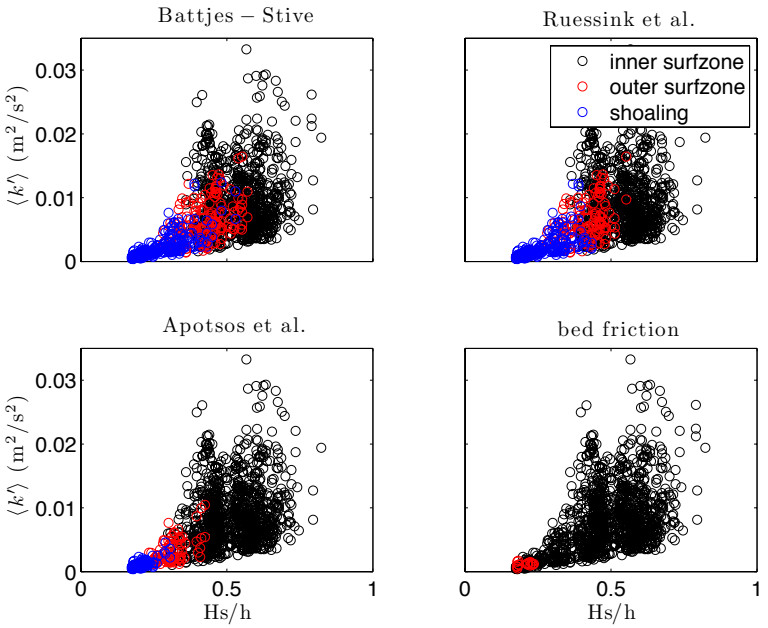

Figure 5.13 Turbulent kinetic energy subdivided in shoaling waves (blue), outer surf zone (red) and inner surf zone (black) against relative wave height for the four different model runs.

The results of the four model runs for the position of the surf zone are shown in figure 5.13. This figure shows the turbulent kinetic energy against the relative wave height subdivided into inner surf zone, outer surf zone and shoaling waves, as it is found from the model. The three model runs for the different γ methods all show a similar trend in the position in the surf zone. For the lower relative wave heights, the waves are found to be shoaling, then with increasing H_s/h this shifts to outer surf zone and then to inner surf zone. However, the model run where bed friction is included gives an entirely different result. According to the results of this model run, the rig was never in the shoaling wave zone, but almost always in the inner surf zone, even when the relative wave height was only about 0.2 (when waves are assumed not to be breaking). This has to do with the method that determines the edge of the surf zone. This method assumes that bed friction can be neglected, but apparently this is not the case. The model run with bed friction is rejected from use in further analysis. The three other model runs show similar results, but the position of the transition from shoaling waves to outer surf

zone and from outer surf zone to inner surf zone differ. The transition from shoaling waves to outer surf zone is at $H_s/h \approx 0.25$ for the AD method, at $H_s/h \approx 0.4$ for both the RWS and BS method. The transition from outer surf zone to inner surf zone is at $H_s/h \approx 0.4$ for the AD method, while it is at $H_s/h \approx 0.5$ for the RWS method and at $H_s/h \approx 0.55$ for the BS method. However, especially the transition from outer to inner surf zone is not very clear. In other experiments, the transition from shoaling waves to outer surf zone and from outer surf zone to inner surf zone was found to be at $H_s/h \approx 0.38$ and $H_s/h \approx 0.48$ respectively (Ruessink 2010). These values are closest to the values found by the γ method of Ruessink et al. (2003).

So therefore, the model run that will be used is the model run with the method of Ruessink et al. (2003). Although the cross-shore prediction of the wave height near the shoreline was not the best one, the cross-shore prediction of the wave height propagation from offshore to several positions shoreward of the rig was very good. Furthermore, the predicted wave height at the rig was most consistent with the measured values (Fig.5.10) and the results for the position of the surf zone were closest to the expected values of the relative wave height Hs/h.

5.1.3.2 Model results

The model results found in the previous paragraph were then investigated further for different characteristics of the turbulent kinetic energy. The turbulent kinetic energy is plotted against the water depth h (Figure 5.14a) and the relative position in the water column z/h (Figure 5.14d). All points are separated into shoaling waves, outer surf zone and inner surf zone. The blue points represent the shoaling waves, the red points the outer surf zone and the black points the inner surf zone. These graphs show that the turbulent kinetic energy does not depend on water depth, while it does increase going from shoaling waves to outer surf zone to inner surf zone. There is some relation visible between turbulent kinetic energy and the relative position in the water column, with a slight increase of turbulent kinetic energy higher up in the water column. The shoaling waves are clearly found in the lower segment of both the turbulent kinetic energy and the relative wave height. In the outer surf zone the turbulent kinetic energy is also rather low, while in the inner surf zone it is substantially larger but also more scattered. Furthermore it can be seen from figure 5.14e is that turbulent kinetic energy is

positively related to the degree of wave breaking. This trend is best visible at the smaller values of the turbulent kinetic energy, as the larger values are more scattered.

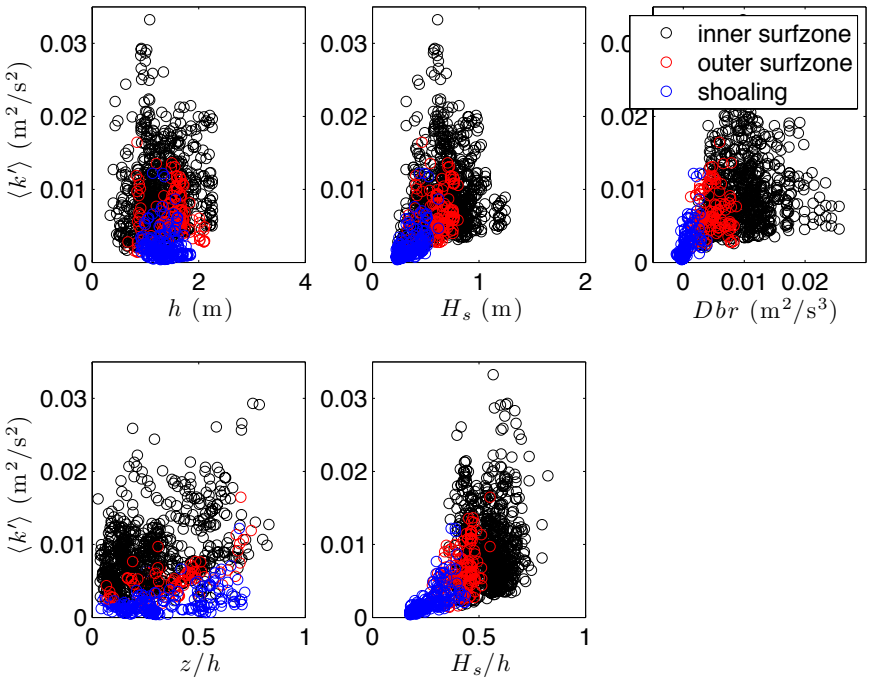

Figure 5.14 Model results for RWS method with turbulent kinetic energy plotted against (a) water depth h, (b) wave height Hs, (c) relative position in the water column z/h, and (d) relative wave height Hs/h.

There also seems to be a weak relation between significant wave height Hs and the turbulent kinetic energy, as the turbulent kinetic energy increases with increasing Hs (Figure 5.14b). So some correlation is visible between turbulent kinetic energy and Hs/h and Hs, but a stronger relation is found between turbulent kinetic energy and the position in the surf zone. The turbulent kinetic energy is positively related to breaker dissipation (Figure 5.14c). The breaker dissipation is also increasing from the outer surfzone into the inner surfzone, consistent with an increase in breaking intensity.

The turbulent kinetic energy rates were then subdivided into groups of relative wave height (Hs/h<0.3, Hs/h=0.3-0.5 and Hs/h>0.5) and plotted against relative position in the water column z/h, in figure 5.15b-d respectively. As was shown earlier, turbulent kinetic energy increases with relative wave height (Figure 5.15a). For the lowest relative wave heights (Figure 5.15b), the turbulent kinetic energy is always low throughout the water column and only increasing slightly towards the surface. For the higher relative heights (Figure 5.15c), when waves are starting to break, the turbulent kinetic energy is clearly larger and increasing higher up in the water column, although there is also a lot of scatter. At the highest relative wave height (Figure 5.15d), when all

waves are breaking, the turbulent kinetic energy is largest and highly increasing towards the surface, indicating a large dependency on wave breaking. This indicates that the turbulent kinetic energy is generally surface-generated.

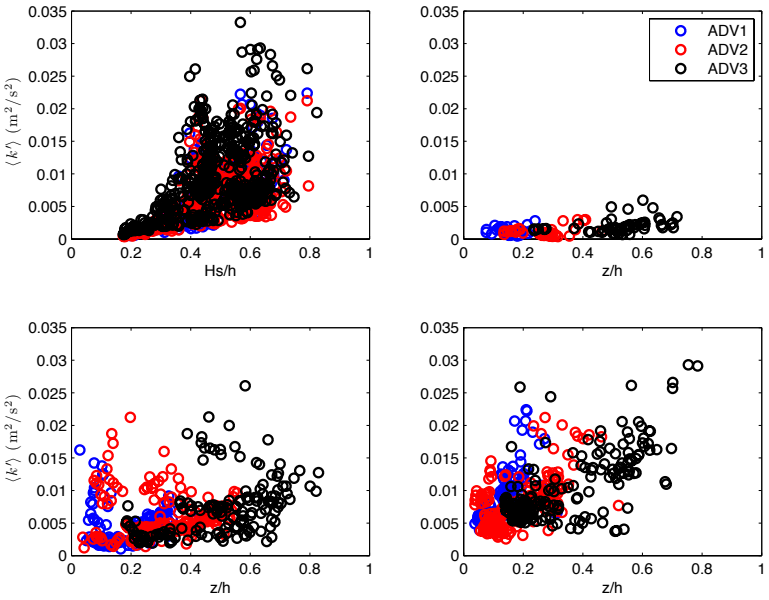

Figure 5.15 (a) Turbulent kinetic energy plotted against relative wave height Hs/h, (b) Turbulent kinetic energy for Hs/h<0.3 against relative position in the water column z/h, (c) Turbulent kinetic energy for 0.3<Hs/h<0.5 against z/h, and (d) Turbulent kinetic energy for Hs/h>0.5 against z/h.

5.1.4 Froude-scaled TKE

The turbulent kinetic energy was then normalized (Froude-scaled) by dividing k by gh and then taking the square-root of the result: $(k'/gh)^{1/2}$. The Froude-scaled turbulent kinetic energy $(k'/gh)^{1/2}$ varies between 0.005 and 0.04, as can be seen in figure 5.16a, with an average value of about 0.02. Figure 5.16a does not show a clear vertical trend, which suggests that vertical turbulence mixing is strong. However, when the graph is limited to the Froude-scaled turbulent kinetic energy in the inner surf zone (Hs/h>0.48), a different image is found, which is shown in figure 5.16b. The Froude-scaled turbulent kinetic energy is now varying mostly between 0.015 and 0.04, so the lower values do not occur during higher energetic conditions. Furthermore, there seems to be a vertical trend, with an increase of Froude-scaled turbulent kinetic energy at higher z/h. This suggests that the turbulent kinetic energy is mostly surface generated. Most laboratory observations of $(k'/gh)^{1/2}$ beneath surf zone bores after spilling breaking are in the range from 0.03 to 0.07. However, Scott et al. (2005) found that turbulence intensities beneath irregular breaking waves are lower than those beneath regular waves with

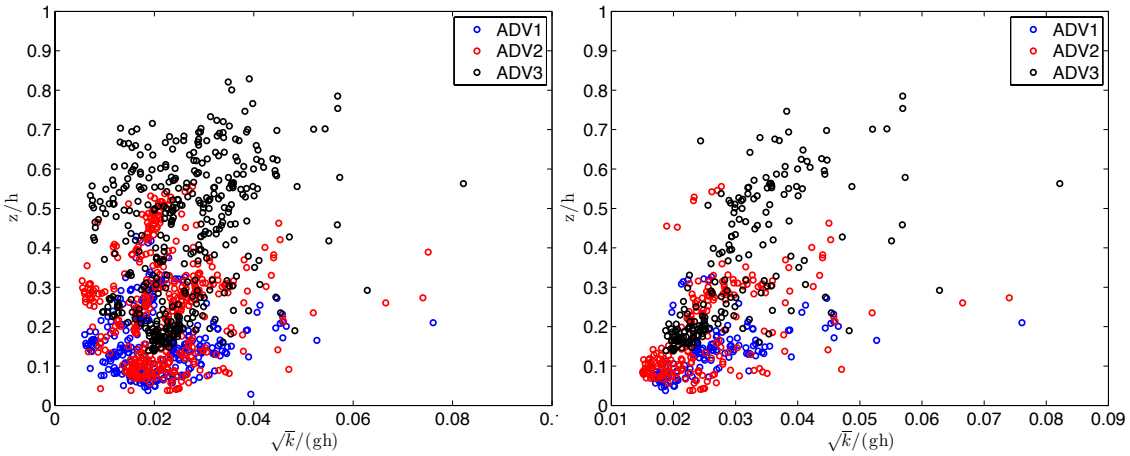

Figure 5.16 Froude-scaled turbulent kinetic energy $(k/gh)^{1/2}$ against relative position in the water column z/h for (a) all conditions, and (b) for Hs/h>0.48.

similar wave height and period, which is confirmed by the values found in this field experiment. This was also found by Mocke (2001), who found small values of $(k'/gh)^{1/2}$ for the field data of George et al. (1994). The values found by Mocke (2001) however, were lower than the values found in this field experiment. According to Mocke (2001), these low values were caused by the limitations in extraction techniques for random waves. This could be possible, since we have also already seen large differences between the different separation methods of the velocity signal.

5.1.5 Contribution u, v and w to TKE

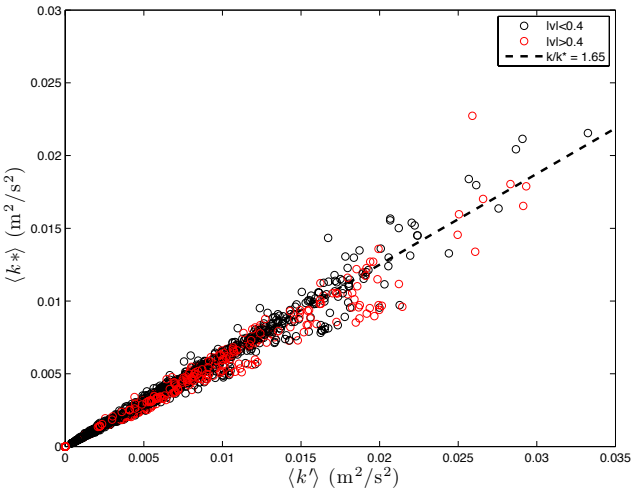

Figure 5.17 Ratio of k to k.*

In laboratory experiments, the transversal component v'^2 is often not measured, and thus the turbulent kinetic energy was calculated as k = 1.33 k*, with $k^* = 0.5(\langle u'^2 \rangle +$

$\langle w'^2 \rangle$). The factor 1.33 comes from turbulence in a plane wake, where u'²:v'²:w'² = 0.43:0.26:0.32. Svendsen (1987) said that the turbulence beneath breaking waves resembles that in a plane wake, and thus k/k* = 1.33. In our data on the other hand, the ratio of k to k* is about 1.65 (Figure 5.17), implying that v'² is more important beneath breaking waves than in plane wake turbulence.

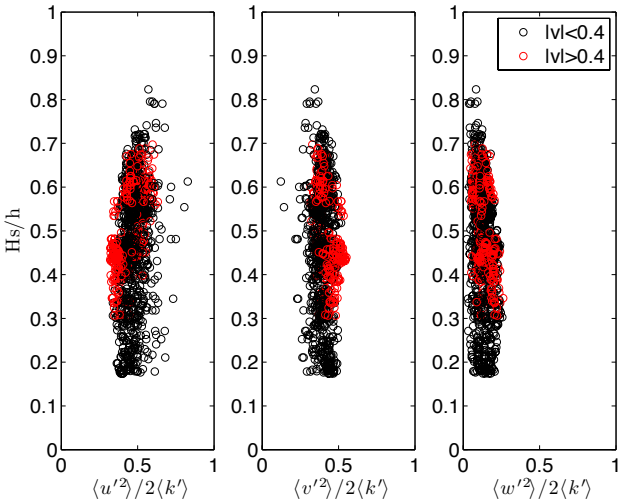

Figure 5.18 Relative contribution of u'², v'² and w'² to turbulent kinetic energy k against relative wave height Hs/h and subdivided in v>0.4 m/s (red) and v<0.4 m/s (black).

The ratio of the u, v and w found from our data is u'²:v'²:w'² = 0.45:0.40:0.15 (Figure 5.18) and thus k/k* = 1.65. The relative contribution of u, v and w does not seem to depend on the degree of wave breaking (relative wave height). However, a trend is visible in the vertical profile (relative position in the water column; Fig.5.19). Lower in the water column, the contribution of w'² decreases, while the contribution of u'² increases. This is probably because the proximity to the bed means that w' is confined. The contribution of v'² to the turbulent kinetic energy seems to be independent of position in the water column.

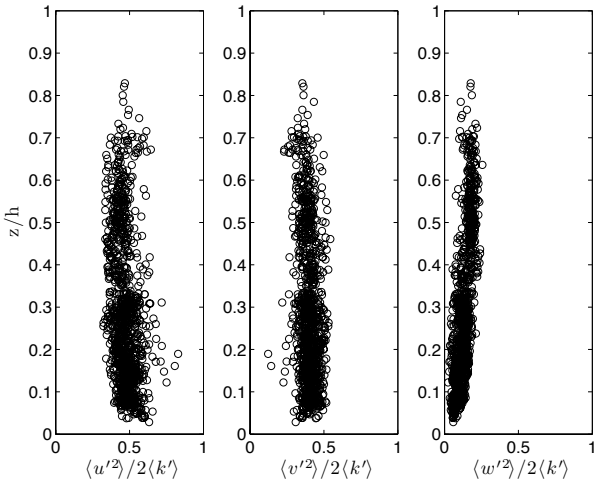

Figure 5.19 Relative contribution of u'², v'² and w'² to turbulent kinetic energy k against relative position in the water column z/h

One could argue that the (relative) high contribution of the transversal component is caused by large alongshore currents and obliquely incoming waves. However, the waves generally had an incoming angle smaller than 15 degrees and the alongshore currents are mostly smaller than 0.4 m/s and always smaller than 0.75 m/s (Fig.5.20). Higher alongshore currents are clearly related to higher incoming wave angles. The red dots in figure 5.17 and 5.18 show the moments when the alongshore current was larger than 0.4 m/s. During higher alongshore currents, the influence of v'^2 indeed seems to be somewhat larger, while the contribution of u'^2 is decreased when the alongshore currents are stronger. However, the contribution of w'^2 does not seem to depend on the alongshore current at all.

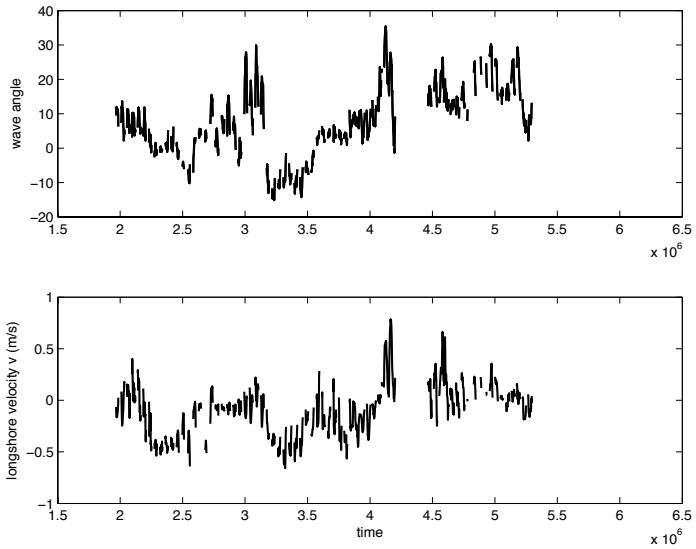

Figure 5.20 (a) wave angle, and (b) alongshore velocity v for the entire 6-week campaign.

5.1.6 Discussion

The turbulent kinetic energy at the upper ADV was generally larger than that of the lower two ADVs, but they do follow the same pattern with peaks at the same time. The turbulent kinetic energy is largest in the upper part of the water column and decreases downward. This is consistent with results from literature (George et al. 1994; Ting & Kirby 1996; Mocke 2001; Scott et al. 2005). So turbulence generated at the surface seems to be spreading downward towards the bed. Probably the turbulence also has a bottom source, as the turbulent kinetic energy at the lower ADV is often slightly larger than at the middle ADV. The shape of the vertical profile of turbulent kinetic energy does not change during different conditions, but the magnitude of turbulent kinetic energy does change.

In large water depths (h>2m), the turbulent kinetic energy rates are largest near the bed, suggesting that the bottom boundary layer turbulence dominates in this case, consistent with the results of Feddersen & Trowbridge (2005). In intermediate water depths (h=0.5-2m), the turbulent kinetic energy is largest higher in the water column, so surface-generated turbulence dominates now. The lack of increase in turbulent kinetic energy from Hs/h = 0.48 and higher suggests that the intensity of wave breaking is relatively unimportant for the turbulent kinetic energy. Furthermore, the turbulent kinetic energy seems to decrease from Hs/h=0.58 onward, suggesting a different type of breaking, or possibly this also has to do with a dependency on the dissipation of short waves. In very small water depths (h<0.5m), the turbulent kinetic energy is largest near the bed, so bed processes are probably very important in this region. This is consistent with the results of Longo et al. (2002) who found that in the swash zone, the bottom turbulence plays a relative important role and can even dominate.

The turbulent kinetic energy was not only related to the degree of wave breaking (relative wave height), but also to the position in the surf zone. Outside the surf zone, where waves are shoaling, the turbulent kinetic energy (and the relative wave height) is low, generally under 0.005 m^2/s^2, which was also found by Trowbridge & Elgar (2001), who found that the turbulence is weak seaward of the breaking zone. In the outer surf zone, where not all waves are breaking, the turbulent kinetic energy is slightly larger, but still rather low (<0.012 m^2/s^2). In the inner surf zone, where all waves are breaking, the turbulent kinetic energy is substantially larger, with values up to 0.03 m^2/s^2, and also more scattered. The larger turbulent kinetic energy closer to the break point was also found by Scott et al. (2005), but they also found that the turbulent kinetic energy more onshore is confined to the upper part of the water column, and thus that the turbulent kinetic energy throughout the entire water column is a localized feature near the wave breaking point. This was not found from our results, since the shape of the vertical profile hardly changed in our results.

The Froude-scaled turbulent kinetic energy was mostly varying between 0.015 and 0.04 and showed a slight vertical trend, suggesting quite weak vertical mixing. The values of the Froude-scaled turbulent kinetic energy are smaller than found during laboratory experiments under regular waves, which is consistent with earlier findings. The contribution of the transversal component (v) to the turbulent kinetic energy was found to be more important than in plane wake turbulence. The ratio of k to k* is about

1.65, while this is 1.33 for plane wake turbulence. Furthermore, the relative contribution of u, v and w does not seem to depend on the degree of wave breaking, but it does show a trend in the vertical profile, where the contribution of u increases (to ± 0.6k) and that of w decreases (to < 0.1k) close to the bed. The importance of the transversal component v to the turbulent kinetic energy seems to increase slightly (less than 0.1k) with increasing longshore currents, but the differences are small.

5.2 Turbulent dissipation

This chapter will discuss results of the turbulent dissipation from the data. Specifically it will be investigated whether turbulent dissipation increases during higher energetic conditions and if the profile of turbulent dissipation changes during these higher energetic conditions. First of all, the change of turbulent dissipation over the entire campaign will be discussed. Then, the vertical profile of turbulent dissipation will be looked at in more detail. And finally, turbulent dissipation will be related to, for example, relative wave height and position in the surf zone.

5.2.1 General results

Time series of the turbulent dissipation were calculated for the entire campaign. The turbulent dissipation was then averaged for each burst to calculate the turbulent dissipation rate. The turbulent dissipation rate was then used to look at the trend of turbulent dissipation and its relation to wave height and breaking intensity.

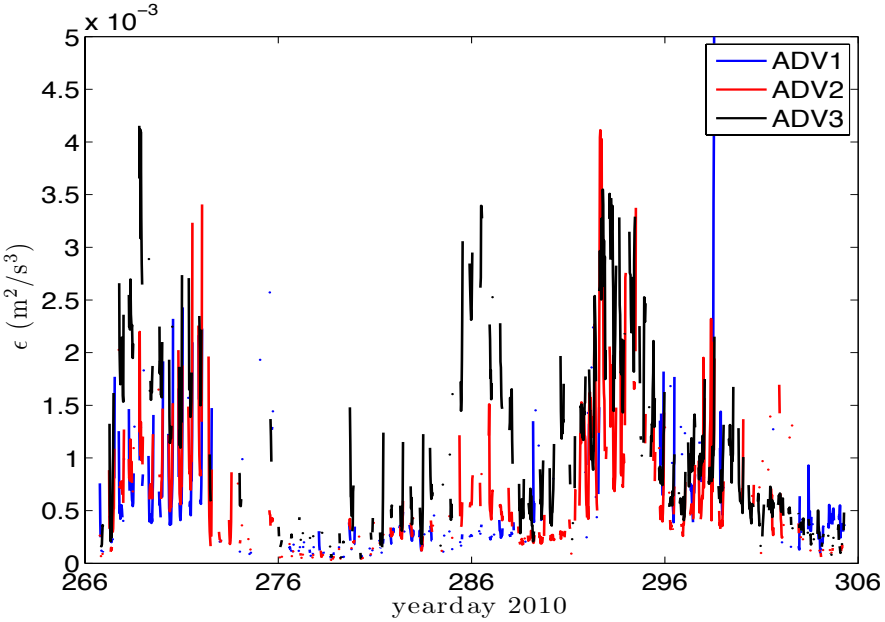

Figure 5.21 Time-averaged turbulent dissipation rates per burst plotted against time for the entire field experiment for ADV1 (blue), ADV2 (red) and ADV3 (black).

Figure 5.21 shows the turbulent dissipation rate per burst for the entire campaign for the three ADVs. The turbulent dissipation clearly varies with wave height, compare to figure 4.4a. During larger wave heights the turbulent dissipation rate is larger as well. During the two high energetic (storm) events (yearday 268-271 and yearday 290-295) the turbulent dissipation is clearly larger than during the low energetic period in

between. Furthermore, the turbulent dissipation seems to vary with the tide, with the largest values around rising and falling tide, and smaller values during high tide, suggesting a relation between the relative wave height Hs/h and the turbulent dissipation rate. The relation between wave height and turbulent dissipation suggests a surface source of turbulence, rather than bottom-generated turbulence. Moreover, the turbulent dissipation is generally larger at ADV3 and decreases downward, which also suggests that the main source of turbulence is from the surface.

5.2.2 Vertical profile

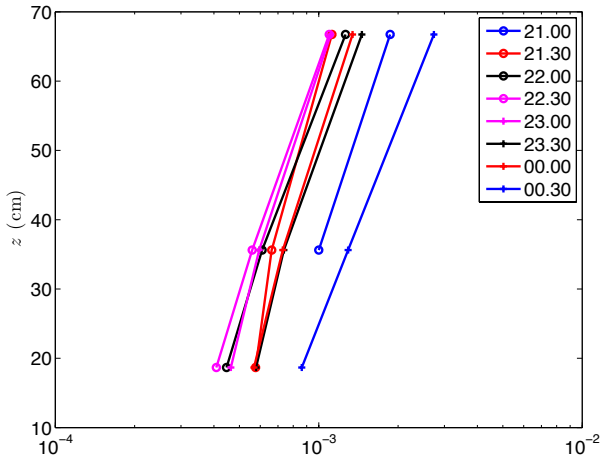

Figure 5.22 Time-averaged vertical profile of turbulent dissipation rates per burst for ADV1-3.

In figure 5.22, the time-averaged vertical profile of turbulent dissipation is shown for one high tide (per burst). The turbulent dissipation is largest during rising and falling tide, and smallest during high tide. This suggests that the turbulent dissipation is either larger with higher relative wave heights Hs/h, or closer to the shoreline (in the inner surf zone). The shape of the vertical profile of the turbulent dissipation does not seem to change during the tide. The dissipation is always largest near the surface and smallest near the bed, which is consistent with dissipation induced by wave breaking.

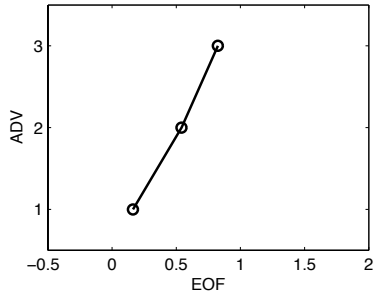

Figure 5.23 Vertical structure of the EOF for turbulent dissipation <epsilon>. This EOF explains 84% of the total variance in <epsilon>.

The vertical structure of the turbulent dissipation was further investigated by doing a EOF analysis. The results of this EOF analysis can be seen in figure 5.23. The EOF is maximum at the upper ADV, indicating that the surface is the dominant turbulent source. The turbulent dissipation then decreases towards the middle ADV and further to the lower ADV. This EOF explained 84% of the variance, indicating that the temporal variation of turbulent dissipation is coherent in the vertical. This shows that the typical vertical structure of turbulent dissipation is maximum near the surface and decreasing downward, supporting the importance of surface-generated turbulence.

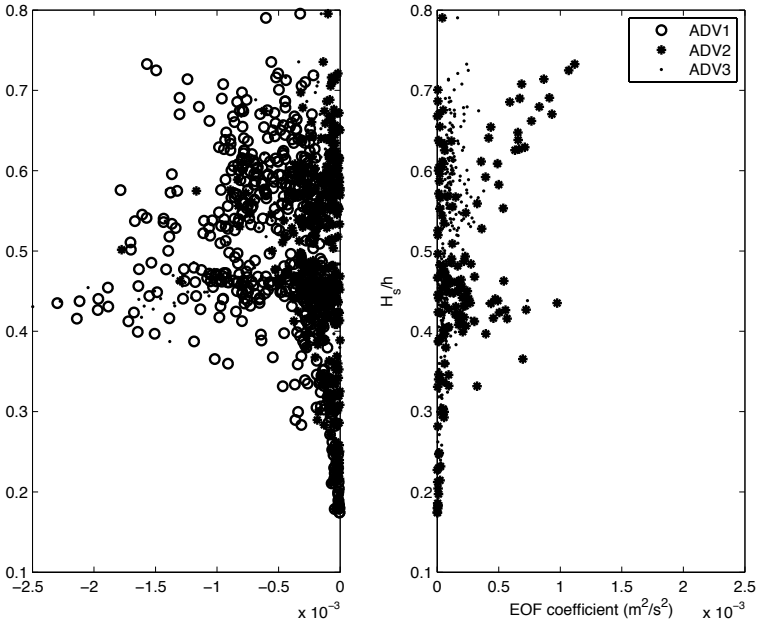

Figure 5.24 (a) negative, and (b) positive coefficients of the first EOF for turbulent dissipation.

The temporal EOF coefficients are shown in figure 5.24. Figure 5.24a and 5.24b show the negative and positive coefficients respectively, these are furthermore subdivided for ADV1, 2 and 3. Clearly, most of the coefficients are negative, which also shows all three ADVs, while there are clearly less positive coefficients and these are only of the upper two ADVs. This indicates that bed-generated and surface-generated alternate in importance. The negative coefficients can indicate upward moving dissipation and thus influence from bed-generated turbulence, while positive coefficients indicate downward moving dissipation and thus surface-generated turbulence. Both positive and negative coefficients increase in magnitude with relative wave height Hs/h, showing a dependency on wave breaking.

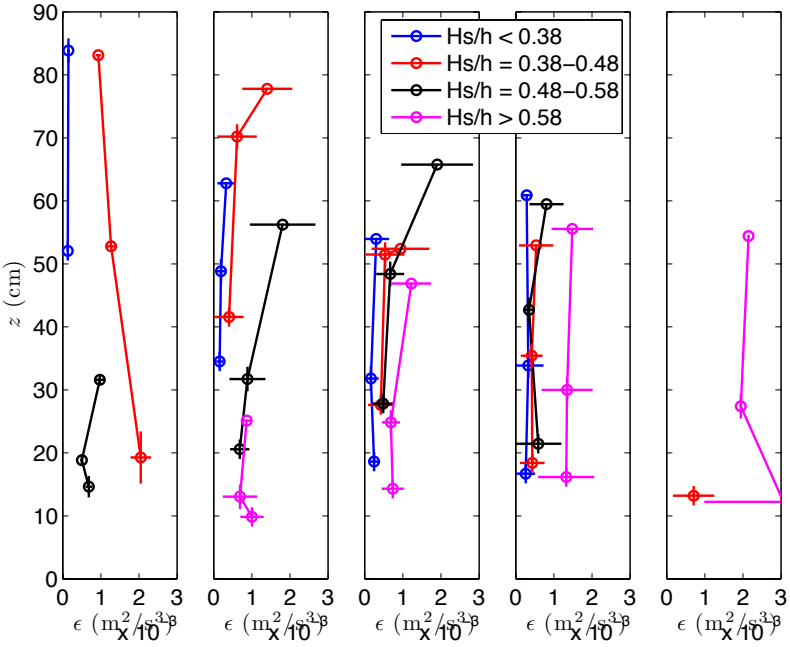

Figure 5.25 Turbulent dissipation rates per water depth, with (a) h > 2m, (b) h = 1.5-2m, (c) h = 1-1.5m, (d) h = 0.5-1m, and (e) h < 0.5m. And relative wave height, with Hs/h < 0.38 (blue), Hs/h = 0.38-0.48 (red), Hs/h = 0.48-0.58 (black), and Hs/h > 0.58 (magenta). The horizontal lines indicate the standard deviation of the turbulent dissipation rates, and the vertical lines indicate the standard deviation of the elevation of each ADV above the bed.

The time-averaged turbulent dissipation rate per burst was then divided into groups of water depths and relative wave heights per ADV. In figure 5.25 these groups of turbulent dissipation are plotted against height above the bed. The most left figure shows the turbulent dissipation rates in the largest water depth (h>2m), while the figure on the right shows the turbulent dissipation rates in the smallest water depth (h<0.5m). The different colours in each subplot indicate different groups of relative wave height, from Hs/h < 0.38 (no breaking, blue line) up till Hs/h > 0.58 (all waves broken, magenta line). The horizontal lines through each point represent the standard deviation of the group of turbulent dissipation rates and the vertical lines through each point represent the standard deviation of the group of elevations above the bed. At the largest water depths (h>2m), the largest turbulent dissipation rates are found near the bed with Hs/h = 0.38-0.48, while the turbulent dissipation rates for Hs/h = 0.48-0.58 are smaller and have a maximum higher up in the water column. This suggests that for the first one the main source of turbulent dissipation is from the bed and not from the surface, while for the larger relative wave heights the surface source is more important, but smaller than the bed source during the lower energetic conditions. The three middle figures, with water

depths varying between 0.5 and 2 m, all show more or less the same. The turbulent dissipation rates are largest higher up in the water column and decreasing downward. This suggests that the surface turbulence is dominant in this region. Furthermore, the turbulent dissipation rates for Hs/h < 0.38 are clearly smallest for all three water depths. These are mostly constant throughout the water column, with no clear trend increasing up- or downward. Possibly the turbulent dissipation rates would increase closer to the bed for this relative water height (suggesting a bottom-generated turbulence source), however, the measurements were mostly done quite high above the bed. In general, the largest increase in turbulent dissipation seems to be from Hs/h < 0.38 to Hs/h = 0.38-0.48. This is generally assumed to be the transition from non-breaking to breaking waves, so this increase in turbulence dissipation again suggests that breaking waves are an important surface source of turbulence. From this group of relative wave heights to the next (Hs/h = 0.48-0.58), the increase of turbulent dissipation is minimal and to the highest relative wave heights (Hs/h > 0.58) the turbulent dissipation even decreases, except for h = 0.5-1 m, where it increases slightly. These more or less constant values of turbulent dissipation rates from Hs/h = 0.48 onward suggest that when eventually all the waves are breaking, the intensity of wave breaking is not very important for the turbulent dissipation. So the turbulent dissipation rate reaches a maximum value and then remains approximately constant. The subplot of the smallest water depths shows a different image. First of all, very little data is available for these small water depths, because these were often rejected by the quality control of the ADV data. Secondly, the data that is available is almost exclusively for Hs/h > 0.58. The profile of the turbulent dissipation rates for this relative wave height shows an increase of turbulent dissipation towards the bed. Although the turbulent dissipation rate higher up in the water column is not smaller than the turbulent dissipation rates for the larger water depths, the turbulent dissipation rate at the bed is much larger. This suggests that closer to the shoreline, in the inner surf zone to the swash zone, turbulence generated at the bed is increasingly more important.

The turbulent dissipation rates were then subdivided in a similar way into different groups for water depth and breaker dissipation (Figure 5.26). Again, the horizontal lines indicate the standard deviation of the turbulent dissipation of the group and the vertical lines indicate the standard deviation of the elevation above the bed. When the breaker dissipation is smaller than 0, the turbulent dissipation is close to 0

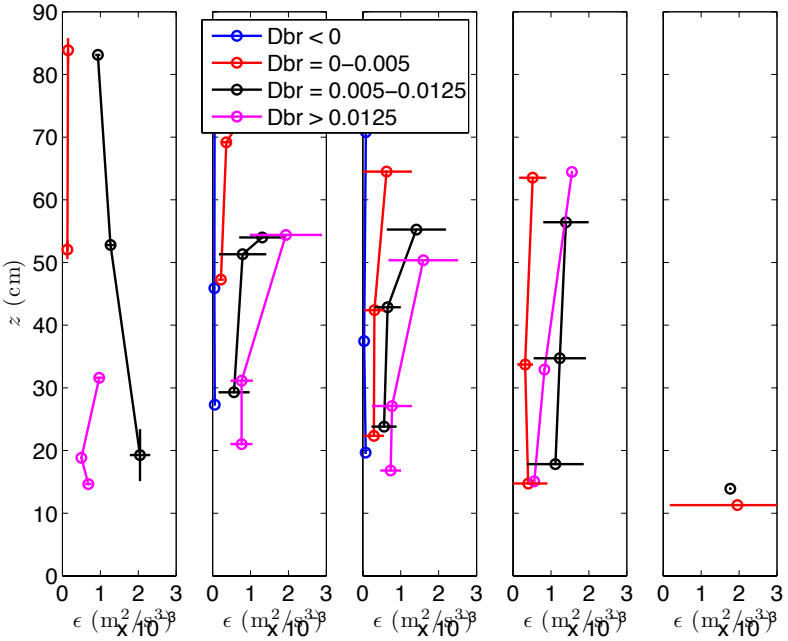

Figure 5.26 Turbulent dissipation rates per water depth, with (a) h > 2m, (b) h = 1.5-2m, (c) h = 1-1.5m, (d) h = 0.5-1m, and (e) h < 0.5m; and total breaker dissipation, with Dbr < 0 (blue), Dbr = 0-0.005 (red), Dbr = 0.005-0.0125 (black), and Dbr > 0.0125 (magenta). The horizontal lines indicate the standard deviation of the turbulent dissipation rates, the vertical lines indicate the standard deviation of the elevation of each ADV above the bed.

throughout the water column, as was expected, because no breaking occurs, so there is no injection of turbulence from wave breaking. Furthermore, it can be seen that for the two intermediate water depth groups (h=1-2m; figure 5.26b-d), the turbulent dissipation generally increases towards the surface, which is consistent with surface-generated turbulence. The turbulent dissipation also seems highly dependent on the breaker dissipation, since it increases for higher breaker dissipation. For the largest water depth (h>2m), the turbulent dissipation seems to increase towards the bed for Dbr = 0.005-0.0125, consistent with bed-generated turbulence. In the case of the largest breaker dissipation, the turbulent dissipation is smaller. For h=0.5-1m, the turbulent dissipation seems more or less uniform throughout the water column, except for the largest breaker dissipation Dbr > 0.0125, where it does increase towards the surface. This uniformity throughout the water column can indicate that the vertical mixing is good. Another explanation is that both bed and surface generated turbulence are important, so the dissipation at the top ADV is due to surface generated turbulence, while the dissipation at the lower ADV is due to bed generated turbulence. However, the standard deviation is quite large, so it is also possible that bed and surface generated

turbulence are important alternately. For the smallest water depth (h<0.5m) there was hardly any consistent data that passed the quality tests and for which at the same time a height measurement was available, as can be seen in figure 5.26e.

5.2.3 Characteristics and position in surf zone

Now, the dependency of turbulent dissipation on various parameters is investigated. In figure 5.27 the turbulent dissipation rates are plotted against water depth, significant wave height, total breaker dissipation, relative wave height and relative position in the water column. The turbulent dissipation does not seem to depend on the water depth, or relative position in the water column. The dissipation does not clearly increase or decrease with water depth or position in the water column. However, there does seem to be a relation between the (relative) wave height and the turbulent dissipation. The turbulent dissipation found at wave heights above approximately 0.4 m seems to be slightly increasing with wave height, but below this 0.4 m the dissipation decreases faster. At the relative wave height a turning point is found at about Hs/h = 0.5. Above this point, the dissipation is almost uniform, but below this point it clearly decreases with decreasing relative wave height. This value of relative wave height (0.5) can be seen as the value above which all waves are breaking. This suggests that the turbulent

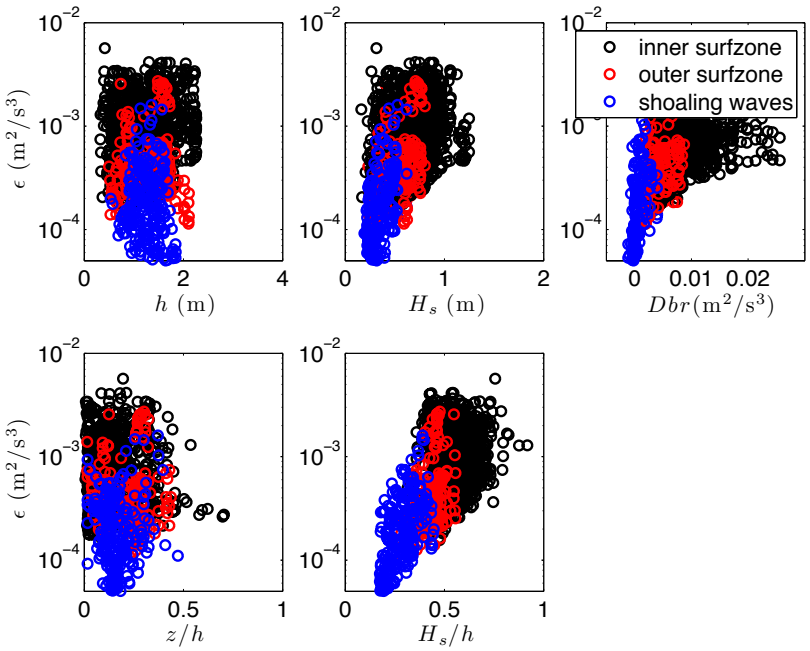

Figure 5.27 Turbulent dissipation rates per burst against (a) water depth h, (b) significant wave height Hs, (c) total breaker dissipation Dbr, (d) relative position in the water column z/h, and (e) relative wave height Hs/h. Divided into inner surf zone (black), outer surf zone (red) and shoaling waves (blue).

dissipation under (fully) breaking waves is not dependent on the intensity of wave breaking, while below this point, the dissipation does depend on the relative wave height and decreases with decreased wave breaking.

Then, the dependency of turbulent dissipation on position in the surf zone is investigated. The turbulent dissipation rates are divided for relative position in the surf zone (according to the model of Battjes-Janssen, Ch.5.1.3). The blue points in the plots indicate shoaling waves, the red point represent the outer surf zone and the inner surf zone is represented by the black points. The turbulent dissipation rate and position in the surf zone are clearly related. The turbulent dissipation rate increases going from shoaling waves to the outer surf zone and then to the inner surf zone. While the dissipation rate seems to be dependent on (relative) wave height for the shoaling waves and the outer surf zone, it seems to be independent of those in the inner surf zone. In the inner surf zone, the range of turbulent dissipation rates is quite large, but no trend of increasing turbulent dissipation with (relative) wave height is visible. In figure 5.27a and 5.27c it can be seen that the turbulent dissipation rate does not depend on the water depth and the relative position in the water column, but it does increase going from the breaker point to the shoreline.

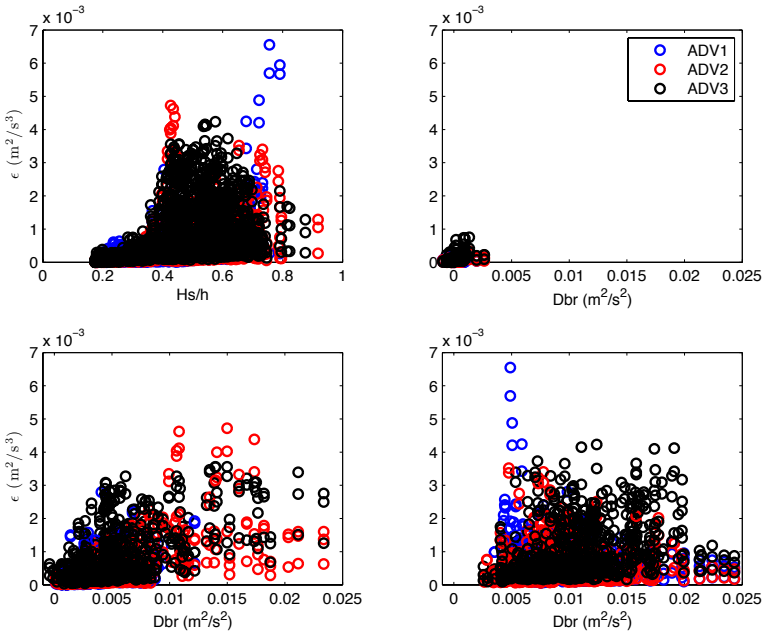

Figure 5.28 (a) Turbulent dissipation rate against Hs/h, and turbulent dissipation rate against breaker dissipation Dbr, for (b) Hs/h<0.3, (c) 0.3<Hs/h<0.5, and (d) Hs/h>0.5.

Since the turbulent dissipation appeared to be related to relative wave height and total breaker dissipation (Fig.5.25), the turbulent dissipation rates were divided into three groups of relative wave height (Hs/h<0.3, Hs/h=0.3-0.5, Hs/h>0.5), shown in figure 5.28b-d respectively. For the smallest relative wave heights, both the turbulent dissipation and breaker dissipation are always small, which is consistent with breaker induced turbulence being important for turbulence dissipation, rather than bed-generated turbulence. For relative wave heights between 0.3 and 0.5, when waves start breaking, the turbulent dissipation is clearly larger and it increases with total breaker dissipation, as expected when surface-generated turbulence is important. For the highest relative wave heights, when all waves are breaking, both the turbulent dissipation and the breaker dissipation are larger and they are slightly positively related. This all supports that surface-generated turbulence due to wave breaking is important for turbulence, rather than bed-generated turbulence.

5.2.4 Discussion

The turbulent dissipation was found to increase with wave height and during higher energetic conditions. Furthermore, the turbulent dissipation varies during the tide; it is largest around rising and falling tide and smaller at high tide. The turbulent dissipation is generally larger at the upper ADV and decreasing downward. This suggests that the main source of turbulence is surface-generated. This is consistent with the results of Huang et al. (2009), who also found that the turbulent dissipation is largest near the surface and decaying downward. However, in their case the turbulent dissipation decayed exponentially towards the bed, while our results show a more or less linear decay, which suggests slower decrease of turbulent dissipation. It must be taken into account however, that the experiment of Huang et al. (2009) was done in the laboratory with scales in the order of millimetres, so scaling problems could arise.

The vertical profile of turbulent dissipation does not change during a tide, although the magnitude does change. The turbulent dissipation rate does not depend on water depth or position in the water column. However, it does increase going from outside the surf zone (shoaling waves) to the outer surf zone and then into the inner surf zone. The dissipation at relative wave heights above approximately 0.5 seems to be constant. Below this point it clearly decreases with decreasing relative wave height. So the turbulent dissipation under (fully) breaking waves is not dependent on the intensity

of wave breaking, while below this point, the dissipation does depend on the relative wave height and increases with it. George et al. (1994) also found that the dissipation rates increase when the fraction of broken waves increases, so this is consistent with our results.

At large water depths (h>2m), the turbulent dissipations rates are largest near the bed. So in this region, the bed-generated turbulence is probably most important. In intermediate water depths (h=0.5-2m), the turbulent dissipation rates are largest higher up in the water column, and decreasing downward. This suggests that the surface turbulence is dominant in this region. In these water depths, the turbulent dissipation is almost constant from Hs/h = 0.48 and higher, so the breaking intensity does not seem very important for the amount of turbulence dissipation. From Hs/h = 0.58 onward, the turbulent dissipation is even slightly decreasing, which could be due to a change in the type of breaking. At very small water depths (h<0.5m), the turbulent dissipation rate is largest near the bed. So in this region, the bed-generated turbulence is probably very important. The increasing dissipation rates with decreasing water depth in the inner surf zone and swash zone are consistent with results from literature (Sou et al. 2010).

6. Sediment suspension and relation to TKE

This chapter will discuss the sediment concentration results and the relation between sediment suspension and turbulent kinetic energy. First, some results of sediment concentration will be discussed, looking at the general pattern during the field experiment and more specifically at the vertical profile and the characteristics and position in the surf zone. Then, the relation between sediment suspension and turbulent kinetic energy will be discussed; looking closely at the question whether sediment suspension under breaking waves can be related to turbulence and if sediment suspension is dominated by surface-generated turbulence. This will then also be related to relative wave height and energy conditions.

Time series of the sediment concentration at five positions in the water column were available for the entire field experiment. These were also time-averaged to be able to have a look at the trends of high sediment concentrations during high- and low-energetic conditions. The time-averaged sediment concentration per burst is plotted in figure 6.1. The time-averaged value of c varies mostly between 0 and 1 g/L, with maxima up to 2 g/L. The period from yearday 292-295, where there is no data, the concentration meters were often buried in the bed, so the bursts were cleaned for this. If the lowest STM of the array was below the bed, the data for all 5 STMs was set to NaN. In general, the sediment concentration is largest during rising and falling tide, and smallest during high tide. The sediment concentration is apparently not directly dependent on the wave height, as the sediment concentration is not higher during the first high energetic period (yearday 268-272) and not decreasing afterwards.

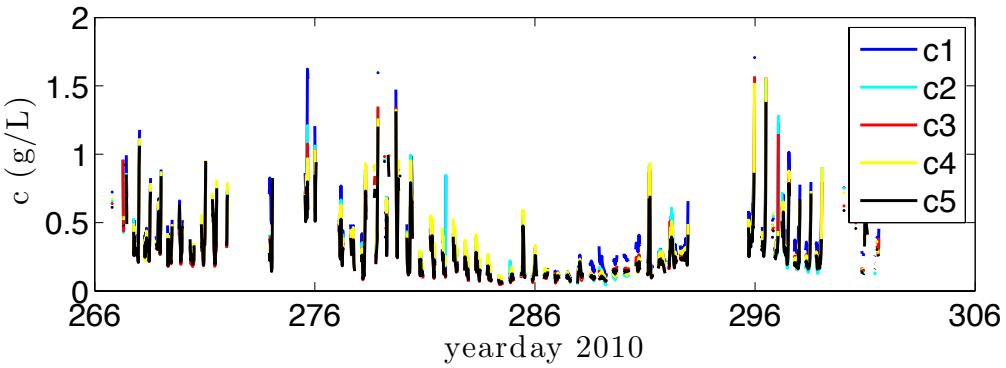

Figure 6.1 Time-averaged sediment concentration per burst for the entire field experiment.

6.1 Vertical profile

As the sediment concentration was measured at five different vertical positions in the water column, also vertical profiles could be investigated. Figure 6.2 shows burst-averaged vertical profiles of the sediment concentration during several high tides in the first week, when the instrument heights were more or less constant and the OBSs were located close to the bed (Fig.6.3). The vertical profiles are divided for different relative wave heights. The blue lines represent a relative wave height smaller than 0.3, the red lines indicate a relative wave height between 0.3 and 0.5, while the black line indicate the largest relative wave heights above 0.5. In all these cases, the sediment concentration is more or less uniform in this segment of the water column, which indicates good vertical mixing in the lower 20 cm of the water column. Furthermore the sediment concentrations are generally very small, indicating that the waves are not very effective in suspending sediment. The largest relative wave heights clearly represent the largest sediment concentration, indicating that the sediment suspension is related to wave breaking. However, there is no difference in magnitude between the two groups of smaller relative wave height. This indicates that when waves start to break, but are not all breaking, sediment suspension is not higher than during non-breaking, shoaling wave conditions.

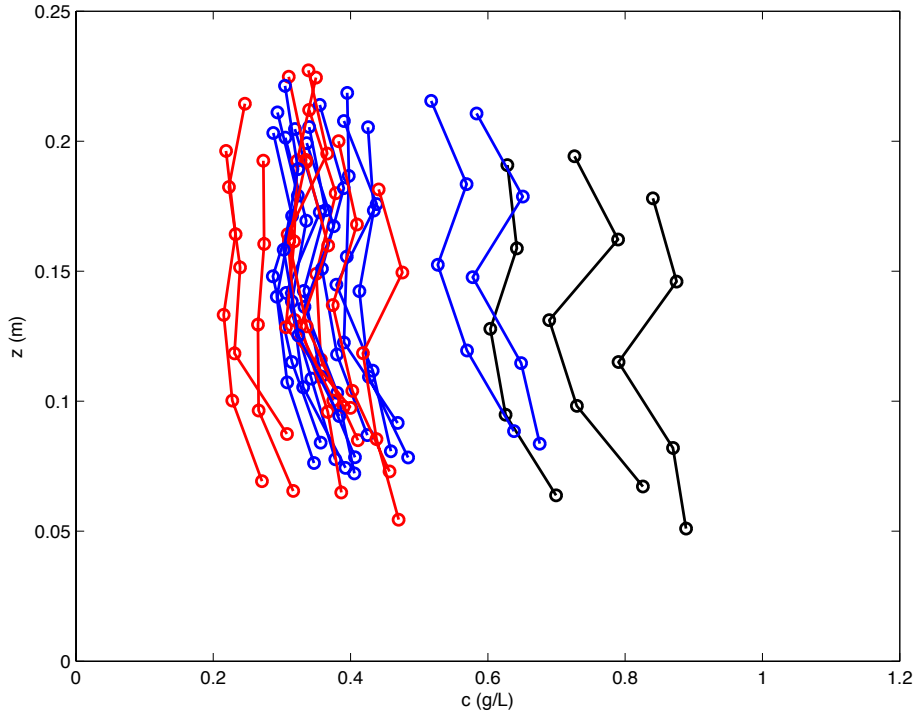

Figure 6.2 Time-averaged vertical profile of sediment concentration per burst for Hs/h<0.3 (blue), 0.3<Hs/h<0.5 (red), and Hs/h>0.5 (black).

Figure 6.3 shows the height of the lowest OBS above the bed, the other OBSs were located in an array within 20cm above the lowest OBS. At the start of the campaign, this was set at about 3 cm, and during the first week this slightly varied between 0 and 10 cm above the bed. Then, a lot of erosion occurred and the instrument height increased dramatically, which was later corrected by lowering the instruments, after which the bed started accreting and eroding quite rapidly again. The bed level was determined by using a ripple profiler (SRPS). This instrument not only shows a scan of the bed and thus indicates ripples or flat bed, but also gives a height above the bed and from this the bed level was determined. This was done by taking the middle 10 cm of the scan of the bed and taking an average of the bed level in this segment. Although generally no ripples occurred during the field experiment, the presence of ripples could possibly affect the results of these bed level calculations.

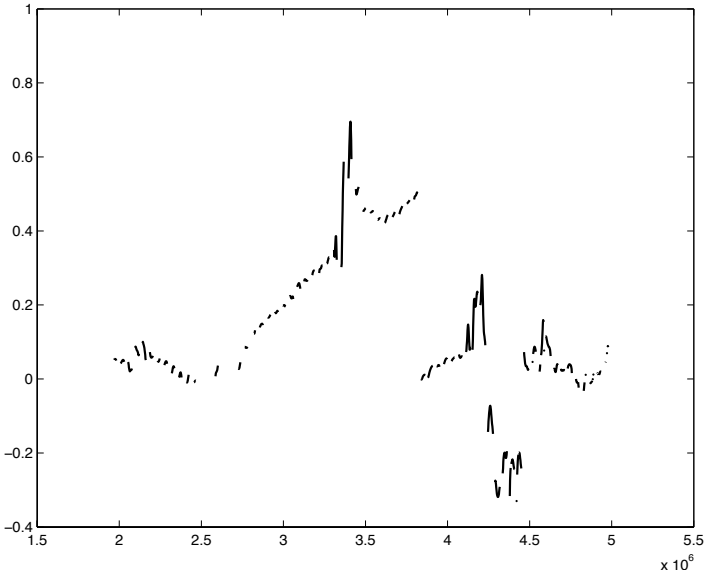

Figure 6.3 Height of the lowest OBS above the bed for the entire field campaign.

6.2 Characteristics and position in surf zone

Now the time-averaged sediment concentrations are investigated further for correlations with water depth, significant wave height etcetera. In figure 6.4 the time-averaged sediment concentration per burst is plotted against water depth h, relative position in the water column z/h, significant wave height Hs and relative wave height Hs/h. The trends are not very strong, the data is very scattered. The sediment concentration seems to decrease slightly with increasing water depth, while it seems to be independent of the significant wave height. The sediment concentration increases slightly with relative wave height. This is consistent with the findings of Aagaard &

Hughes (2010), who found that the sediment concentrations are much higher under broken waves. However, the correlation found in this case is much weaker than what Aagaard & Hughes (2010) found. Also a weak correlation is visible between the relative position in the water column and the sediment concentration. As could be expected, higher up in the water column, the sediment concentration decreases.

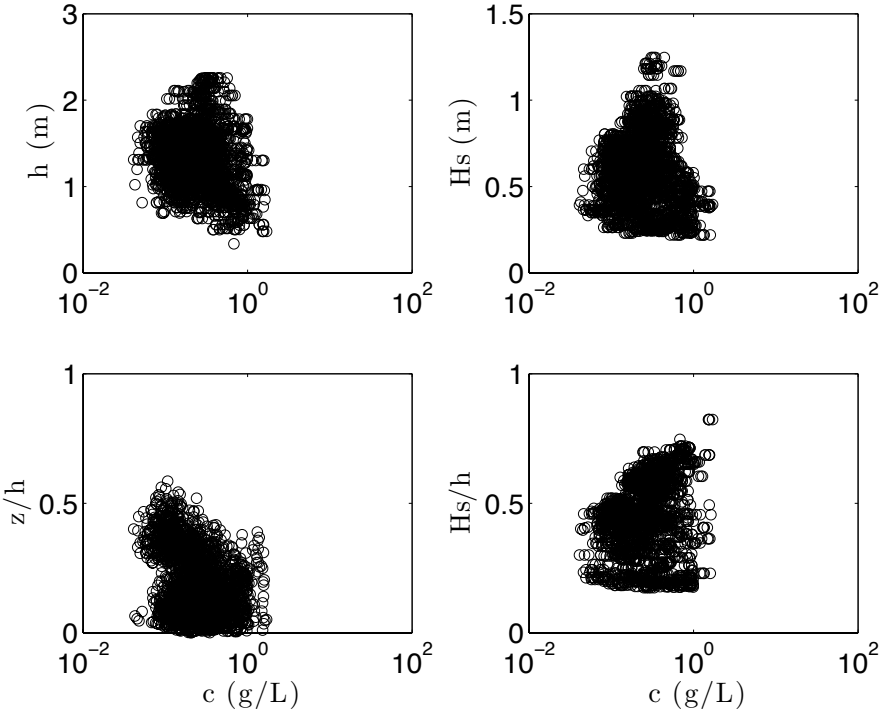

Figure 6.4 Sediment concentration c against (a) water depth h, (b) significant wave height Hs, (c) relative position in the water column z/h, and (d) relative wave height Hs/h.

It has to be taken into account that the OBSs were located at very different heights above the bed throughout the field experiment, as was shown in figure 6.3, so this may also influence the results. Therefore, a closer look was taken at the first week of measurements, when the instrument height was relatively constant and close to the bed. These results are shown in figure 6.5; here, the sediment concentration is plotted against water depth, significant wave height, relative position in the water column and relative wave height. There is a clear relation between the sediment concentration and water depth and significant wave height. The sediment concentration is largest for the smallest water depths and also the smallest wave height, then decreasing quite rapidly for larger water depths and wave heights and then remaining more or less constant. This indicates that the sediment concentrations are largest closer to the shoreline (in the smallest water depths). Furthermore, the sediment concentration increases with

relative wave height, indicating a relation between sediment suspension and wave breaking. Surprisingly, no clear relation was found between sediment concentration and position in the water column, which was also seen in the vertical profile, indicating that vertical mixing of sediment is good. This uniformity is also affected by the fact that all the measurements shown here were done in the lower 20 cm of the water column.

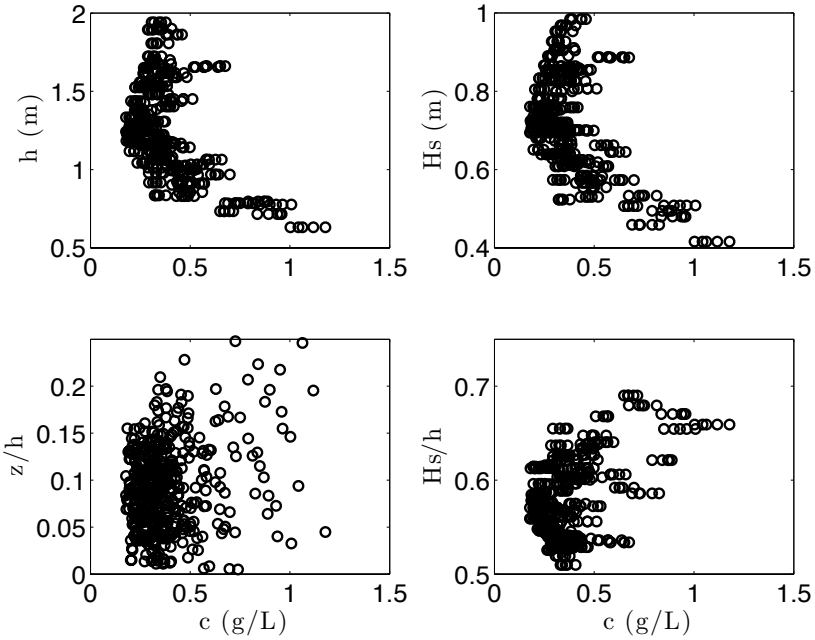

Figure 6.5 Sediment concentration c against (a) water depth h, (b) significant wave height Hs, (c) relative position in the water column z/h, and (d) relative wave height Hs/h. Subdivided in shoaling waves (blue), outer surf zone (red) and inner surf zone (black).

6.3 Relation TKE and sediment suspension

Under breaking waves, turbulence generated at the surface can penetrate downward through the water column, hit the bed, and thus provide an additional mechanism to suspend sediment. To relate the sediment suspension to turbulent kinetic energy generated at the surface, time series of turbulent kinetic energy and sediment concentration were compared. To be able to quantify the relation between the turbulent kinetic energy and sediment suspension, in both time series peaks were defined. This was done using a threshold value. Everything above this threshold was assumed to be a peak. The threshold that was used was 4 times the standard deviation of each time series for both the turbulent kinetic energy and the sediment concentration. This relatively high threshold was chosen because the probability density function of the time series is very kurtosed. To determine this, the kurtosis of each time series was

calculated. The kurtosis K_a of a demeaned time-series 'a' is defined as $\langle a^4 \rangle / \langle a^2 \rangle^2$ and equals 3 for a Gaussian distributed series. For our data the kurtosis found was generally between 20 and 200, with extremes up to 1000. This suggests that the intermittency of the time series is very high and that high turbulent kinetic energy is restricted to a very small percentage of a burst.

Figure 6.6 shows an example of time series that were used to compare sediment concentration and turbulent kinetic energy. The upper figure (Fig.6.6a) shows a time series of half an hour of the turbulent kinetic energy; the third figure (Fig.6.6c) shows the time series of half an hour of the sediment concentration. The figures immediately below those (Fig.6.6b and d) give a 0 for every point that was found not to be a peak and 1 for every point that is a peak. The peaks were determined as discussed earlier.

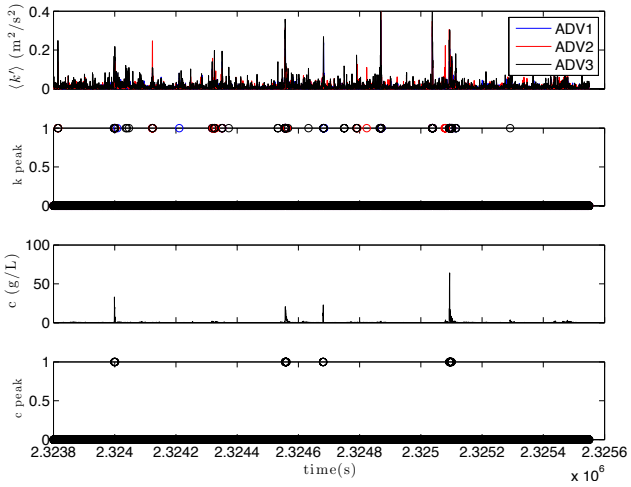

Figure 6.6 Time series of (a) turbulent kinetic energy k and (c) sediment concentration c for 1 burst, and (b) the peaks found from the time series of turbulent kinetic energy k, and (d) the peaks found from the time series of sediment concentration c.

Clearly much more peaks are found in the turbulent kinetic energy time series than in the sediment concentration, which suggests that a relatively small portion of the turbulent events reach the bed and stir the sediment. The ADVs and OBSs were located in a slightly different cross-shore and longshore location, the approximate horizontal distance between the ADVs and OBSs was about 1m. This has to be taken into account when the relation between two timeseries is determined. After the peaks in the time series were defined, the relation between these peaks could be calculated. This was done by assuming that a peak in sediment concentration is related to turbulent kinetic energy if there is also a peak in turbulent kinetic energy within one wave period before the concentration peak. An example of this is shown in figure 6.7, which shows a time

series of 60 seconds of turbulent kinetic energy and sediment concentration with the relation between these time series below that. The relation figure shows the sum of the peaks found within a wave period of each concentration peak. So a number of 10 in the lower figure means that in the 24 points (T = 6, Fs = 4Hz) before the concentration peak, 10 turbulent kinetic energy values higher than the threshold value were found. So the peaks shown in figure 6.7 can clearly be related to each other.

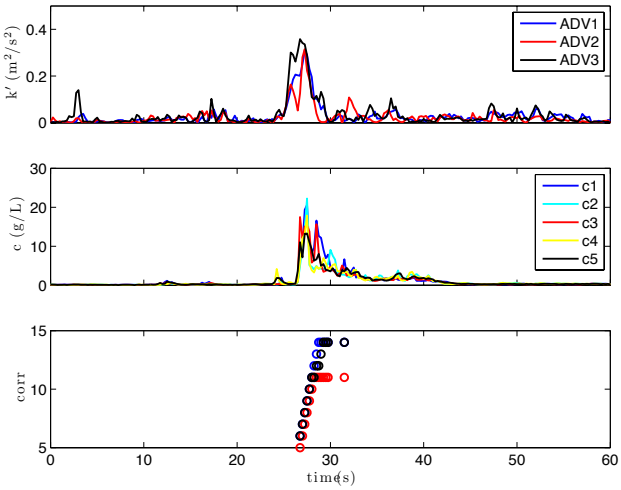

Figure 6.7 Time series of 60 sec of (a) turbulent kinetic energy k, (b) sediment concentration c, and (c) relation between concentration peaks and turbulence peaks, where 0 is no relation.

In figure 6.8 on the other hand, another time series of 60 s is shown of the turbulent kinetic energy (upper one), sediment concentration (middle one) and relation between those (lower one). Here, peaks are clearly found in the concentration series, but these could not be related to the turbulent kinetic energy, so the turbulent kinetic energy peaks and concentration peaks are not related.

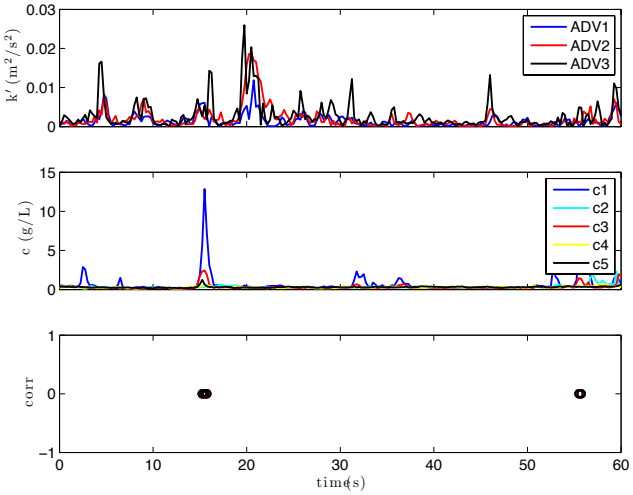

Figure 6.8 Time series of 60 sec of (a) turbulent kinetic energy k, (b) sediment concentration, and (c) relation between concentration peaks and turbulence peaks, where 0 is no relation.

Figure 6.7 reveals an obvious flaw in the method that was used, since a large turbulence event will be shown as multiple peaks, while it should be one peak for one turbulence event. This could influence the results of the relation between turbulent kinetic energy and sediment suspension. The best method to define large peak events as a single peak is the method of Scott et al. (2009), who first did a wavelet analysis on the time series and then used a 9-point block-filter. This block-filter determined the peaks by looking at 9 points at a time and defining only those points as peaks that were higher than the surrounding 8 points. This way, only the highest point of a turbulence event would be defined as a peak. To account for large clouds of turbulence (that have a longer duration than 1 data point), using this more simplistic method, it was assumed that not more than one turbulence peak could occur during one wave period. So if there were 20 peaks found during one wave period, this was assumed to be one consistent turbulence event and this was then reduced to one peak.

The percentage of peaks of turbulent kinetic energy and sediment concentration that could be related was then calculated per burst. The results of these calculations are plotted in figure 6.9 for the entire field experiment. A value of 30 indicates that 30% of the concentration peaks are related to turbulent kinetic energy peaks during the entire burst. For this computation, the cleaned time series of peaks were used, with just one peak for each turbulence event. During the first week of the field experiment, between 40% and 100% of the sediment concentration peaks were preceded by a peak in turbulent kinetic, and this increased during rising and falling tide. This indicates that the relation increases with higher energetic conditions and in the inner surf zone. However, the second period with high energetic conditions (yearday 290-295) is not represented by higher percentages of the relation between turbulent kinetic energy and sediment concentration. After this first period, the relation is quite constant with values varying between 10% and 40%, with again larger values during rising and falling tide. So clearly sediment concentration peaks can be related to turbulence generated at the surface. Surface-generated turbulence does seem to dominate as a sediment suspension process during the first high energetic period, but later on, it seems to be not the only process important for sediment suspension.

It is not clear why during the second period of high energetic conditions the relations are not similarly elevated. A possible influence on this lower relation is the large fluctuations of the height of the OBSs above the bed, as was shown in figure 6.3. In

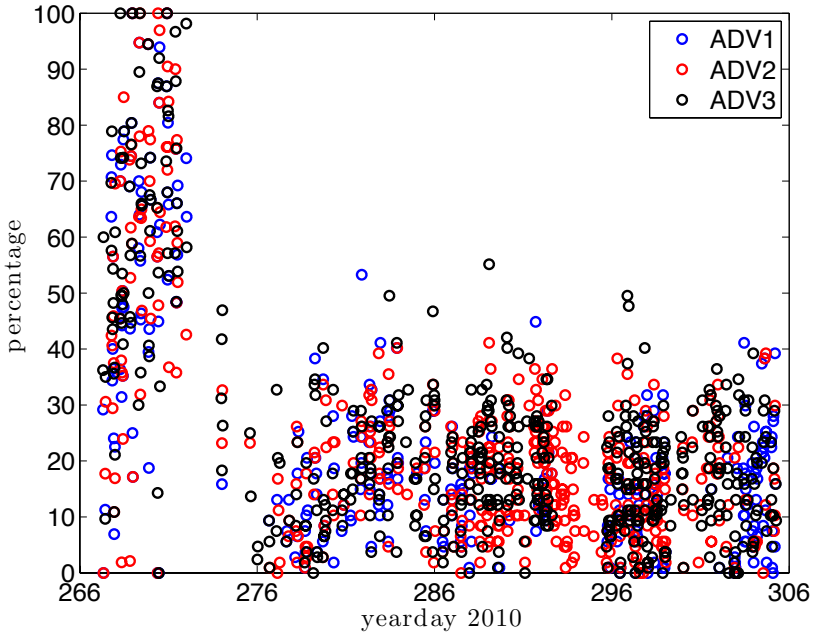

Figure 6.9 Time-averaged relation between sediment concentration and turbulent kinetic energy per burst in percentages (where 0% means no relation between concentration peaks and turbulence peaks during 1 burst and 100% means that all concentration peaks of 1 burst can be related to turbulence peaks).

the first week, both the OBSs and ADVs were located close to the bed. After this, the height of the OBSs increased rapidly, resulting in fewer sediment peaks and also making a relation between sediment concentration and turbulent kinetic energy less likely. Another possible explanation for this is that the type of wave breaking was different. Two main types of breaking can occur, spilling and plunging waves. Plunging waves are more efficient in stirring the sediment as the turbulent kinetic energy is higher throughout the entire water column, while that of spilling breakers is generally more confined to the upper part of the water column and decaying quickly downward (Aagaard & Hughes 2010). However, because of the horizontal vortices associated with plunging breakers, the vertical distribution of the stirred sediment is limited. For spilling waves, the opposite is valid. Although these are not very efficient in stirring the sediment, the oblique vortices that occur under spilling waves cause strong vertical mixing of the sediment (Zhang & Sunamura 1990, Voulgaris & Collins 2000). So this difference could also cause the difference in relation between the two high energetic periods. Furthermore, some of the data of this period was lost, due to a large change in the bed elevation. During the beginning of this storm, the bed accreted approximately 40 cm at the rig (Fig.4.4f), causing some of the instruments that were high above the bed at first, to be sanded in. During the rest of this high energetic period the rig could not be

reached, so during most of this period no data was collected by the lower ADVs. Since there is no data available to support a difference in the type of wave breaking, the difference between the first high energetic period and the second one is most likely to be caused by the difference in instrument height above the bed.

The relation per burst is then plotted against water depth h, significant wave height Hs, relative position in the water column z/h, and relative wave height Hs/h (Fig.6.10). No clear trend is visible in either of these graphs. However, the higher relations (above 50%) seem to occur at high significant wave heights and relative wave heights. This indicates that the observation made from the former graph is correct, that the high relations occur at high energetic conditions.

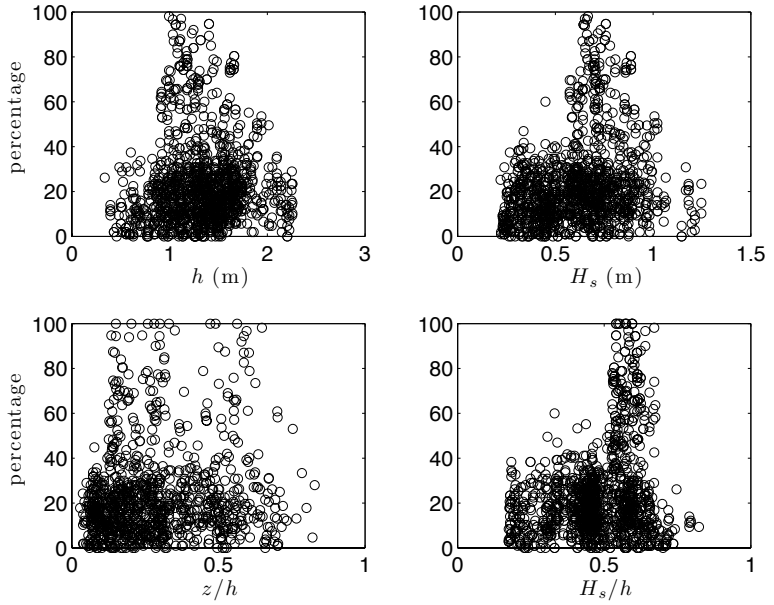

Figure 6.10 Relation between sediment concentration and turbulent kinetic energy against (a) water depth h, (b) significant wave height Hs, (c) relative position in the water column z/h, and (d) relative wave height Hs/h.

Then, the relation was calculated again, but now it was done the other way around. The time series of turbulent kinetic energy were checked for peaks and then sediment concentration peaks were searched within one wave period after the turbulent kinetic energy peak. Then again the percentage of related peaks per burst was calculated. The time series of these relation percentages are shown in figure 6.11. This figure shows a similar pattern as figure 6.9. During the first week, when the conditions were high energetic, the relation between turbulent kinetic energy and sediment concentration was highest, up to 70%. During the rest of the campaign, this varied between 10% and 30%. The fact that all these values are smaller can be explained by what was seen earlier on, namely that more peaks are found in the turbulent kinetic energy than in the sediment concentration. This indicates that not all turbulent kinetic energy peaks

penetrate the water column and hit the bed, or that no sand passes the sensor, since the sensor were not located at the exact same position.

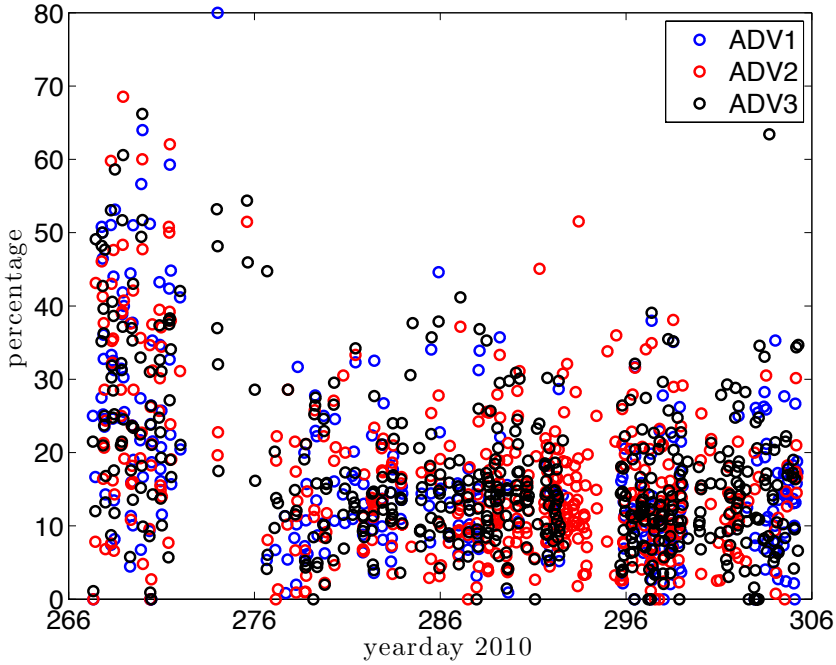

Figure 6.11 Time-averaged relation between turbulent kinetic energy and sediment concentration per burst in percentages (where 0% means no relation between turbulence peaks and concentration peaks during 1 burst and 100% means that all turbulence peaks of 1 burst can be related to concentration peaks).

The relation per burst was also plotted again against water depth, significant wave height, relative position in the water column and relative wave height (Fig.6.12). No clear trend is visible, although there does seem to be some increase in relation with significant wave height and relative wave height, as was also seen in figure 6.10. However, this trend is less obvious then in figure 6.10, which can be explained by the smaller (range in) values.

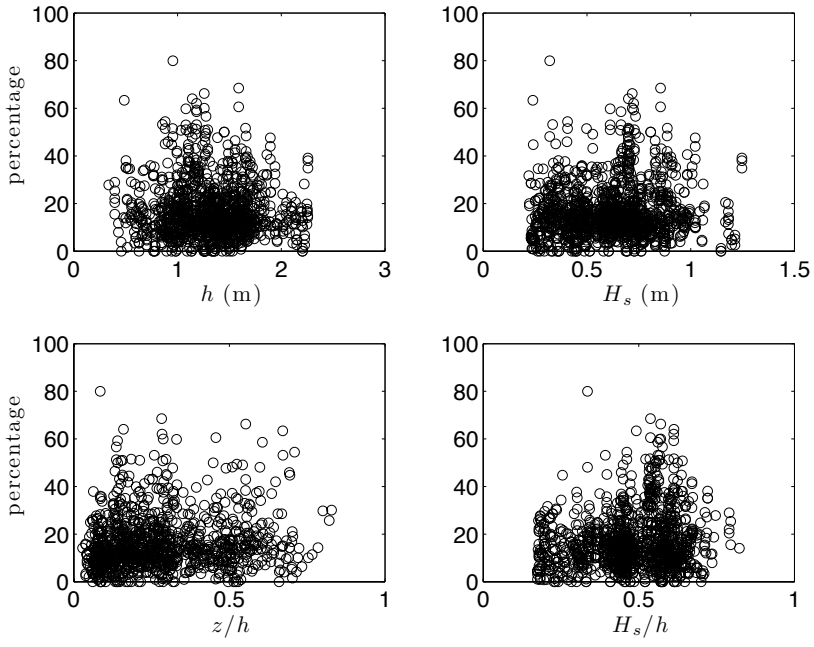

Figure 6.12 Relation between turbulent kinetic energy and sediment concentration against (a) water depth h, (b) significant wave height Hs, (c) relative position in the water column z/h, and (d) relative wave height Hs/h.

6.4 Discussion

The sediment concentration was found to depend on water depth, wave height and relative wave height. The sediment concentration was higher during the higher energetic periods. This is consistent with the results of Ogston & Sternberg (2002), who found that the suspended sediment concentrations are much higher under broken waves, especially higher up in the water column. The sediment concentration did not seem to depend on the position in the water column, and was thus quite uniform in the lower part of the water column where the measurements were taken.

More peaks are present in the turbulent kinetic energy time series than in that of the sediment concentration. This indicates that probably a relatively small portion of the turbulent events reach the bed and stir the sediment. The relation found between sediment suspension and turbulent kinetic energy was highly variable with time. During high energetic conditions in the first week of the experiment, the values were sometimes up to 90%, while during a large amount of time the values were between 10 and 40%. This large difference is most likely caused by a difference in the measuring height of the instruments during these periods. The values increased during rising and falling tide and increased with amount of breaking and higher energetic conditions (especially the highest values are found at high energetic conditions). The sediment concentration peaks can thus clearly be related to turbulence generated at the surface.

The relation between turbulent kinetic energy and sediment suspension (so the other way around) was clearly smaller than the one discussed earlier, but this does show the same trend. During the high energetic period at the start of the experiment, the values were generally higher (in this case up to 70%). This increase was visible for high relative wave heights and during rising and falling tide. The values during the rest of the campaign generally varied between 10 and 30%. These smaller values can be explained by the fact that more peaks are found in the turbulent kinetic energy than in the sediment concentration. So clearly not all turbulent kinetic energy peaks penetrate the water column fully and hit the bed.

The large range of values of the relation between sediment suspension and surface-generated turbulence was also found in the literature. Scott et al. (2009) found that sand suspension events caused by locally generated breaking-wave turbulence only accounts for 15- 33% of the total number of high concentration events. Aagaard &

Hughes (2010) on the other hand, found that sediment suspended by breaker vortices increases with the turbulence intensity, with high ratios up to 88%. They also found that there is some relation between the sediment suspended by breaker vortices and the relative wave height, which was also shown in our results.

7. Conclusion

The turbulent kinetic energy was found to be largest during higher energetic conditions and smaller during calm conditions. The turbulent kinetic energy is largest in the upper part of the water column and decreases downward. So turbulence generated at the surface seems to be spreading downward towards the bed. Turbulence also has a bottom-source, as the turbulent kinetic energy at the lower ADV is often slightly larger than at the middle ADV. The Froude-scaled turbulent kinetic energy also shows a vertical trend, decreasing downward, supporting a downward spreading surface-generated turbulent kinetic energy. The magnitude of turbulent kinetic energy over the entire vertical profile changes during different energy conditions, but the shape of the vertical profile remains more or less the same. In the surf zone (intermediate water depths, h=0.5-2m), the turbulent kinetic energy is large, and larger higher up in the water column, indicating that surface-generated turbulence dominates here, and it increases for higher energetic conditions. In both larger water depths (h>2m), where waves are not breaking, and smaller water depths (h<0.5m), in the swash zone, turbulent kinetic energy is largest near the bed, indicating that bed processes are important here.

Turbulent dissipation increases with wave height and during higher energetic conditions. The turbulent dissipation is generally larger at the upper ADV and decreasing downward, so the main source of turbulence is surface-generated. The shape of the vertical profile of turbulent dissipation does not change during a tide, or during different energetic conditions. The turbulent dissipation does depend on the relative wave height and position in the surf zone. It increases for larger relative wave heights and for a position towards the inner surf zone. Supporting that the turbulent dissipation is mainly due to wave breaking. In large and very small water depths (h>2m and h<0.5m) the turbulent dissipation rate is largest near the bed, indicating that here, the bed-generated turbulence is important.

The sediment concentration increased slightly with relative wave height. The sediment concentration did not depend on the position in the water column, but was larger for smaller water depths. The turbulent kinetic energy time series had generally more peaks than in the sediment concentration time series. This indicates that a relatively small portion of turbulence events reach the bed and stir the sediment. The

relation found between sediment suspension and turbulent kinetic energy highly varied. This was largely influenced by the large difference in instrument positions. In the first week, when the instruments were located at a more or less constant position close to the bed, the relation between sediment suspension and turbulent kinetic energy was clearly high (up to 90%). This indicates that sediment suspension can definitely be related to surface-generated turbulence. Turbulent kinetic energy sometimes seems to be the dominant mechanism for suspending sediment, while at other times this is not the case.

So turbulent kinetic energy is spreading downward towards the bed, does depend on relative wave height and higher energetic conditions, and is generally larger in the surf zone than seaward of the surf zone. Turbulent kinetic energy can also be related to sediment suspension, but the strength of this relation is highly variable, so it is unclear whether turbulent kinetic energy is the dominant mechanism for suspending sediment, and especially during which conditions this is (not) the case.

Appendix

Several γ methods could be applied in the Battjes-Janssen model.

First of all the method that computes breaker parameter γ according to Battjes & Stive (1985). Battjes & Stive use as input the offshore wave height H_{rms0} and the offshore wave number k_0, as follows:

$s_0 = H_{rms0} /(2\pi/k_0)$ (A1)

$\gamma = 0.5+0.4\tanh(33*s_0)$ (A2)

Secondly, the method that computes the breaker parameter γ according to Ruessink et al. (2003). Ruessink et al. use as input the wave number k, and the total water depth h, which also includes wave set-up and tidal influences, and γ is computed according to the following formula:

$\gamma = 0.76*k*h + 0.29$ (A3)

Finally, the method that computes the breaker parameter γ according to Apotsos et al. (2008). Apotsos et al. use as input the offshore wave height H_{rms0}, and the wave model number, which changes per model (possibilities are the Janssen model, the Battjes-Janssen model and the Baldock model). This function is based on eq.23 and fig.7 in Apotsos et al. (2008).

$\gamma = a+b*\tanh(c*H_{rms0})$ (A4)

For wave model number = 2 (= Battjes-Jansen model), a = 0.30, b = 0.45, c = 0.9, so that:

$\gamma = 0.3+0.45*\tanh(0.9*H_{rms0})$ (A5)

8. References

Aagaard, T. and M.G. Hughes, 2010. Breaker turbulence and sediment suspension in the surf zone. Marine Geology 271, pp 250-259.

Apotsos, A., B. Raubenheimer, S. Elgar and R.T. Guza, 2008. Testing and calibrating parametric wave transformation models on natural beaches. Coastal Engineering 55, pp. 224-235.

Battjes, J.A., J.P.F.M. Janssen, 1979. Energy loss and set-up due to breaking of random waves. Proceedings of the Coastal Engineering Conference 1 (1979), pp. 569-587.

Battjes, J.A. and M.J.F Stive, 1985. Calibration and verification of a dissipation model for random breaking waves. Proceedings of the Coastal Engineering Conference 1 (1984), pp. 649-660.

Beach, R.A. and R.W. Sternberg, 1996. Suspended-sediment transport in the surf zone: response to breaking waves. Continental Shelf Research 16, pp 1989-2003.

Bryan, K.R., K.P. Black and R.M. Gorman, 2003. Spectral estimates of dissipation rate within and near the surf zone. Journal of Physical Oceanography 33, pp. 979-993.

Butt, T., P. Russell, J. Puleo, J. Miles and G. Masselink, 2004. The influence of bore turbulence on sediment transport in the swash and inner surf zones. Continental Shelf Research 24, pp. 757-771.

Elgar, S, B. Raubenheimer and R.T. Guza, 2005. Quality control of acoustic Doppler velocimeter data in the surf zone. Measurement Science and Technology 16, pp 1889-1893.

Feddersen, F., 2010. Quality controlling surfzone Acoustic Doppler Velocimeter bbservations to estimate the turbulent dissipation rate. Journal of Atmospheric and Oceanic Technology 27, pp. 2039-2055.

Feddersen, F. and J.H. Trowbridge, 2005. The effect of wave breaking on surf-zone turbulence and alongshore currents: a modelling study. Journal of Physical Oceanography 35, pp 2187-2203.

Feddersen, F., J.H. Trowbridge, and A.J. Williams, 2007. Vertical structure of dissipation in the nearshore. Journal of Physical Oceanography 37, pp 1764-1777.

Feddersen, F. and A.J. Williams, 2007. Direct estimation of the Reynolds stress vertical structure in the nearshore. Journal of Atmospheric and Oceanic Technology 24, pp 102-116.

George, R., R.E. Flick and R.T. Guza, 1994. Observations of turbulence in the surf zone. Journal of Geophysical research 99, pp 801-810.

Gerbi, G.P., J.H. Trowbridge, E.A. Terray, A.J. Plueddemann and T. Kukulka, 2008. Observations of turbulence in the ocean surface boundary layer: energetic and transport. Journal of Physical Oceanography 39, pp. 1077-1096.

Huang Z.C., S.C. Hsiao, H.H. Hwung, K.A. Chang, 2009. Turbulence and energy dissipations of surf-zone spilling breakers. Coastal Engineering 56, pp 733-756.

Longo S., M. Petti, I.J. Losada, 2002. Turbulence in the swash and surf zones: a review. Coastal Engineering, 45, 129-147.

Lumley, J.L. and E.A. Terray, 1983. Kinematics of turbulence convected by a random wave field. Journal of Physical Oceanography 13, pp. 2000-2007.

Melville W.K., F. Veron, C.J. White, 2002. The velocity field under breaking waves: coherent structures and turbulence. Journal of Fluid mechanics 454, pp 203-233.

Mocke, G.P., 2001. Structure and modelling of surf zone turbulence due to wave breaking. Journal of Geophysical research 106, pp 17.039-17.057.

Mori, N., T. Suzuki and S. Kakuno, 2007. Noise of Acoustic Doppler velocimeter data in bubbly flows. Journal of Engineering Mechanics, pp. 122-125.

Nadaoka, K., M. Hino and Y. Koyano, 1989. Structure of the turbulent flow field under breaking waves in the surf zone. Journal of Fluid Mechanics 204, pp. 359-387.

Ogston, A.S. and R.W. Sternberg, 2002. Effect of wave breaking on sediment eddy diffusitivity, suspended-sediment and longshore sediment flux profiles in the surf zone. Continental Shelf Research 22, pp. 633-655.

Osborne, P.D. and G.A. Rooker, 1999. Sand re-suspension events in a high energy infragravity swash zone. Journal of Coastal Research 15, pp. 74-86.

Puleo, J.A., R.A. Beach, R.A. Holman and J.S. Allen, 2000. Swash zone sediment suspension and transport and the importance of bore-generated turbulence.

Raubenheimer, B., S. Elgar and R.T. Guza, 2004. Observations of swash zone velocities: A note on friction coefficients. Journal of Geophysical Research 109, C01027.

Ruessink, B.G., 2010. Observations of turbulence within a natural surf zone. Journal of Physical Oceanography 40, pp. 2696-2712.

Ruessink, B.G., D.J.R. Walstra and H.N. Southgate, 2003. Calibration and verification of a parametric wave model on barred beaches. Coastal Engineering 48, pp. 139-149.

Scott, C.P., D.T. Cox, T.B. Maddox and J.W. Long, 2005. Large-scale laboratory observations of turbulence on a fixed barred beach. Measurement Science & Technology 16, pp 1903-1912.

Scott, N.V., T.J. Hsu and D. Cox, 2009. Steep wave, turbulence and sediment concentration statistics beneath a breaking wave field and implications for sediment transport. Continental Shelf Research 29, pp 2303-2317.

Sou, I.M., E.A. Cowen and P.L.F Liu, 2010. Evolution of the turbulence structure in the surf and swash zones. Journal of Fluid mechanics 644, pp 193-216.

Suzuki, T., A. Okayasu and T. Shibayama, 2007. A numerical study of intermittent sediment concentration under breaking waves in the surf zone. Coastal Engineering 54, pp. 433-444.

Svendsen, I.A., 1987. Analysis of surf zone turbulence. Journal of Geophysical Research 92, pp. 5115-5124.

Tennekes, H. and J.L. Lumley, 1972. A first course in turbulence, MIT press.

Thomson, J., S. Elgar, B. Raubenheimer, T.H.C. Herbers and R.T. Guza, 2006. Tidal modulation of infragravity waves via nonlinear energy losses in the surfzone. Geophysical Research Letter 33.

Thornton, E.B., 1979. Energetics of breaking waves within the surf zone. Journal of Geophysical Research 84, pp. 4931-4938.

Thorpe, S.A., 2007. An introduction to Ocean Turbulence. Cambridge University Press. Chapters 1 & 2.

Ting, F.C.K., 2006. Large-scale turbulence under a solitary wave. Coastal Engineering 53, pp 441-462.

Ting, F.C.K., 2008. Large-scale turbulence under a solitary wave: Part 2 Forms and evolution of coherent structures. Coastal Engineering 55, pp 522-536.

Ting, F.C.K. and J.T. Kirby, 1994. Observation of undertow and turbulence in a laboratory surf zone. Coastal Engineering 24, pp 51-80.

Ting, F.C.K. and J.T. Kirby, 1996. Dynamics of surf-zone turbulence in a spilling breaker. Coastal Engineering 27, pp 131-160.

Trowbridge, J. and S. Elgar, 2001. Turbulence Measurements in the Surf Zone. Journal of Physical Oceanography 31, pp 2403-2417.

Vittori G., 2003. Sediment suspension due to waves. Journal of Geophysical research 108, pp 4-1 – 4-17.

Voulgaris, G. and M.B. Collins, 2000. Sediment resuspension on beaches: response to breaking waves. Marine Geology 167, pp. 167-187.

Yu, Y., R.W. Sternberg, R.A. Beach, 1993. Kinematics of breaking waves and associated suspended sediment in the nearshore zone. Continental Shelf Research 13, pp. 1219-1242.

Zhang, D. and T. Sunamura, 1990. Conditions for the occurrence of vortices induced by breaking waves. Coastal Engineering in Japan 33, pp 145-155.

Zhang, D.P., T. Sunamura, S. Tanaka and K. Yamamoto, 1994. Laboratory experiment of longshore bars produced by breaker-induced vortex action. Proc. of Coastal Dynamics (1994), pp. 29-43.